Novel All-Aluminium Mirrors of the MAGIC Telescope Project and Low Light Level Silicon Photo-Multiplier Sensors for Future Telescopes

Diploma Thesis of

Cornelia Schultz

Munich University of Applied Sciences

Departement of Precision- and Micro-Engineering,

Engineering Physics/ Technical Physics

Max-Planck-Institute for Physics

Referee: Prof. Dr. Stefan Sotier

Co-referee: Prof. Dr. Ulrich Röder

Supervisor: Dr. Razmik Mirzoyan

October 27, 2008

Abstract

The MAGIC II telescope is, after MAGIC I, the second large diameter Cherenkov telescope build in La Palma. Its goal is to detect extraterrestrial gamma-radiation in the energy region from 30 GeV to 30 TeV. Additionally, MAGIC II has been build with the purpose of stereoscopic observation with MAGIC I. Cosmic particles, such as gamma-rays, protons and heavy particles, generate, when hitting the atmosphere, so-called extended air showers. Ultra-relativistic particles of these showers produce Cherenkov light that can be observed by ground-based telescopes during dark, clear nights. These measurements both provide information about the direction of the primary particle and its energy. From the shower image shape one can distinguish the very rare gamma-rays from the much larger hadronic background. The intensity of the Cherenkov radiation scales in first order with energy. Depending on the shower impact parameter the light flux is typically in the order of ≈ 100 photons/1 m^2 for a 1 TeV shower and an impact value below about 120 m. For impact parameters above 120 m the intensity of the light flux is rapidly dropping as the light originates from the shower halo particles. Therefore, the optical performance as well as the size of the mirror for Cherenkov-telescopes is of great importance, since it is a key element in the detection chain. The optical parameters like the point spread function, the focused reßectivity and the focal length play a major role for recording high quality images. The mirror performance data have to be used for the Monte Carlo Simulation of the MAGIC telescope because it is impossible to test the telescope with calibrated cosmic 'test sources', which do not exist. Note that this is an important difference to particle physics experiments where one normally tests detector elements in test beams. Moreover, it is of great importance to assure the mirror's resistance against the impact of the environmental, such as against dew, rain water

or icing. Therefore, a number of measurements were performed to determine the relevant optical parameters and water tightness for the all-aluminium mirror elements of the MAGIC-II telescope. In this thesis the principles and the results of these measurements will be presented. Additionally, in order to improve the light detection efficiency for future telescope, one considered to use so-called Silicon Photo-Multipliers (SiPM) for Cherenkov light detection. One of the most critical parameters of these novel and still experimental semiconductor light detectors with internal gain is the generation of light in the avalanche gain amplification leading to optical crosstalk and preventing to operate SiPMs with high photon detection efficiency (PDE). As the operation parameters of these devices have also to be used for the Monte Carlo Simulation of future Cherenkov telescopes it is important to evaluate the optical crosstalk rate and its impact on the PDE in great detail. The detailed study of optical crosstalk is also part of this diploma thesis and the analysis and results of this study will be presented here.

Kurzfassung

MAGIC II ist nach MAGIC I das zweite Cherenkov-Teleskop großen Durchmessers, das auf La Palma gebaut wurde, um extraterrestrischer Gamma-Strahlung im Energiebereich von 30 GeV bis 30 TeV zu untersuchen. Darüber hinaus wurde es mit dem Ziel gebaut, zusammen mit MAGIC I stereoskopische Beobachtungen vornehmen zu können. Kosmische Gamma-Strahlen und kosmische Teilchen wie Protonen oder schwere Teilchen, erzeugen beim Eintritt in die Erdatmosphere sogenannte ausgedehnte Luftschauer. Die ultra-relativistschen Teilchen dieser Luftschauer erzeugen wiederum Cherenkov-Licht, das man mit erdgebundenen Teleskopen in dunklen, klaren Nächten beobachten kann. Von dem Cherenkov-Licht kann man sowohl auf die Richtung seines Primärteilchens als auch auf dessen Energie schließen. Außerdem kann man mit Hilfe der Form des detektierten Schauerbildes die seltene Gamma-Strahlung von dem großen hadronischen Hintergrund unterscheiden. Die Intensität der Cherenkov-Strahlung ist in erster Linie proportional zur Energie. Abhängig vom Impact Parameter des Schauers liegt der Lichtfluss eines 1 TeV Schauers mit einem Impact Parameter von 120 Metern typischerweise in der Größenordnung von ungefähr 100 Photonen/1 m^2. Liegt der Impact Parameter über 120 Metern fällt die Intensität des Lichtflusses sehr schnell ab, da das Cherenkov-Licht durch die Teilchen des Schauerhalos erzeugt wird. Deswegen ist sowohl die optische Güte als auch die Größe des Spiegels eines Cherenkov Teleskops von großer Wichtigkeit, da dieser das Schlüsselelement in der Detektionskette darstellt. Die optischen Parameter wie die Punktspreitzfunktion, die fokussierte Reflektivität sowie die Brennweite spielen eine wichtige Rolle bei der Aufnahme von Schauerbildern hoher Qualität. Anders als in der Teilchenphysik, in der man die Dektetorgüte mit Teststrahlen untersuchen kann, kann man die Güte des MAGIC Teleskops

nicht mit einer kalibrierten kosmischen Quelle testen, da solche nicht existieren. Stattdessen wird diese mittels Monte Carlo Simulation untersucht. Hierfür werden die Daten der optischen Spiegelparameter benötigt. Darüber hinaus ist es wichtig, zu gewährleisten, dass der Teleskopspiegel gegen Umwelteinflüsse wie Regenwasser, Eisbildung und Tau resistent ist. Daher wurden mehrere Messungen durchgeführt, um die entsprechenden optischen Parameter der komplett aus Aluminium bestehenden Spiegelelemente des MAGIC Teleskops zu untersuchen und diese auf Wasserdichtigkeit zu prüfen. In dieser Diplomarbeit werden diese Messungen und deren Ergebnisse vorgestellt. Hinsichtlich der Verbesserung der Effizienz der Lichtdetektion wird für zukünftige Cherenkov-Teleskope der Einsatz sogenannter Silizium Photomultiplier (SiPM) zur Detektion von Cherenkov-Licht in Betracht gezogen. Ein sehr kritischter Parameter diese neuartigen Halbleiter Lichtdetektoren, die noch in der Erprobungsphase sind und eine interne Verstärkung besitzen, ist die Lichterzeugung bei der sogenannten Avalanche Gain Amplification, welche optischen Crosstalk zur Folge hat. Dieser verhindert, dass man SiPMs mit hoher Photonendetektionseffizien (PDE) betreiben kann. Da die Betriebsparameter der SiPMs ebenfalls in der Monte Carlo Simulation zukünftiger Cherenkiv-Teleskope verwendet werden würden, ist die Untersuchung der optischen Crosstalkrate und dessen genauer Einfluss auf die PDE sehr wichtig. Daher werden in dieser Diplomarbeit eine ausführliche Analyse und die Ergebnisse bezüglich optischen Crosstalks vorgestellt.

Contents

1 Introduction

Over the last decades, there has been an enormous development in astrophysical sciences, mainly due to the opening up of the electromagnetic spectrum outside the visible range for astronomical observations. The new fields were radio astronomy, Infra-Red astronomy, X-ray astronomy and γ-ray astronomy. Especially the field of high energy astroparticle physics is of great importance for the fundamental physics research of cosmic objects dealing with non-thermal processes. Astroparticle physics deals, among other things, with the observation of energetic photons, also called γ-rays. These γ-rays are energetic electromagnetic particles of at least a few hundred keV. Currently, they can be considered as the most important 'messengers' of high energy processes in stellar environments as they fly at the speed of light along a straight line (a consequence of gammas having no mass and charge). The observation of γ-rays on earth allows back-extrapolation to their origin, as well as to set a lower limit on the energy in cosmic particle processes and their time structure. They are therefore, directly related to high energy particle interaction and particle generation. These are so-called ultra relativistic particle processes in the universe that mainly take place in or nearby stellar environments, which cause particle acceleration. Thus, the so-called Very High Energy (VHE) γ-Astronomy, observing γ-rays with energies of at least 10 GeV up to 100 TeV, allows one to understand stellar processes at extreme conditions.

1.1 Discovery of Cosmic Rays

In 1911 the field of astroparticle physics was 'opened' by Viktor Franz Hess's discovery that charged radiation comes from the outer space. He detected this radiation, which was named 'cosmic rays', during his studies of ionized radiation.

At that time, scientists were wondering about the phenomenon where charged electrometers was discharged over time even though they were isolated from the Earth. Their assumption was that this effect was caused by ionizing radiation. Still, there was the question, where did this radiation come from? One theory was based on the assumption that this ionizing radiation was coming from nearby radioactive substances of the soil or minerals. Hess tested this assumption with some experiments carried out between 1911 and 1913. By measuring the ionizing rate with electrometers at high altitudes during several balloon flights he discovered that the radiation rate first decreased with increasing height, but during a further rise of the balloon, he detected that the discharging rate was got higher and higher, again with increasing altitude. Hess suggested that this rise was a consequence of ionizing radiation coming from outer space and that this radiation is partially shielded by the Earth's atmosphere. This hypothesis was proven to be correct over the following years. In addition, it has been proven that these ionizing particles are the product of the interaction of high energy particles and atoms of the atmosphere.

1.1.1 Composition of Cosmic Rays

Cosmic rays consist mainly of charged nuclei. However, cosmic rays also consist of components, which have no electrical charge. These components are γ-rays and neutrinos, the latter are very difficult to observe as neutrinos are weakly interacting particles. The composition of cosmic rays varies according to the energy. The measured energy spectrum of cosmic rays, see figure 1.1, extends over more than 13 orders of magnitude whereas the flux drops from $\approx$ 1 particle/(cm^2 s) at energies of 100 MeV to less then 0.01 particles/(km^2 century) for the highest observed energy.

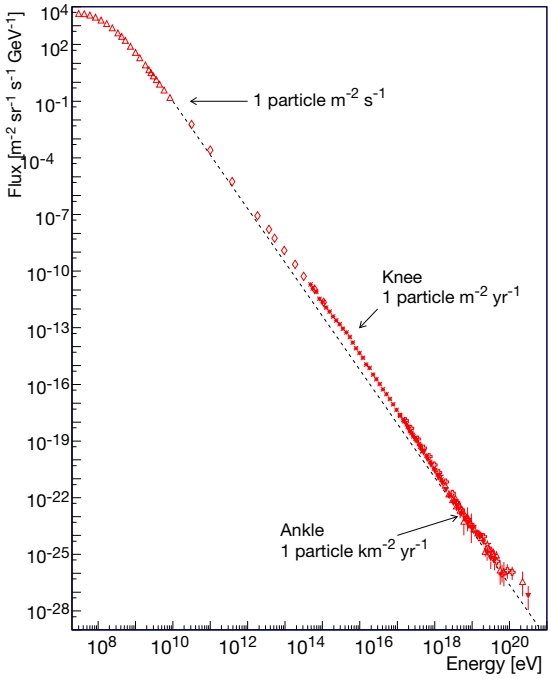

Fig. 1.1: The cosmic ray spectrum[1]: The data compiled are by Simon Swordy.

Above $\approx$ 1 GeV the differential flux $\mathrm{d}N/\mathrm{d}E$ can be approximated by a simple power law.

$$\mathrm{d}N/\mathrm{d}E \propto E^{-2.6\alpha} \tag{1.1}$$

At $\approx$ 1 GeV above the energy spectrum the particles propagating to Earth are no longer affected by the solar wind and the Earth magnetic field. As one can see in figure 1.1, there are two significant structures called the knee and the ankle. Up to about 10^{14} eV the chemical composition of cosmic rays can be measured directly. It is mainly composed of protons (about 79 %). The remainder being mainly helium nuclei (about 70 %) and a small fraction of nuclei of heavier elements, as well as electrons and positrons. Below 10 GeV most cosmic rays come from the sun, whereas cosmic rays of higher energies are assumed to originate from galactic accelerators while above 10^{15} to 10^{17} eV particles from extra-galactic sources gradually start to dominate. Up to $\approx 10^{20}$ eV one cannot trace charged particles back to their origin as they are deflected by the Earth magnetic field and completely scrambled in their direction. By contrast γ-rays are not deflected and, hence, can be traced back to their origin. In the following section, the production

mechanisms and some parameters of γ-rays will be described in greater detail.

1.1.2 Cosmic γ-rays

Cosmic γ-rays are photons of energies above 100 keV as these do not carry magnetic fields. Therefore, its source position can be determined by the photon's direction of arrival. By analyzing cosmic γ-rays, it is possible to carry out astronomical observations covering a large part of the electromagnetic spectrum. The energy band of cosmic γ-rays is commonly subdivided into five sections, as listed in table 1.1.

Low Energy	LE	100 keV - 10 MeV
Medium Energy	ME	10 MeV - 1 GeV
High Energy	HE	1 GeV - 100 GeV
Very High Energy	VHE	100 GeV - 100 TeV
Ultra High Energy	UHE	$>$ 100 TeV

Tab. 1.1: Subdivision of the γ-rays energy band

1.1.3 Sources of Cosmic γ-rays

In this section, the possible sources of cosmic γ-rays will be shortly described. These sources are divided into different classes. High energy photons cannot be accelerated like charged particles. Generally, high energy γ-rays are generated from the interactions of parent particles of even higher energy. These can either be accelerated electrons or hadrons. γ rays can either be generated by high-energy electrons, which 'up-scatter' via inverse Compton (IC) scattering low-energy photons or, are produced by hadronic interaction of accelerated hadrons and nuclei of interstellar or stellar residual gas with other nuclei. In these interactions often π^0-mesons are produced, which decay in a very short time ($\approx 10^{-16}$ sec in the cm system) in two γ-quanta. Besides the inverse Compton scattering and π^0-decay processes two other mechanisms exist for γ-production. These are Bremsstrahlung and Synchrotron Radiation. The Bremsstrahlung mechanism describes the deceleration of a charged particle due to the strong electric field of a charged particle.

This means, that the charged particle loses kinetic energy, which is dissipated into radiation. Synchrotron radiation is emitted when a charged particle passes a strong magnetic field. Because of its low mass only electrons (positrons) lose a significant amount of energy while protons contribute very little to the synchrotron photons in the universe. A specific process linked to electrons can occur in many stellar environments where particles can be accelerated. The so-called synchrotron self-Compton scattering (SSC) describes the process where at first electrons produce synchrotron photons when passing a magnetic field and than the same electrons can up-scatter these photons by IC scattering up to almost the energy of the parent electrons. Figure 1.2 shows a sky map of the high energy γ-rays[2] sources discovered up to now (2008).

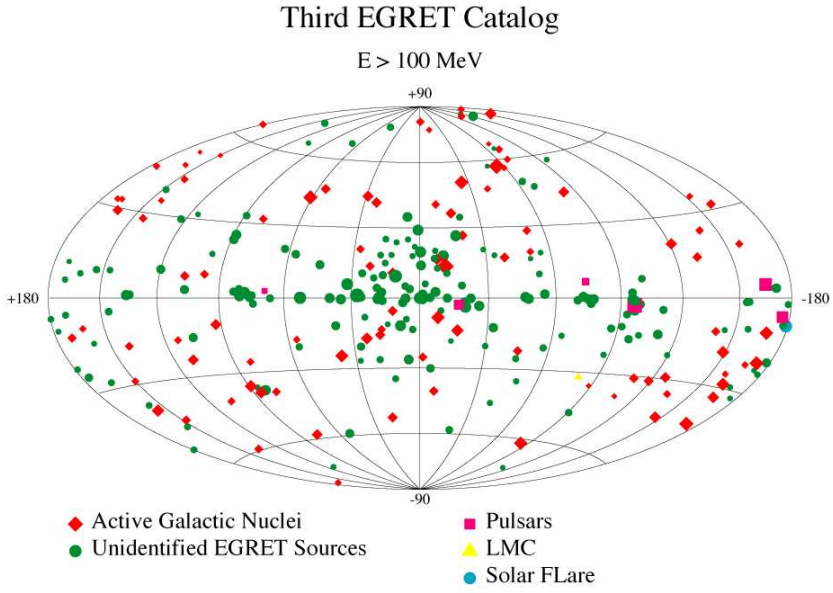

Fig. 1.2: Known sources of γ radiation[3]

The different classes of cosmic γ-ray sources[1] are:

- Active Galactic Nuclei
- Microquasars
- Supernova Remnants
- Pulsars ans Pulsars Nebulae
- γ Ray Bursts

1.1.4 Detection of Cosmic γ-rays

The field of γ-astronomy offers the possibility to analyze astronomical objects, which produce these high energy particles. By observing the emission of γ-rays four parameters characterizing the γ radiation can be measured directly. Thus, conclusions about the mechanism of the γ-rays production and the density of the intergalactic infrared photon field can be made. The four parameters are:

1. The flux coming from the source. This is defined as the number of γ-quanta, which arrive at the Earth's atmosphere per unit time and per unit area.
2. The energy spectrum.
3. The time dependency of the flux and the spectrum.
4. The arrival direction allows one to decide whether one is observing a point-like or an extended source.

In order to detect cosmic γ-rays of very high energies, either satellite-borne or ground-based detectors are used. These instruments should have detection areas that match the flux of gammas in the energy range to be studied. This restricts the detection range of satellites to 10^{12} eV. For satellites with a sufficiently large detection surface energies above $\approx$ 1 TeV would be both too heavy and too expensive. That is why ground-based detectors, so-called air Cherenkov telescopes are used for the observations of high energy γ-rays. As γ-rays interact with the top layer of the Earth's atmosphere and thus initiate an electromagnetic shower, one has to observe γ-rays indirectly by studying signals from the avalanche of

[1] A brief description of the sources is given in section A.

the secondary particles caused by this interaction. When the charged secondary particles of the avalanche move in the atmosphere at a velocity exceeding that of the speed of light, they produce so-called Cherenkov light, see section 1.2. This light is emitted mostly in the direction of the shower particles (with only a small angular deviation depending on the refractive index of the atmosphere as a function of altitude) and can be measured with the above mentioned Cherenkov telescopes. The basic principle is very similar to compact and heavy calorimeters used in high energy physics experiments at accelerators. The main difference is that one uses the Cherenkov light as a measure of the shower energy and the density is variable and at least a factor 1000 lower than the accelerator calorimeters. Furthermore, the atmospheric calorimeter has no confining and sealed walls and changes constantly the density (due to the earth rotation) and its transmission due to weather changes.

1.2 Cherenkov Radiation

In 1934 the Russian physicist Pawel Alexejewitsch Cherenkov discovered the emission of bluish light from relativistic radioactive particles in water for which he received the Nobel Prize in 1958. Cherenkov radiation is an electromagnetic radiation due to the interaction of fast moving charged particles with other particles. Its generation can be explained as follows. In general, if a particle passes a transparent medium, the atoms along its trajectory get temporarily polarized and emit electromagnetic waves due to polarization. Usually, these waves interfere destructively. Therefore, no light emission is observable. However, if the particle moves at a velocity that is faster than the speed of light, in this medium the waves of neighboring atoms no longer interfere in a destructive manner, as they develop faster than they extinguish each other. These electromagnetic waves are then observable as Cherenkov-light that has the shape of a Mach cone as shown in figure 1.3. In analogy to the phenomenon seen in the case of macroscopic objects moving at supersonic velocity in gases one parameter of the Mach cone is its angle of aperture ϕ, which depends on the velocity ν of the particle and the speed of light c' of the medium which has the refraction index n. The so-called beta factor

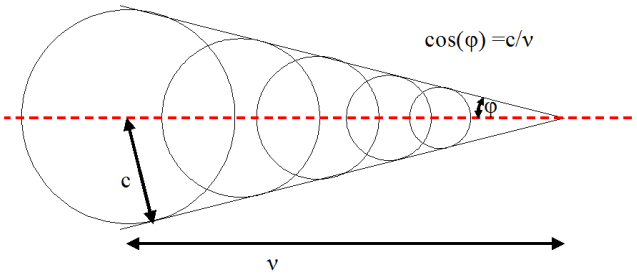

Fig. 1.3: Propagation of electromagnetic waves with the shape of a Mach cone

specifies the ratio of ν and c

$$\beta = \frac{\nu}{c} \tag{1.2}$$

Furthermore, in a medium the speed of light is computable by dividing the vacuum speed of light c by the refraction index n of the medium.

$$c' = \frac{c}{n} \tag{1.3}$$

The angle of aperture ϕ can be determined as follows:

$$\cos(\phi) = \frac{c'}{\nu} = \frac{1}{n\beta} \ . \tag{1.4}$$

It is within the range of $(0.4 - 1.2)^\circ$ for Cherenkov light. In the following section a simplified model for the shower process as found, for example, in many text books will be briefly described.

1.2.1 Simplified Model of the Air Shower Process

When a high energy cosmic γ-ray hits the upper layer of the atmosphere, it generates mostly within the first radiation length an electron positron pair with a partition of energy summing up to the initial energy. For simplicity one can assume that each carries about half the initial energy. Again, within about a radiation length both the electron and positron lose a large fraction of their energy by Bremsstrahlung, i.e. both produce a γ-ray that carries about a quarter of the initial energy. Within the next radiation length the multiplication processes are

repeated and at the same time the energy per particle drops by a mean value of 1/2. Parallel to the multiplication process the charged electrons/positrons lose a tiny fraction of their energy by ionization. The multiplication process continues until the electrons have such a low energy that the charged particles lose about the same amount of energy by ionization and producing gammas by Bremsstrahlung. Eventually the energy will be so low that pair productions no longer occur and energy losses of the charged electrons/positrons by ionization dominate and eventually stop all charged particles. The showering process eventually dies out. The process is very similar to an avalanche and is therefore, often called an avalanche multiplication process. The maximum of this electromagnetic shower, i.e., when the number of charged particles is reached, is when the probability of both possibilities for energy loss are the same. Figure 1.4 illustrates the development, as well as the composition of such an electromagnetic shower inducted by γ-rays. As described, the number of charged particles is reached when the probability

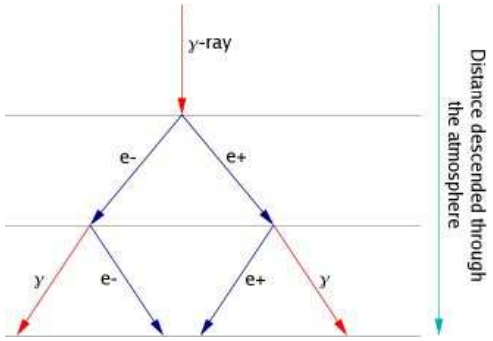

Fig. 1.4: Development of an electromagnetic particle shower[4]

of both possibilities for energy loss is the same. As described above, a g-ray induced shower contains practically only electrons and positrons as charged particle (according to the literature there exists a small probability for so-called photoproduction of heavier particles, but this process can be completely neglected) as the small mass of electrons/positrons are above a few MeV highly relativistic energy. During their transition through the atmosphere these ultrarelativistic electrons/positrons can generate Cherenkov radiation if their β factor is above $\beta_{\text{Cherenkov}}$. The Cherenkov spectrum observed on the ground is within a wavelength range from 300 nm (limited by the absorption of Ozone) up to several meters of wavelengths, again limited by the atmospheric transmission in the IR set by water and CO_2. Since the spectral intensity distribution is proportional

to λ^{-2}, the Cherenkov light is rather ultraviolet and blue. Part of the Cherenkov light is lost during the passage of the atmosphere. This is due to Rayleigh and Mie scattering. The radiation at short wavelengths is more decreased by Rayleigh scattering than at longer wavelengths due to the λ^{-4} proportionality of Rayleigh scattering. Figure 1.5 shows spectra of Cherenkov emission for different energies.

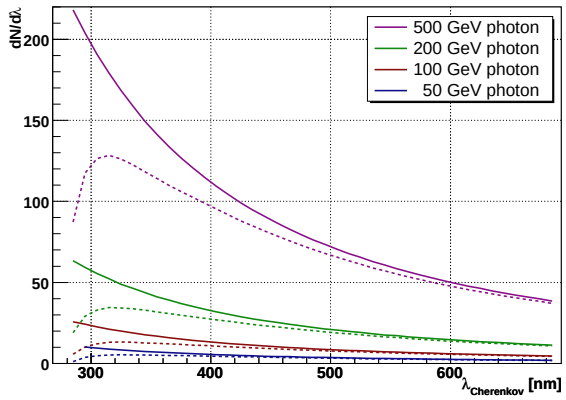

Fig. 1.5: Typical calculated spectra of Cherenkov radiation for different energies before (continuous line) and after interaction with atmospheric particles (dashed line)[5]. Cherenkov radiation of an atmospheric shower is maximal at about 340 nm for a zenith azimuth of 30°[2].

1.2.2 Gamma-Hadron Separation

In the following section, some of the fundamentals of air shower physics as well as the methods used to separate gammas from hadrons that have taken many years to be developed by the γ-astronomy community will be summarized. More details can be found in the relevant literature. As mentioned in section 1.1.1, the VHE cosmic rays not only consist of γ-quanta but also of charged particles such as hadrons. These hadrons also generate air showers and hence Cherenkov light. However, since hadrons are charged particles, they get distracted by the extragalactic as well as the Earth's magnetic field. Consequently, they can not be back-extrapolated to the source's position. Moreover, the hadronic portion of

[2]The position of the maximum varies according to the zenith azimuth. With increasing zenith azimuth. The maximum is shifted to longer wavelength[6].

cosmic rays is up to 10^5 times larger compared to the small fraction of γ-rays emitted by point sources. Thus, hadronic showers represent an immense background for the ground-based γ-rays astronomy. In satellite borne detectors one can easily sup press the hadronic background by using an anticoincidence counter above the γ-detector. This is impossible for ground-based γ-ray detectors and other methods have to be used to filter out the rare γ-rays. This is done with the so-called γ-hadron separation via analysis of the shower images that are recorded by the telescope. The schematic development of a hadronic shower emitting partially Cherenkov light is illustrated in figure 1.6. In hadronic interactions one produces mostly pions as secondary particles. For the following topic one can neglect the small number of other secondary particles (P, antiprotons, strange participles...). On average 2/3 of the secondary pions are charged and 1/3 π^0s. The charged pions can either decay, fuelling the muon component of the shower or interact with atmospheric nuclei and fuel the hadronic component (again with $\approx 1/3$ π^0s) while the π^0s decay into two γs. The γs from the π^0s -> $\gamma\gamma$ decay now start the production of electromagnetic sub showers thus fuelling the electromagnetic component of the originally hadronic shower. As in any hadronic interaction, about 1/3 of the energy is transferred to π^0s. Eventually most of the shower energy will be transferred to the electromagnetic component. For example, in the second half of the showering process most hadronic shower consist of nearly only electrons, positrons and γs and a few energetic muons and (invisible) neutrinos and rarely some protons and charged pions. The huge number of electrons and positrons are mostly above the Cherenkov threshold in the atmosphere and therefore, produce a light flash similar to a γ-induced shower, i.e. one cannot only discriminate the amount of Cherenkov light γs and hadrons as one has no independent measurement of the initial energy. (To give a typical number: a hadron shower of 1 TeV produces on average about the same amount of light as a 1/2 TeV γ-shower). Nevertheless, there are small differences in the 'Cherenkov shower image' depending on the initial γs and hadrons. In γ-induced showers the secondary electrons, positrons and γs are very closely collimated along the shower axis. This is due to the very small transverse momentum of the secondary partic les. The main effects, that transversely blow up a shower are multiple scattering and small deflections of electrons/positrons by earth magnetic field. As a consequence, the γ-shower images are rather narrow and regular. In hadronic interactions the sec-

ondary particles receive a transverse momentum 'kick', which deflects them away from the shower axis. As a consequence, the showers become wider. In addition, the hadronic interaction length in the atmosphere is ≈ 2.5 times longer than the radiation length, i.e. hadrons fly on average 2.5 times further before undergoing an interaction. Also, the number of secondary particles in a hadronic interaction can vary by a large factor while in electromagnetic interactions normally only one additional 'particle' is produced. Therefore, in summary, hadronic showers are much more irregular, wider and normally more extended in length than an electromagnetic shower. These differences show up in the images recorded by a Cherenkov telescope and can be used to discriminate the primary particles. Obviously, the method has limitations as the statistical nature of the shower process leads to many fluctuations that at times will result in γ-showers looking like a typical hadron shower and also other hadron showers will look like γ-showers. Figure 1.7 shows a simulation of a γ and a hadron induced air shower. The typ-

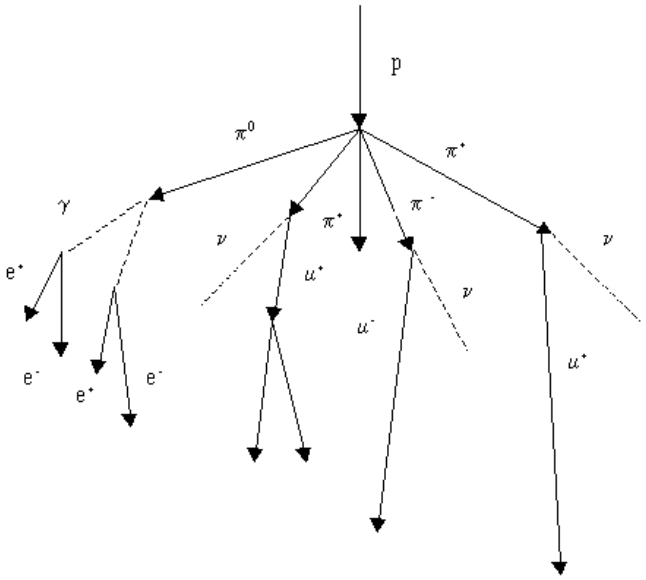

Fig. 1.6: Development of a hadronic air shower[4]

ical differences in the shower images can be used to develop separation criteria for the enrichment of γs in the recorded data samples, see section 1.2.3.

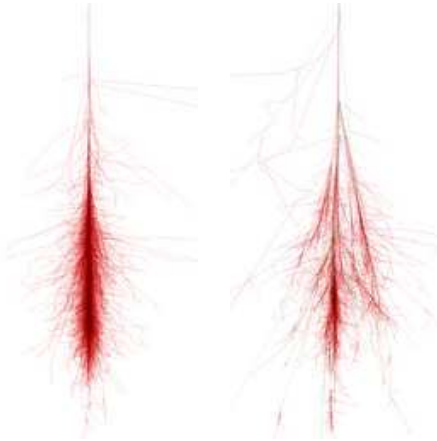

(a) Electromagnetic shower (b) Hadronic shower

Fig. 1.7: CORSIKA Simulation of a hadronic and an electromagnetic air shower at E= 100 GeV[7]: The hadronic shower is wider than the electromagnetic one.

1.2.3 Detection and Analysis of the Cherenkov Light

For the data acquisition the so-called imaging technique which is presented in figure 1.8 is used. For the observation the telescope's axis is pointed towards the

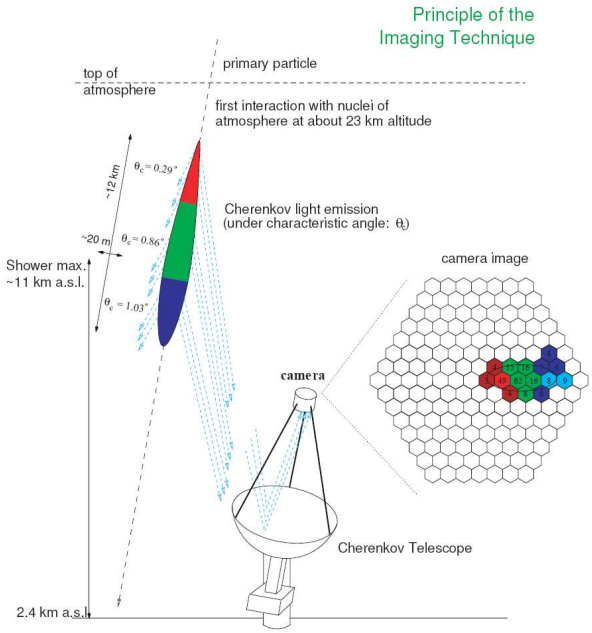

Fig. 1.8: Principle of the imaging technique[4]

object to be studied. Air showers, caused by γ-radiation emitted by the object, are seen as a two-dimensional image on the camera plane and can be recorded using suitable light detectors. In the case of a point source of γ-rays the main axis of the air shower images are aligned towards the centre of the camera. If the air shower impacts within a radius of about 120 m around the telescope, the efficiency of the Cherenkov telescope is optimal because light from particles along or close to the shower axis falls onto the telescope mirror and can be recorded by the so-called camera mounted on the focal plane of the telescope mirror. The camera is composed of a matrix of small photomultipliers, which allow one to record the very fast signals of the Cherenkov light flash, (typically of $2 - 10$ ns duration). The images of the air shower are then parameterized by the so-called HILLAS-Parameters, which are named Dist, Size, Length, Width, Concentration and Alpha. These are shown in figure 1.9. With these parameters

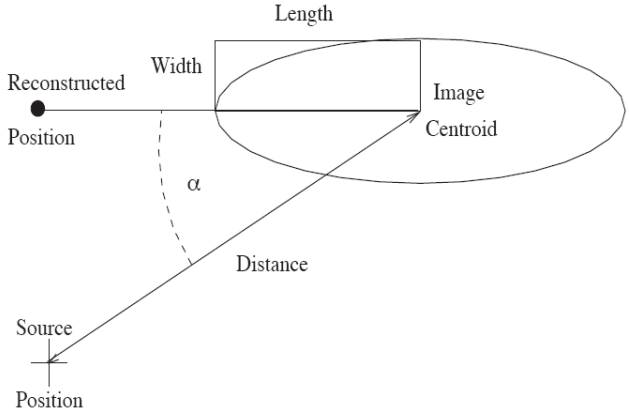

Fig. 1.9: Sketch of the HILLAS Parameter[8]

it is possible to draw conclusions on the initial particle and the energy of any given event. Furthermore, the origin of the γ-quanta that generated the detected air shower can be determined by extrapolation. Thus, the position of a source of γ-radiation can be located on the sky map. In order to reduce the background of the signal, so-called 'ON' and 'OFF' data are recorded by pointing the telescope onto the source and then a few degrees away from the source. The first step in the analysis is the so-called 'image cleaning' to reject accidental triggers and to prepare shower images for analysis. (Further details are not given on this, as

this, as this is a rather detailed procedure and not the subject of this thesis). The HILLAS parameters differ depending on the type of primary particles. The reason for this is the different development of the showers, as explained in the previous chapter. This enables the distinction between air showers generated by hadrons and those induced by γ-quanta. Unlike showers induced by γ-quanta, hadronic showers do not point to the camera centre. Moreover, as described in the previous section, hadronic shower images have a more expanded image than that of γ-showers. Sometimes muons are generated in hadronic showers, because of charged pion decay. Energetic muons also emit Cherenkov light. If the impact parameter is below 30 m, one sees a ring, respectively a large arc (ring section). Figure 1.10 shows an example of these three different types of shower images.

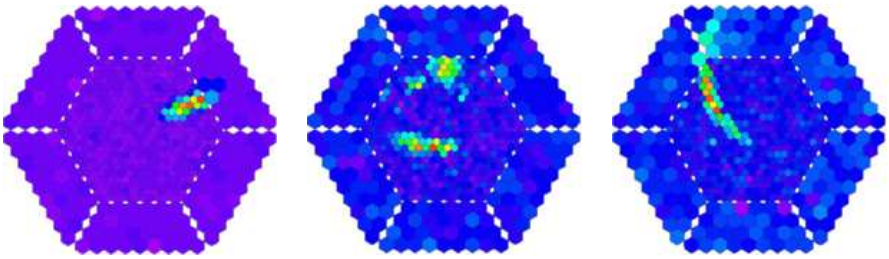

(a) γ-ray candidate (b) Hadron candidate (c) Muon Ring

Fig. 1.10: Different shower Images recorded by the MAGIC camera[9]

1.3 Monte Carlo Simulations

Usually, in order to investigate the performance of a detector, one uses either a test beam of known parameters or, if not available, one studies its response to a known signal, functioning as a test signal. Unfortunately, a cosmic γ-ray beam of defined sharp energy and timing does not exist, therefore the Monte Carlo simulations method has to be used as the key method to study IACT performances. This method simulates showers from a predefined direction and energy calculating the transport of Cherenkov light through the atmosphere and telescope and then analyses the images. It is nevertheless, important to know all the performance data of the entire detection chain. In doing so, important parameters such as detection efficiency or the energy threshold of a telescope can be evaluated.

Therefore, the Monte Carlo (MC) simulation is also used to estimate the performance of the MAGIC telescope[6]. As mentioned above, this simulation is divided into three sections. The first section generates a shower of secondary particles in the atmospheric calorimeter, simulated by the emitted Cherenkov light and calculated by the transport of these photons through the atmosphere down to the ground and onto the telescope. The simulation is based on the CORSIKA code (Cosmic Ray Simulations for Kascade[10]) developed at Karlsruhe. In this program the attenuation of the air shower light due to absorption and scattering in the atmosphere is simulated. Afterwards, the reflection of the light shower is evaluated taking the optical parameters of the mirror elements into account. Finally, the response of the telescope camera is simulated[2]. In order to improve the second stage of the MC simulation the here defined 'focused reflectivity', as well as the results obtained will be the central part of this thesis. Additionally, since the possibility of using a silicon photo-multiplier (SiPM) as camera pixels instead of the usual photo-multiplier tubes(PMTs) in future telescopes is being considered, an analysis of the crosstalk due to the avalanche amplification in SiPM will be presented. Thus, the third stage of the MC simulation can be adapted properly.

1.4 The Goals and Structure of this Thesis

The main goals of this thesis are:

1. The study of the overall reflectivity, optical focusing and the so-called focused reflectivity of the mirror panels for the MAGIC II telescope

2. A specific study, the optical crosstalk rate as a function of operation voltage, for the SiPMs, a novel high detection efficiency photon detector under consideration for future IACTs

The focused reflectivity specifies the amount of reflected light from a point source falling on a pixel of the camera. This measurement is important as the mirror panels have quite some halo due to the specific production process. On the one hand a strong halo increases the energy threshold whereas on the other, one can fake a large shower width that spoils the decisive γ-hadron separation. A new method for the determination of the focussed reflectivity has been developed in

this thesis. The SiPM is a novel solid state photon detector with the potential of a high photon detection efficiency of perhaps a $2-3$ times higher photon detection efficiency compared to the currently used photomultipliers. Besides some of the very promising performance data SiPMs still have some problems. One of the most severe ones is the optical cross-talk that prevents operating them at a high voltage above the avalanche breakdown necessary to achieve a high photon detection efficiency. Here some of the first studies of the correlation of the optical crosstalk of the Hamamatsu MPPCs, currently considered as one candidate for future IACT cameras, will be reported about. This thesis has the following structure: Chapter 1 will cover the objectives of cosmic ray physics studies giving emphasis to ground-based high energy γ-ray astronomy. There will also be an evaluation on air showers and their detection in Cherenkov light by using so-called atmospheric imaging Cherenkov telescopes. Obviously, the chapter is based on many of the publications and studies of the community of high energy astroparticle physicists. The chapter is therefore, the essential background for the experimental studies described in the next chapters.
In chapter 4 the measurements of the optical cross-talk in a specific SiPM will be presented.
In chapter 5 a short conclusion will be given.
The Appendix contains a list of abbreviations, figures and tables and additions, as well as some details of the measurements, which are only of interest for those doing similar studies.

2 The MAGIC Telescope

In this chapter the basic construction of the MAGIC telescope[11] will be described. Furthermore, the differences between MAGIC II and I will briefly be pointed out. One of the major differences is represented by the mirror elements of the MAGIC II telescope. They differ both in their production method, as well as in their requirements, which will both be explained in detail. This is the main part of this thesis.

2.1 The MAGIC Telescope Basic Design and Functioning

The basic design of the 17m diameter 'Major Atmospheric Imaging Cherenkov' (MAGIC) telescope is shown in figure 2.1.

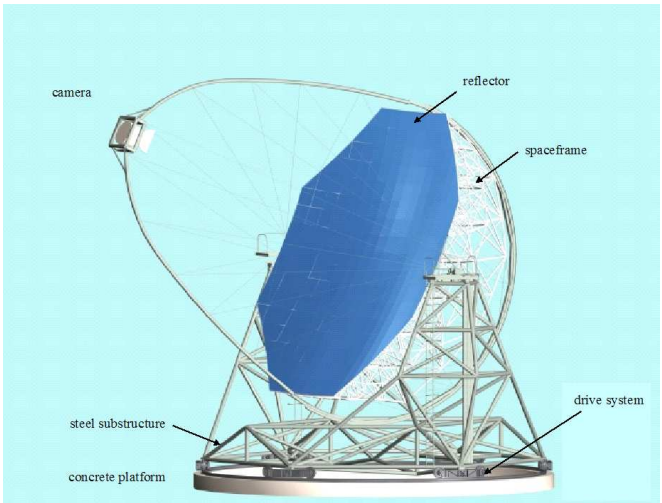

Fig. 2.1: Basic design of the MAGIC telescope[6].

The main components are:

- A concrete platform with a circular rail with a 19 m diameter
- A tubular steel substructure with 6 undercarriages rotating around a central axis
- A lightweight spaceframe carrying the main mirror
- A tessellated reflector composed of several small mirror elements
- An active mirror control to correct small deformations of the spaceframe during operation (not shown)
- A 590 pixel photomultiplier camera supported by a parabolic shaped mast structure. The camera covers a field of view (FOV) of $\approx 3.2^\circ$
- The telescope drive system for the azimuth and altitude movements
- The signal transmission system and readout electronics (not shown).
- Auxiliary components (not shown), necessary for the operation of the telescope

The telescope frame, which is a light weight construction is mounted on bogeys. In this way, the MAGIC telescope can quickly be turned horizontally and vertically. Thus, the telescope can be orientated to any celestial position. The MAGIC telescope has a so-called alt-azimuth mount with an octagonal, tessellated, parabolic reflector with a large surface. The mirror surface is composed of several small spherical mirror elements of slightly different radii in order to approximate the overall parabolic profile. Each mirror element[1] of 1 x 1 m^2 area is separately mounted onto the telescope's space frame by a 3-point mount and can be remotely, respectively and automatically adjusted. This is the so-called 'Active Mirror Control'[12](AMC). For a short description see section B. The reason for the AMC is - similar to the use in large modern optical telescopes with segmented mirrors - and is to correct the small deformations of the lightweight mirror support structure (only 5 tons for the 17 m diameter frame). These deformations are unavoidable when tracking a source or repositioning the telescope. The AMC

[1]In Magic I four small mirror elements were mounted on a 1 m^2 support panel, which was fixed on the space frame. The reasons behind this solution were technology limitations in the year 2000 for the production of diamond turned mirrors as well as optical considerations.

will always allow one to have the best possible focusing of the 17 m mirror. The intensity of the Cherenkov light flashes is very low. Here some numbers are given to highlight the problem: A vertical incidence γ-shower of 1 TeV and within an impact distance of 120 m generates about $4.5 \cdot 10^6$ photons spread rather uniformly over an area of 45 000 m^2, i.e. about 100 photons per 1 m^2 between 300 nm and 600 nm wavelength. In first order this intensity is proportional to the γ-energy. It should be noted that for an observation this flux of 100 photons/m^2 must be multiplied by the mirror area in m^2 and then by the system quantum efficiency (The efficiency to convert a photon impinging onto the telescope to a measurable electrical signal)of typically $11 - 15$ % (MAGIC I close to 15 %) when averaged over the spectral sensitivity of the PMTs. On the other hand, the background light from the night sky (LONS) from a section outside the galactic plane and during a moonless night is $2 \cdot 10^{12}$ photons/(m^2 sec sterad) in the same wavelength band. When observing objects in the galactic plane or during partial moon shine, the LONS can be considerably higher. The reason why it is possible at all to observe the Cherenkov light flashes against the LONS is that the Cherenkov light flashes are extremely short in time, typically $2 - 5$ ns. The logical conclusions considering the low flash intensity, the high LONS and the short flash time are:

- If one wants to detect low energy γ-showers, one needs very large mirror areas with low light loss (high reflectivity, high focusing).
- In order to minimize the background from the steady flux LONS one must have a readout system that has nsec time acquisition and- very important- a mirror system that does not add extra time spread, i.e. a parabolic mirror profile.

The camera consists of a matrix of 572 PMTs. The arrangement of a hexagonal geometry comprises 396 inner pixels of 0.1° (25 mm diameter PMTs) and 176 outer pixels of 0.2° size (42 mm diameter PMTs). The round PMTs have even in the most dense package some dead areas. To avoid light loss from this dead area each PMT has a small light catcher in front of it to focus the light falling onto the gaps on the PMTs. The function of the PMTs is to convert the light flashes collected by the reflector into photoelectrons and amplify them by a factor $3 \cdot 10^4$. This amplified electrical signal is backconverted into an optical light signal

by vertical cavity laser diodes (VCSEL) and transmitted via optical fibers to the counting house distant 80 metres. (The reason for this procedure is that the initially planned use of coax cables would have been more expensive, very clumsy because of the need of large diameter coax cables, very heavy and would have resulted in quite sa lot of signal distortion and a widening of the $2-5$ ns signals). At the counting house the optical signals are backconverted into electrical signals and then digitized and read out (with a lot of other information) onto storage tapes for later analysis. The analysis of the acquired data is carried out as described in section 1.2.3.

2.2 The MAGIC II Telescope

Both the MAGIC I telescope that has already been running for 4 years and the MAGIC II telescope, currently under construction, are used for ground-based and very high energy gamma astronomy. These are currently the world's largest Imaging Air Cherenkov Telescopes (IACT). Both telescopes are located on the Canary island La Palma at the Observatorio del Roque de Los Muchachos (27.8° N, 17.8° W, 2225 m asl). Figure 2.2 shows both telescopes, one standing next to the other at a distance of 85 m. The motivation for building MAGIC II was

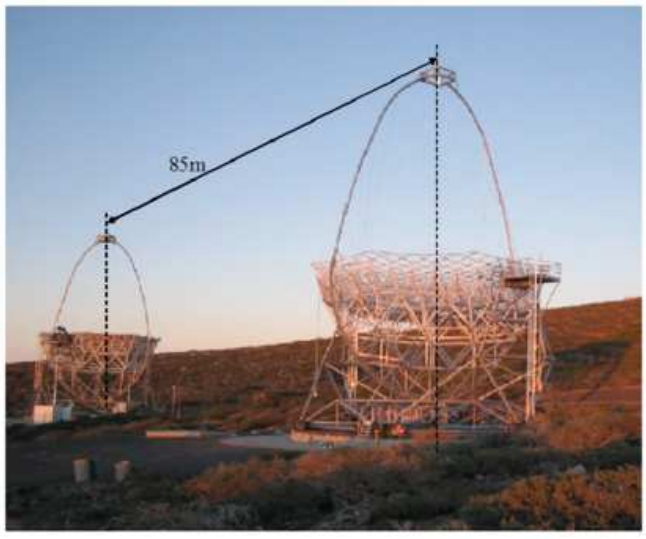

Fig. 2.2: MAGIC I and MAGIC II telescopes in La Palma[2]

two-fold:

1. To increase the sensitivity in the stereo observation mode and to simultaneously allow the observation of two sources. The 'stereoscopic' observation enables a better reconstruction of two important three-dimensional shower parameters[13]. These are the shower impact parameter and the height of the shower maximum. This results in an improved angular resolution, as well as in a better energy resolution, a lower energy threshold and an overall increased sensitivity due to an improved γ-hadron separation.

2. The construction of MAGIC II differs only in part from that of MAGIC I. The general structure, as well as the drive system, have been retained for the second MAGIC telescope. The main differences, motivated by lower installation costs and improved performance are[14]:

   - New types of mirror panels
   - A camera with higher QE PMTs and a 0.1° pixel size throughout the 3.5° field of view
   - A novel digitizer with 2 GHz sampling frequency
   - A sligtly modified drive system

Unlike in MAGIC I, the size of the mirror elements has been changed for MAGIC II from about 0.5 x 0.5 m^2 to nearly 1.0 x 1.0 m^2. Consequently, the number of mirror elements was reduced from 974 to 248. The reason was to very much simplify the installation procedure, accepting a slight optical degradation due to the larger mirror element size. Moreover, the support panels could be omitted and height considerably reduced. The increase in size required an increase of the honeycomb thickness, see section 2.5.1, in order to provide sufficient stiffness of the mirror elements. Besides the all-aluminium sandwich construction with the diamond turned surface also a novel panel type is used for half of the mirror area. The number of camera pixels has been increased from 577 pixels to 1039. Moreover, a new type of photomultiplier with an increased quantum efficiency has been selected. These hemispherical, 6 dynode PMTs from Hamamatsu have a so-called Superbialkali photocathode with a peak quantum efficiency of $32-35$ %. Furthermore, the trigger area has been enlarged from 0.95 to 1.25.

2.3 The MAGIC II Telescope Reflector

MAGIC II has an identically shaped parabolic 17 m diameter reflector whose effective mirror area is of about 240 m^2. Its focal to diameter ratio k, called f-number, is 1. As already indicated, the reflector is composed of many small mirror elements. Since one of the topics of this thesis is the design and study of the mirror elements, the reflector will be described in greater detail. The telescope's reflector, consists of 247 spherical mirror elements of different radii and approximates the overall parabolic mirror shape so that the nearly parallel Cherenkov light intersects the focus avoiding any additional time spread. This is shown in figure 2.3. Furthermore, the parabolic profile provides a high angular resolution

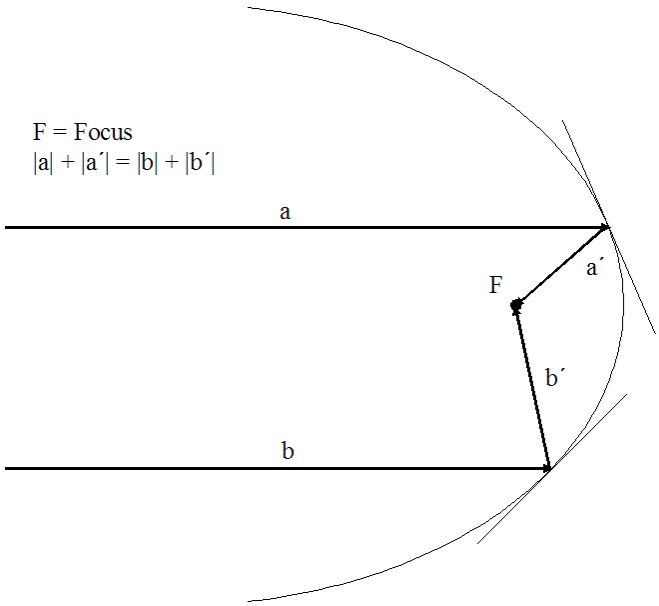

Fig. 2.3: Optical path of the reflected light at a parabolic reflector

in the part of the focal plane close to the axis. As one can see, for example, in figure 2.4 the characteristic of the parabolic reflector is that at each point of the surface it possesses two different curvature radii. These radii are called radial and perpendicular. The radii differ depending on the distance of the reflector's optical axis. The reflector is composed of 247 squared mirror elements, which are either aluminium or glass mirrors. In figure 2.5 one can see the arrangement of the different types of mirrors. The outer 104 mirrors, which are light-blue, are

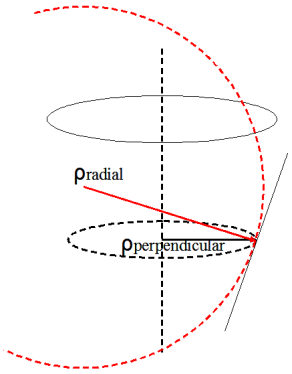

Fig. 2.4: Perpendicular (black) and radial radius (red) of the parabolic reflector curvature

glass surface mirrors. The 143 dark-blue coloured ones are all-aluminium mirrors. For these mirror elements two different production techniques have been used.

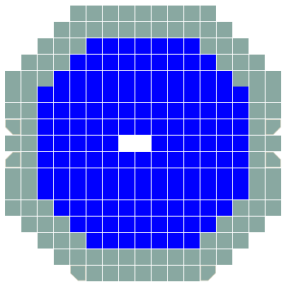

Fig. 2.5: Arrangement of the different mirror types on the reflector frame: The dark-blue colored ones are all-aluminium mirrors whereas, the others are glass mirrors[14].

The production technique of the all-aluminum mirrors will be presented in section 2.5[2]. These two types of mirrors have both advantages and disadvantages. The production of the glass mirrors is much faster than that of the all-aluminium mirrors as the process of diamond turning is unnecessary. Also, the fact that the glass mirrors are lighter than the aluminium ones favors glass mirrors. On the other hand, the glass mirrors require a high quality aluminium coating and an absolutely watertight protection layer. In general, these mirrors age faster than the all-aluminium mirrors as water can creep between the glass and aluminium layer whenever the surface is damaged by dust, cleaning or acid rain. While the

[2]The glass mirror production is appended in section D.

aluminium prototype mirrors for MAGIC have shown very little degradation after 5 years and same can be said for the HEGRA CT1 telescope after 5 years storage, aluminized glass mirrors show quite some degradation after about $5-6$ years. It is hoped that a very careful surface preparation of the novel type of glass mirrors for MAGIC II will very much reduce the aging process. The two different mirror panel types differ with regards to their optical performance. For instance, the reflectivity for pure aluminium used for the glass mirror is higher than for the $AlMgSi_1$ alloy of the aluminium mirror by a few percent. The spectral reflectivity of the two types, as well as of other aluminium alloys, is shown in figure 2.6. As one can also see, the reflectivity of evaporated aluminium is within

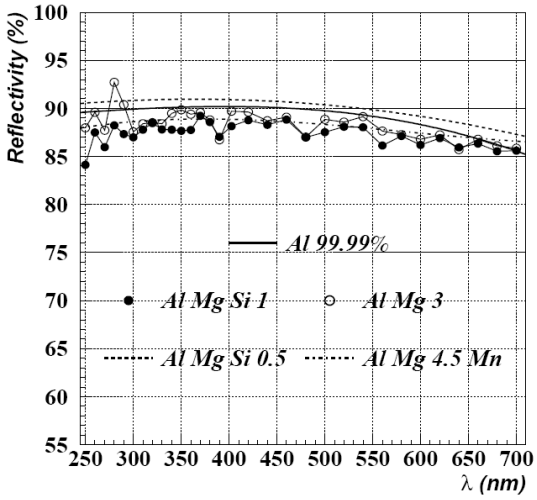

Fig. 2.6: Comparison of the spectral Reflectivity of pure aluminium and different aluminium alloys[15]

the wavelength range of 100 nm to 300 nm higher, which is unimportant for the Cherenkov radiation because the atmospheric Ozone cuts all UV light below $\approx$ 300 nm. On the other hand, the focusing power of the aluminium mirror is much better than that of glass mirrors, which can be seen thanks to the different PSFs[3].

[3]A brief comparison of the differences concerning the measured optical performance will be made in the appended section F.

2.4 Specifications of Mirror Elements of the MAGIC Telescope

There are several requirements the mirrors must have in order to assure a good optical performance of the MAGIC telescope. Some of these concern the geometry and physical parameters, others the optical parameters. Some of these requirements, explained in this section, have been verified by quality checks, see chapter 3. Due to the production methods of these mirrors, see section 2.5, the mirror elements have a spherical shape with a constant radius of curvature. Also, this means that their curvature radii are identical for both directions, as shown in figure 2.7. As explained in section 2.3, the mirror elements approximate the

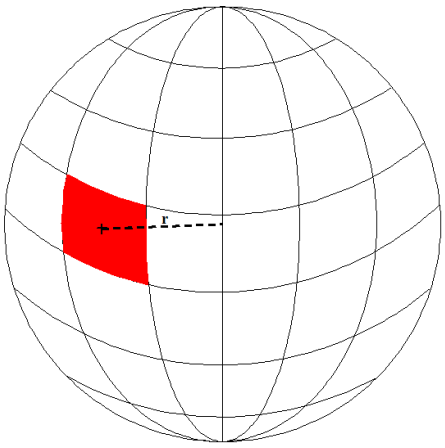

Fig. 2.7: Radius of curvature r of a spherical mirror element

parabolic reflector of the MAGIC telescope. This parabolic profile has however no constant radius of curvature. In consequence, the mirror elements have to differ in their radii of curvature in order to obtain a parabolic shape. Therefore, one must estimate the number of mirror elements that have to be made with a specific radius of curvature. In figure 2.8, the calculation for the number of aluminium mirror panels, having a specific radius of curvature, is presented. The binning reflects the accuracy of the all-aluminium mirror production (15 cm). This calculation is based on the average of the tangential and the radial radius of curvature as illustrated in figure 2.9.

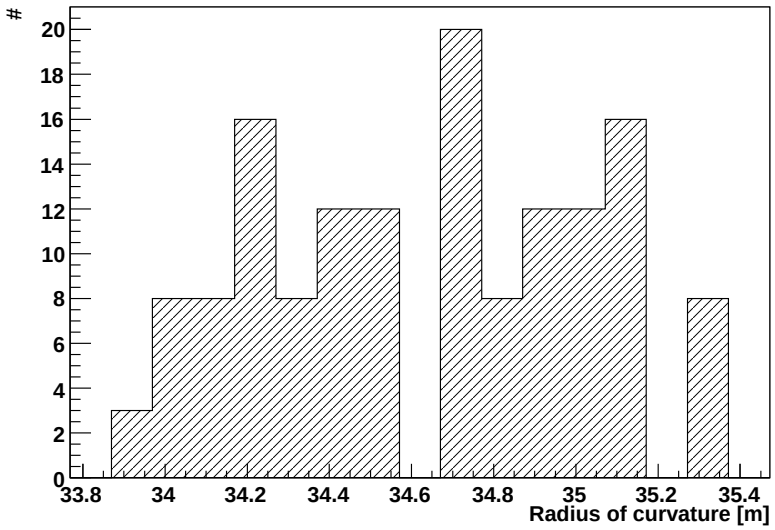

Fig. 2.8: Distribution of the mirror elements with the required radii of curvature

In this way, a parabolic profile can be approximated. Two other requirements concern the optical performance of the mirror elements. These are the spectral reflectivity and the PSF. Within the wavelength range of Cherenkov radiation reaching the ground, the reflectivity should be as high as possible as this assures that the threshold of detection by the PMTs camera is almost unaffected. This is why it must be more than 85 % within the wavelength rang of 320 nm to 600 nm and at least 70 % in the range of 280 nm to 320 nm. The PSF, see section 3.2.2, has to be less than the diameter of a camera pixel, which is $\approx$ 24 mm, otherwise, the detection of low energy showers and hence the imaging would be fuzzy and the γ-hadron separation very much reduced. As the MAGIC telescopes is not protected against bad weather by a dome, the mirror elements have to be weatherproof. One reason for this is that the mirror elements could get damaged by water accumulating in the Hexcell structure, see section 2.5.1, as well as due to freezing during cold nights. Furthermore, the mirror could get too heavy to be controlled by actuators. In addition, the mirror elements should be resistant to chemical damage i.e. Corrosion, as well as to mechanical damage. This is why a protection coating of quartz is required. Since this supplementary layer causes interferences the choice of the thickness is of high relevance. The interference effects should maximise the integral of the product of the detection

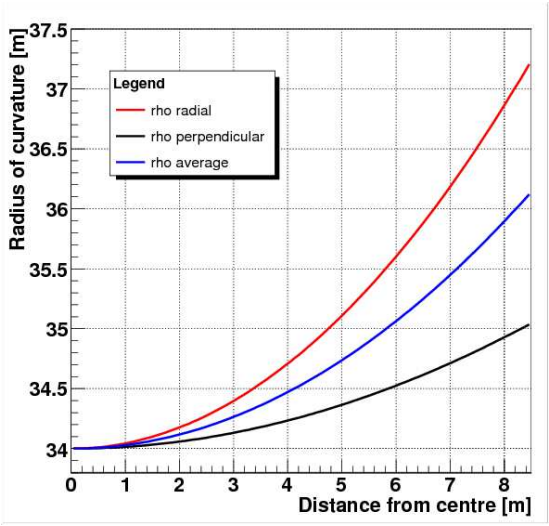

Fig. 2.9: One-dimensional plot of the perpendicular, the radial and the average radius of curvature of a parabolic shape versus the distance to the centre[16].

chain's function. This is given by the convolution of the Cherenkov spectrum, the overall spectral specular reflectivity of the mirror and the QE of the PMTs of the camera. In general the maximal interference should be close to UV part. Consequently, the thickness of the coating must be around 100 nm. The resultant specular reflectivity as a function of wavelength can be seen in figure 2.10.

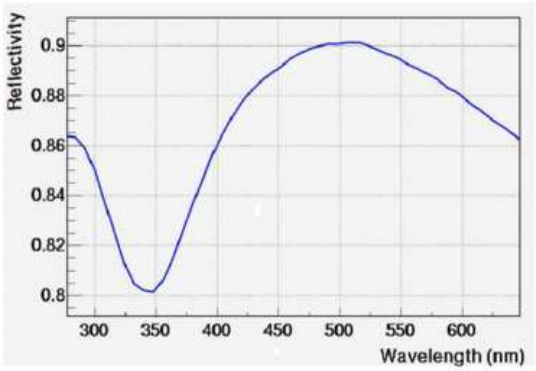

Fig. 2.10: Reflectivity between 190 and 900 nm. In the visible range (290 – 600 nm) the average reflectivity is 86 %. The minimum at about 340 nm originates from destructive interference[4][4].

[4]The calculation of the position of the miminmal reflectivity is described in the appendix C.

Besides these requirements the mirror elements must have a side length slightly below 1 m, i.e., 0,985 m, and a weight below 22 kg. The reason for the limitation of the weight is that for a larger weight the center of gravity will rise above the declination axis and the telescope could get damaged if the altitude drive motor were unpowered and the safety break were to fail[17].

2.5 Production of the All- Aluminium Mirrors

The production of the All-Aluminium mirrors proceeds in three steps. Step One is the production of the raw mirror panels. The other two steps are the diamond milling and the protective coating process. These three processes will be shortly described in this section[16].

2.5.1 Raw Mirror Panel Production

The raw panels are produced in Vicenza by the company Compositex. In figure 2.11 this design is schematically presented. As one can see, the mirror panel consists of different components. The basic construction is a sandwich construction of a solid backplate with side frames (the so-called bottom box) and a diamond machined front plate interspaced by a low density honeycomb and the protective layer for the front side reflective surface.

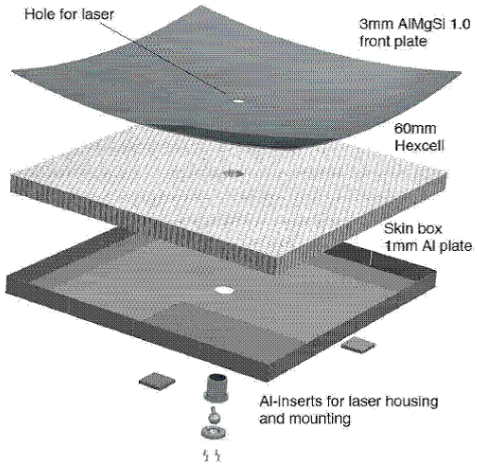

Fig. 2.11: Schematic design of the raw all-aluminium mirror panel[16]

The four major components will be described in the following paragraph.

Bottom box
The bottom box of the mirror element is a 937 x 937 x 62.9 mm aluminium frame. The aluminium alloy is 5754 H111 whose principal alloy component besides aluminium is 2.7 % magnesium. Hence, it features a very good resistance against corrosion. Moreover, the material is easily foldable. The aluminium sheet has a thickness of 2 mm. There are five small equidistant slots at each lateral side of the sheet. These slots are 3 mm wide and 56 mm high. The purpose of the slots is to enable the bending of the bottom box in order to achieve a spherical shape with a radius of 35 m. This mirror component is produced by the company Me.Co.M.

Hexcell Honeycomb core
In order to combine high rigidity and low weight the panels are constructed like a sandwich with a honeycomb spacer with dimensions of 971 x 971 x 60 mm. This material is produced by the company Hexcell. The final shaping and expanding has been done by the Milan company I.Ma.Tec.

Surface skin plate
The surface skin is a 985 x 985 x 3mm reflecting plate of $AlMgSi_1$, type 6082 T6. This alloy has high corrosion resistance and can easily be machined and deformed. It is also deformed to have the same spherical shape as the bottom box and is delivered by Me.Co.M.

Laser Housing
For the active mirror control-see later- a laser pointer is used. This laser pointer is fixed to the mirror in a special housing. The Laser housing is fixed to a hole at the center of the mirror. The hole is machined after the raw mirror is assembled. Two special glues have been used for mirror panel; one for gluing the aluminium components together and the other one for sealing. Aluminium cannot be glued easily because when exposed to the atmosphere immediately a thin layer of Al_2O_3 forms and this layer has (like sapphire) low adhesion to nearly all glues. Normally the aluminium sheets must be pretreated by either etching or with a primer. Both glues are epoxy adhesives of the company Scotch-Weld.

The assembly is performed in five steps which are the following;

1. Cleaning:

Each mirror component is degreased and cleaned with Acetone.

2. Assembly:

The honeycomb, as well as the inserts for mounting, are placed in the bottom box together with a partially pre-reacted thermosetting glue film with the surface skin placed on top.

3. Mould and Vacuum Bag:

The sandwich structure is put on a curved mould. Together they are placed inside a vacuum bag, and a vacuum is created using a vacuum pump.

4. Curing Cycle:

The vacuum bag is placed inside an autoclave for curing the adhesive at high pressure and at about 150 °C for a few hours. After the curing cycle, the raw-blank production is finished

5. Sealing:

The finished raw-blank is then sealed from the outside.

2.5.2 The Milling Process

The final radii of curvature and the highly reflecting surface of the panels are obtained by diamond milling the top sheet[18]. This production step, which is named fly cutter technique, is performed by the German company LT-Ultra. The procedure will be described in greater detail below. In figure 2.14 the schematic setup of the fly cutter technique is shown. The raw panel is mounted on a slowly rotating granite table that rests on an air bearing (for the necessary smoothness and low vibration). The surface of the panel is machined by a diamond mounted on a fast rotating arm (again with the rotation axis running on an air bearing). The rotation axis is slightly inclined. The combination of the rotation of the panel and also of the diamond cutter produce the high precision spherical surface. In this figure, β is the angle of deviation with that of the arbor, called fly cutter and is orientated to the mirror surface. R is the radius of curvature that the mirror must have after this process, and r is the radius of fly circle of the fly cutter. This radius is 75 cm. At the fly cutter, the diamond milling cutter is mounted

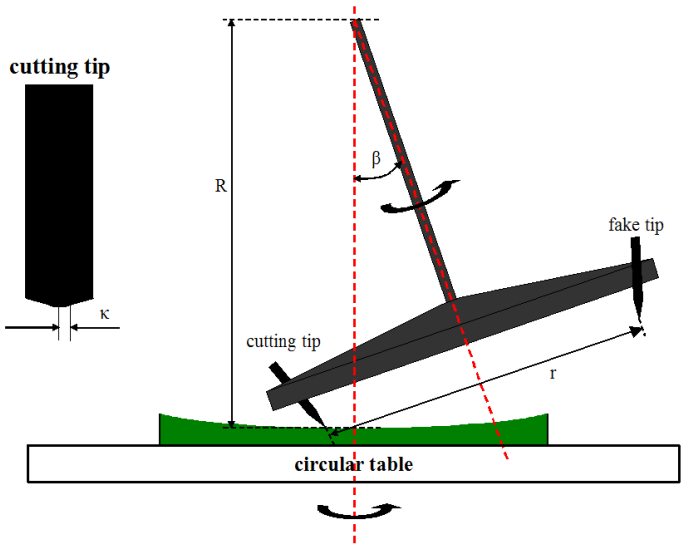

Fig. 2.12: Schematic setup of the milling using a fly cutter: The diamond cutting tip is zoomed in.

and must have a radius of curvature κ of about 100 mm. Considering the ratio of the two radii r and R, the angle of deviation can be calculated.

$$\sin(\beta) = \frac{r}{R} \tag{2.1}$$

This means that one can produce the desired radius of curvature of the mirror element simply by adjusting the angle of deviation. Before the milling process is started, several adjustments must be made so that the following conditions are fulfilled:

- The axis of the circular table and of the arbor have to be in the same plane
- The fly circle has to subtend the circular table's axis at the bottom point
- The center of the mirror has to be at the position of the arbor's axis
- The pivoted axis of the fly cutter has to be perpendicular to the clamping area.

Furthermore, the cutter has to feature a hardness that exceeds that of the thin Al_2O_3 layer formed on the aluminium surface such that its radius, as well as its shape, remain constant during the whole milling . This assures a homogeneously

milled mirror surface. For this reason, the diamond milling cutter is changed each time before starting a new milling process. The speed of the arbor is about 20000 /h, whereas the translate velocity of the positioning stage, on which the mirror is mounted, equates to 1 m/h. One cycle takes about one hour so the overall milling, consisting of several cycles, takes on average twelve hours to complete one mirror, depending on the quality of the surface of the raw panel. During the process the milled material is accumulated on both sides of the milling course. This results in grooves of a certain distance such that the surface has a specific grating structure. Figure 2.13 shows a photo of the fly cutter during the milling process is shown. Due to the velocities of the arbor and the positioning stage,

Fig. 2.13: Photo of the fly cutter while milling a raw mirror panel

the groove distance of the surface is 50 μm. This is also shown in figure 2.14. In order to avoid diffractiondue to a periodic groove structure the operation speed is slightly changed during the process. In doing so, the diffraction can be minimised by destructive interference.

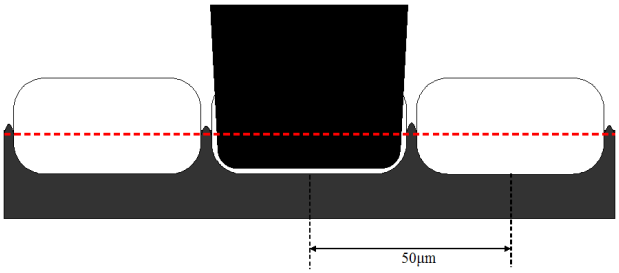

Fig. 2.14: Illustration of the milling on the mirror surfaces: Due to the milling procedure material is cumulated at the side of each groove.

2.5.3 The Coating Process

The last production step is the coating that is is carried out at the Fraunhofer Institute at Bremen[19]. The purpose of the coating is the protection of the reflecting surface against mechanical and chemical damage, weathering or for instance, exposure to acid rain or iron hydroxide containing dust from the Sahara. In addition, the coating provides corrosion protection. The basic component of the coating consists of SiO_2 with some admixture of carbon. The thickness of the protective layer must be 100 nm, as already explained in section 2.4. This coating is deposited by plasma polymerization using the technique of plasma enhanced chemical vapor deposition (PEVCD). Plasma is the fourth aggregate state that describes the state of a gas at a high temperature range. Although the plasma is macroscopically a quasi neutral system, its charged particles interact electromagnetically via coulomb force, which causes the ionization of the gas. In order to sustain the ionization an external supply of energy, either by heat or by electromagnetic radiation, is necessary. In general, the plasma is generated by the use of alternating electric fields. Usually, one divides plasmas into high and low temperature plasmas. The low temperature plasmas are additionally subdivided into thermal and non-thermal plasmas by the operation pressure. Non-thermal plasmas are also called low pressure plasmas. These are used for the coating. The so-called plasma polymerization is a radical initiated polymerization procedure, which enables the coating of a surface. During this chemical reaction the operation gas, which is called precursor, is activated and fragmented by a plasma. During the fragmentation radicals are created which are deposited on the sur-

face. With this dry chemical procedure various organic coatings can be realized. Among the fragmenting plasma polymerization other reactions take place. These are:

- Plasma inducted polymerization
- Reactions within the deposited plasma polymers influenced by the plasma
- Plasma etching

In figure 2.15 these plasma polymerization reactions are presented. Contrary to

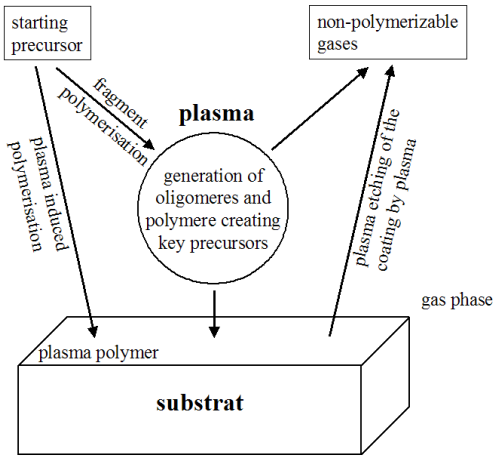

Fig. 2.15: Reactions during fragmenting polymerization[19]

conventional polymers the plasma polymer process generates an amorphous, high molecular weight coating with a statistic molecular distribution. Hence the coating is distinguished by specific properties such as high chemical, mechanical and thermal stability. Therefore, its potential application range covers the following functions:

- barrier layer
- non adhesive,soil-resisting coatings
- anticorrosive coatings
- abrasion-resistant coatings

Figure 2.16 shows the principal setup of the reactor.

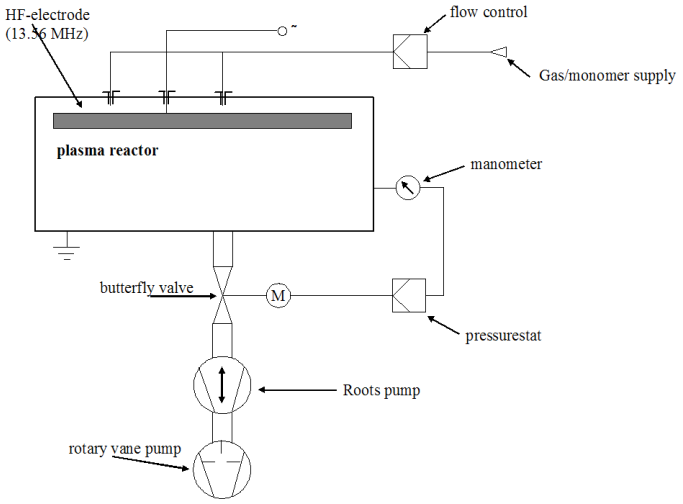

Fig. 2.16: Schematic setup of the process reactor[19]

It comprises an HF generator which is needed for the activation of the plasma. The operation gas is inserted from the top of the reactor via thin, perforated gas pipes. The electrodes, which are function as plasma sources, are situated at the sides of the reactor. The gas enters the reactor perpendicular to these. The direction of the gas flow is from the top to the bottom of the reactor. At the bottom of the reactor a pump system, consisting of a rotary vane pump, a roots pump and a butterfly valve, is installed. This regulates the operation pressure independently of the gas flow. Besides, the measurement of the operation pressure is independent of the used gas whose flow is controlled by mass flow regulation. Figure 2.17 shows a photograph of the above described reactor. During preliminary tests the crucial

Fig. 2.17: Reactor of the coating process[19]

parameters that define the thickness and the homogeneity of the coating have to be determined. Two of these parameters are, for example, coating endurance as well as gas flow. A dummy with the same geometry as the mirror is coated. On its surface 25 small pieces of silicon wafers are mounted of which the deposit thickness is analyzed by interferometry. By means of this procedure the parameters for the most homogenous coating of the desired thickness are optimized. In order to coat four mirrors simultaneously a specific mounting tool is used. The geometry of this mounting tool is shown in figure 2.18. The mounting geometry is optimized

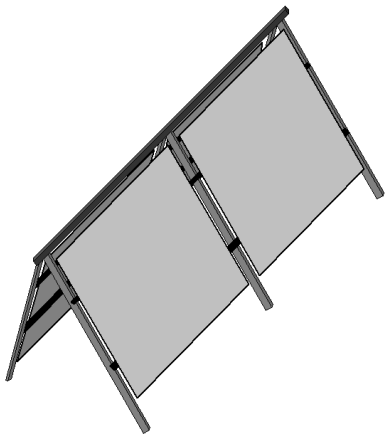

Fig. 2.18: Mirror alignment inside the reactor: Four mirrors are cotaed at a time.

in order to minimize an inhomogeneous coating. This could be caused by small slits between the edges of the mirror and the mounting tool causing possible turbulences in the plasma. As one can see, the mirror surfaces face the respective electrodes. The angle between the surface and the corresponding electrode is 45°. Additionally, the mirror panels are positioned in the middle of the lower two thirds of the reactor. This is because the rate of deposition is still far too close to the electrodes, as well as in the upper third of the reactor. In figure 2.19 one can see that the luminescence of the plasma is less intense close to the electrodes.

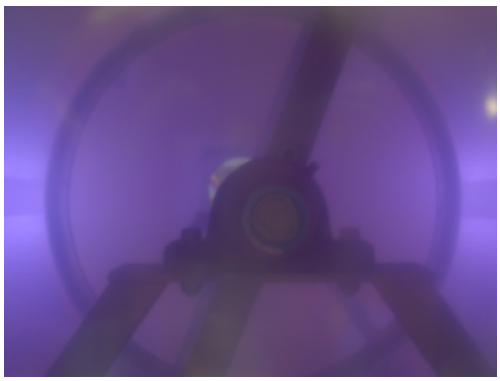

Fig. 2.19: Illustration of the luminescence inside the reactor during the PECVD caused by the plasma: The electrodes are on the left and on the right. The color of the luminescence depends on the composition of the precursor gas.

The reason for this is that the precursor gas is less ionized close to the electrodes. The coating is performed in two steps. First dust is removed from the surface. The second step is represented by the actual coating process. The process procedure starts with the mounting of the mirrors inside a 5000 l reactor, which consists of stainless steel as well as electrodes. After this procedure, air is pumped down until the operation pressure of $2{\cdot}10^{-2}$ mbar is reached. Gaseous hydrogen is inserted into the reactor. After the pressure is again regulated the entire inside the reactor and thus the gas is ionized by an alternating electric field. The thereby generated plasma is used to clean the surface of the mirrors in order to assure a homogenous coating afterwards. After completion of the first step of the coating process the monomer gas for the actual coating is inserted. At the end of this second process step, the electric field is switched off and the inflow of gas is stopped. Finally, the pressure is reset to atmospheric pressure.

3 The Quality Checks of the MAGIC Telescope Mirrors

In the following sections quality checks, which have been carried out to verify that the mirrors meet the afore mentioned requirements, will be presented, , see section 2.4. These requirements concern on the one hand the influence of the environmental on the mirror; on the other hand they are related to the optical parameters of the mirror. For the verification of the optical parameters a charge-coupled device (CCD) camera ST-402ME[20] from Santa Barbara Instrument Group was used. Its CCD chip comprises 510 rows and 765 columns of 9 x 9 μm^2 pixels with a peak quantum efficiency (QE) of nearly 85 %. Furthermore, the CCD camera features color filters, as well as a cooling system allowing one to reduce both the signal noise and the thermal noise. Figure 3.1 shows a photo of the CCD camera. For remote operation the CCDOPS software was used. With

Fig. 3.1: Figure of the used CCD camera ST-402ME

this software, the exposure time of the CCD camera can be set as well as the desired monochromatic filter and the cooling conditions. Moreover, focusing can be adjusted by running the camera in the continuous mode called 'focus'. Figure 3.2 shows the respective dialogue windows for setting the camera parameter.

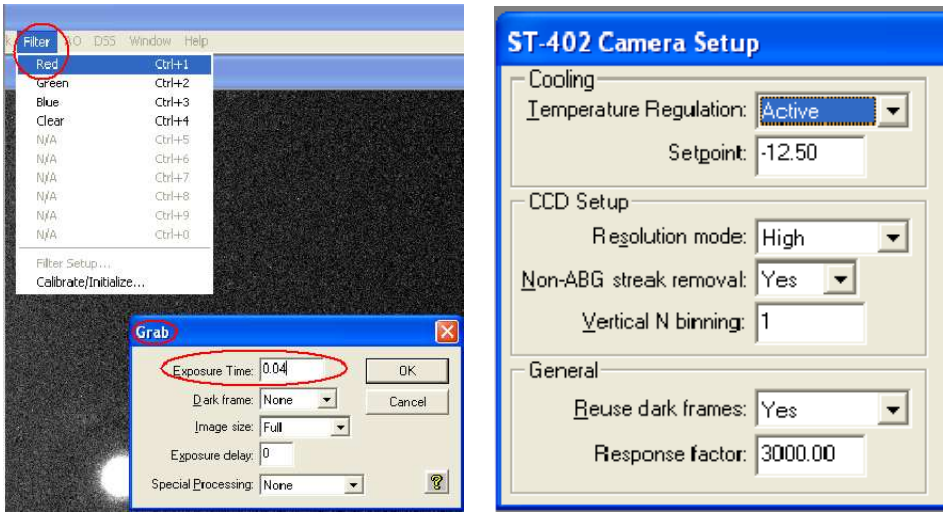

(a) Exposure time and Filter adjustment (b) Cooling system activation

Fig. 3.2: Images of different control panels of the CCD accessory software

Additionally, one can adjust the light sensitivity such that the CCD camera does not saturate for the maximally detectable intensity range. Figure 3.3 shows the corresponding dialogue of the panel. Images are recorded by the so-called 'grab'

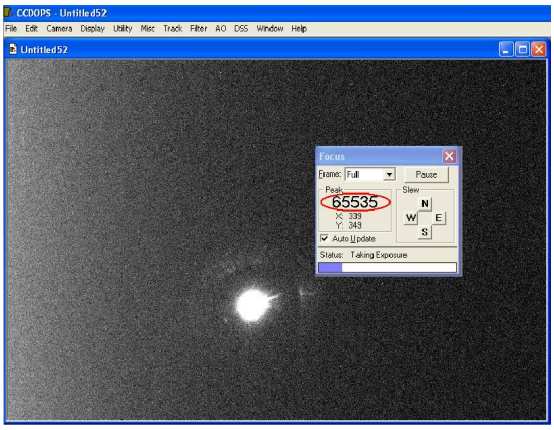

Fig. 3.3: Saturation indicator of the CCD accessory software: The highest detected intensity is indicated. The CCD camera saturates 65535 counts.

mode. The pictures are saved as a SBIG-file. For later analysis these files have to be converted to an ASCII-file. For each signal file an additional background file is recorded for correction purposes. These data are analysed with a procedure written in BASICS and executed by a macro[1]. This reads the data and subtracts the

[1]All macros that have been used for the analysis are written within a software package called

background data. The background distribution can be slightly shifted from zero, i.e. have a baseline offset. This has to be taken into account for the background subtraction. Afterwards a calculation of the detected light intensity is made by summation. Within the summation limits which have to be set manually the respective intensity of each CCD pixel is summed up. For several measurements a screen, consisting of sintered fluoropolymer powder, is used. The material is called: 'Spectralon', which offers a very high diffuse spectral reflectance (98 %) within a wavelength range of 350 to 1000 and shows Lambertian behavior for the angular intensity distribution [21].

3.1 Tests of the Water Tightness of the Mirror Panels

Since MAGIC is not protected by a dome like all optical telescopes the MAGIC mirrors are exposed all the time to the day-to-day atmospheric conditions and are thus sometimes subject to harsh environmental interaction. The telescope site is in La Palma at about 2200 meters altitude. Between October and March it can rain quite frequently and often temperatures during the night drop below zero. It is therefore, important that the mirror panels are watertight; otherwise water could penetrate into the honeycomb cavities of the sandwich structure. During winter nights this water could freeze and hence permanently destroy the mirror by expansion. This problem was observed in the past for some mirrors installed in MAGIC I. Therefore, all the mirror panels have to be tested for water tightness. Another consequence of water filling the sandwich is that the mirrors would become very heavy and could cause problems when mounting. The tests for water tightness are performed using the following procedure. A basin is half filled with warm water. Then, a mirror panel is put into the basin with the reflecting surface facing downwards. The panel is protected against mechanical damages by a rubber layer. The mirror is kept below the water level by two wooden plates, which are fixed to the basin as shown in figure 3.4 According to the ideal gas equation the air located in the mirror heats up, expands and escapes through

Root which is written in C++.

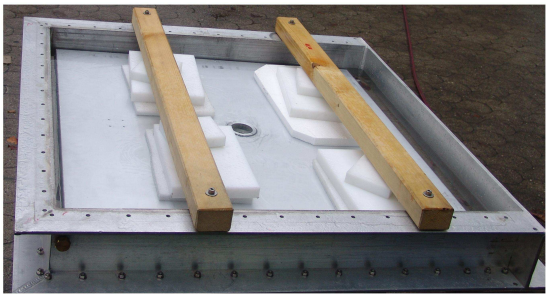

Fig. 3.4: Layout of the basin for water tightness verification

leaks because of the pressure gradient.

$$\frac{p_1}{T_1} = \frac{p_2}{T_2} \tag{3.1}$$

Leaking air can then be seen in the form of bubbles escaping from small holes, as shown in an example in figure 3.5. If a leak is detected, it is sealed with glue

Fig. 3.5: Photo of a leaky mirror in the basin: Bubbles indicate the position of the leak which is red-circled.

and the mirror is tested again after the glue has hardened. This procedure is repeated until the mirror becomes watertight. Most of the mirrors have been found to leak as quite a few tiny holes are formed in the glue lines somewhere in the aluminium frame, see for example, figure 3.6. Other panels have the backside of the aluminium box. These leaks were traced to locations inside the screw holes, which were later used for the mounting of the mirrors panel onto the space frame of the MAGIC telescope. Drilling the holes too deep caused the leaks. Thus, the aluminium frame had been punctured. These leaks were sealed with glue at the

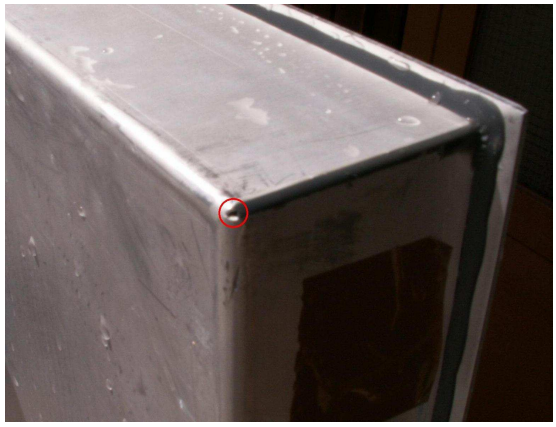

Fig. 3.6: Photo of a leakage being red-circled in the glue line of the mirror's bottom box

time when the mirror panels were mounted onto the telescope. Figure 3.7 shows a pie chart of the different causes of leakage [2].

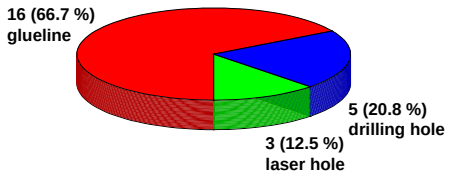

Fig. 3.7: Pie chart of the different leakage causations: Most of the leakages are in glue lines.

3.2 The Panel Radius of Curvature and Point Spread function

Two of the most important parameters of the mirror panels are their radius of curvature and their point spread function (PSF). Therefore, both parameters have

[2]The pie chart presents only the results of the water tightness test for the last 91 mirrors that have been produced.

been measured for each mirror. If the radius of curvature differs by more than 0.5 % from the specified one or if the PSF of the mirror is worse than the required one, the mirror has either to be reworked or in some cases even to be rejected. By evaluating the radius of curvature of a panel one can select the position on which the reflector has to be mounted. Initially one can accept any radius of curvature between 33.8 and 35.8 m but, once the needed number of mirror panels of a given radius is fulfilled, one has in any case to rework the surface. Another reason for this measurement is, that the panel data can be used to improve and fine tune the MC simulation, see section 1.3. The measurement setup and the obtained results are presented in the following sections.

3.2.1 The Measurement of the Radius of Curvature

The mirror panel under test is mounted on a tripod, which is shown in figure 3.8. This tripod is adjustable in height by a few centimetres. In addition, the stand

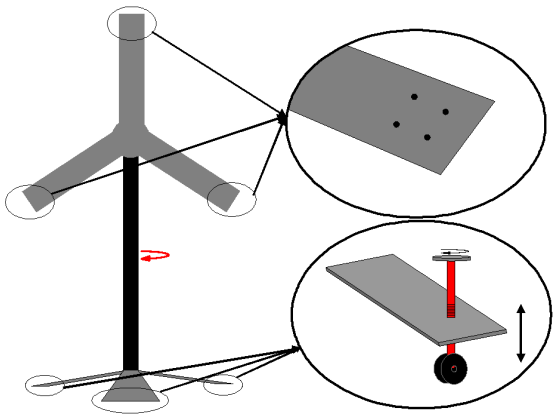

Fig. 3.8: Photograph of the adjustable tripod: The tripod is mounted on wheels. The mirror is fixed at three positions each with four screws

allows one to rotate the mirror panel around the vertical axis. This offers the possibility of changing the mounting position of the mirror in two dimensions. The mirror is mounted via three fixation plates that are attached with four screws to the backside of the mirror. These fixtures are screwed onto the tripod at three different positions. A halogen lamp is installed at a distance of about 34 m from the mirror. This distance corresponds roughly to the radius of curvature of the inner part of the mirror. The lamp with a small pinhole in front of it, is adjusted

such that the entire mirror is illuminated as uniformly as possible. The reflected light is then projected onto a screen made from Spectralon. Shifting the screen forwards or backwards until the image is minimized in its size allows one to determine the focal length f of that element from the distances of the source and the screen. This adjustment was done manually and initially required a lot of fine-tuning. The horizontal and vertical position of the reflected image can be adjusted by position changes of the tripod. The distance p from the screen to the mirror is measured with a laser distance-measuring device, which has an accuracy of 3 mm per 100 m. In addition, the distance q of the light source to the mirror is measured. According to geometrical optics the dependency of these distances p and q, the focal length f is described by the formula

$$\frac{1}{f} = \frac{1}{p} + \frac{1}{q} \,. \tag{3.2}$$

The radius of curvature R equals twice the focal length f of the panel being tested.

$$R = 2f \tag{3.3}$$

Figure 3.9 shows the schematic measurement setup.

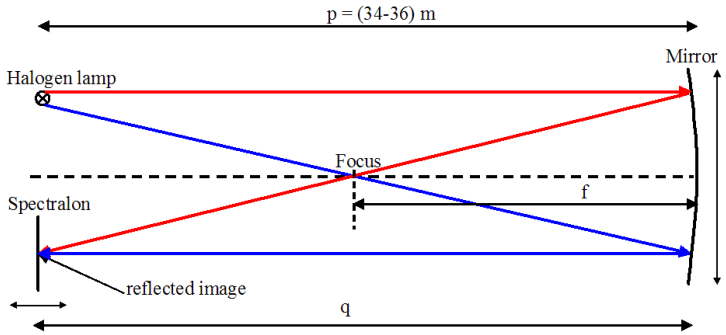

Fig. 3.9: Setup for the measurement of the radius of curvature: The figure is not in scale.

The statistics of the data of a large batch of panels is shown in figure figure 3.10. The histograms show both the needed (calculated) number of panels as the function of the radius and the distribution of the radii of the produced number of panels passing also the acceptance criteria for the PSF. As in figure 2.8, the binning is adjusted in such a manner, that the production accuracy of 15 cm is considered. As one can see, there is a slight difference between the ideal radii and

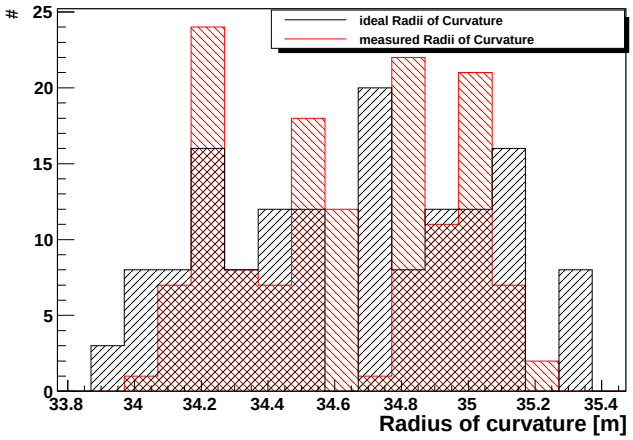

Fig. 3.10: Distribution of the determined radii of curvature: The measured radii of curvature are shaded in red whilst the theoretically calculated ones are shaded in black.

those produced. This difference, however, is tolerable since a divergence of 15 cm for only a few elements causes only a small increase of about 4 mm of the PSF of these panels. The calculation of this increase is illustrated in figure 3.11. By applying intercept theorems the maximal spot enlargement b can be calculated as:

$$b = \frac{d \cdot a}{c} \tag{3.4}$$

,with

$$\begin{aligned} c &= 17 \text{ m} \\ a &= 0.5 \text{ m} \\ d &= 0.15 \text{ m} \, . \end{aligned}$$

As mentioned previously, spherically machined panels positioned off-axis will not

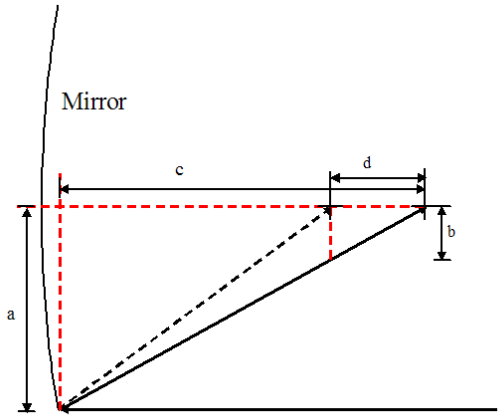

Fig. 3.11: Geometric correlation of the divergence of the radius of curvature and the size of a reflected figure in the focus: a is half of the mirror's lateral length, c equals the focal length f and d represents the production accuracy.

have the same distance for the minimum in spot height in x and y , i.e., F_{x} and F_{y} slightly differ one from the other. So, R_{x} and R_{y} also differs. The reason is an aberration called astigmatism[22], as illustrated in figure 3.12. As a result, the

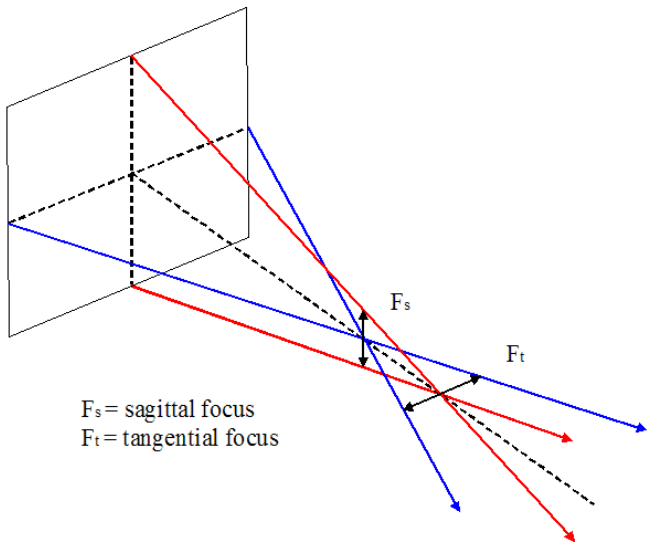

Fig. 3.12: Sketch of the origin of astigmatism: The tangential and the sagittal foci differ one from the other. The reason is a divergence of the ideal spherical shape.

form of the reflected image at best in the x position or y position is not round but elliptic, as one can see in figure 3.13. Most mirrors are not perfectly spheri-

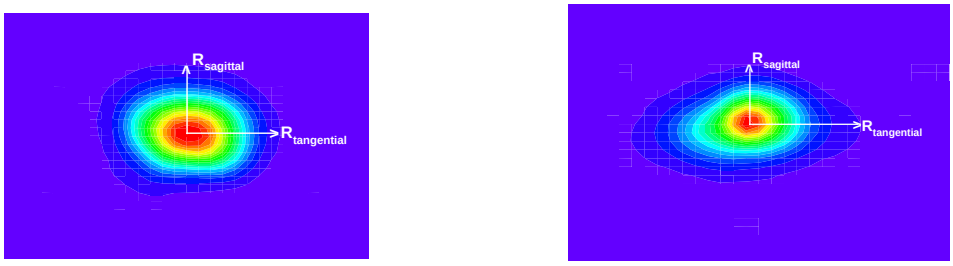

(a) Mirror with little astigmatism produces a round spot

(b) Mirror with astigmatism indicated by an elliptic spot

Fig. 3.13: Comparison of one mirror producing greater astigmatism with another with less astigmatism: The spot radii R_{Sagittal} and $R_{\text{tangemtial}}$ are indicated.

cal after being machined because there is a remaining tension in the aluminium plates that results in a slightly aspherical distortion when taken from the milling machine. One can make use of this defect and find by rotation of the panel often a good minimum of the spot. Colleagues at other institutions have repeated the measurement of the radius of curvature. They used slightly different measurement setups. However, the measurement principle was the same as described above. The acquired results showed a very high consistency with at most a few centimeters difference. It can be concluded that the measurement 'by eye' allows one to determine the radius of curvature of panels with a precision of about 2 cm.

3.2.2 The Point Spread Function Measurement

The PSF[23] describes the response of an imaging system to a point source of light and can be considered as a measure of image blurring. Normally, the PSF of an optical system without any imaging error convoluted with a point source object would again be a point source image. But, due to spherical aberration, which is shown in figure 3.14 and because of diffraction due to surface roughness

the image is blurred. Furthermore, potential divergences of the ideal shape of the

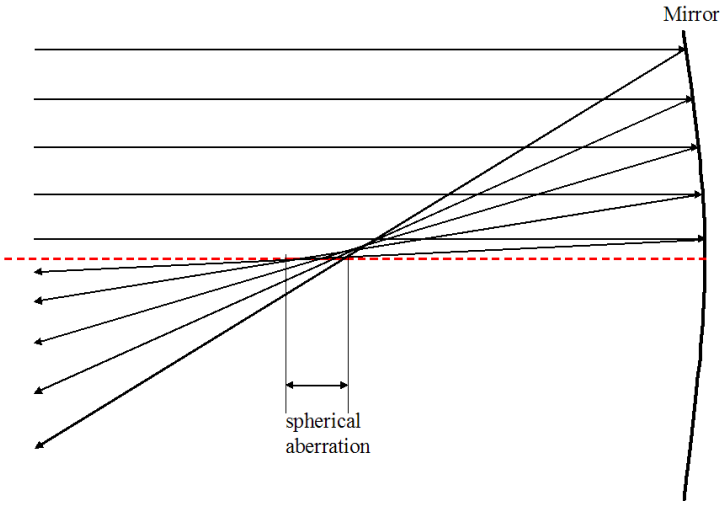

Fig. 3.14: Presentation of spherical aberration of a parallel light beam: The beams that are far from the optical axis have an angle of incident that differs from that of beams close to the optical axis. Consequently they are reflected to slightly differing directions. Thus, the beams do not intersect in one point.

imaging system causes blurring. So, by measuring the PSF of the reflected image of a point source one can draw conclusions on how much the mirror deviates from its ideal spherical shape. The PSF quantifies the imaging error of an optical system and can be described by a parameter called R90. In this case, it specifies the radius in the focal plane of the spherical mirror, which contains 90 % of the reflected light, as shown in figure 3.15. Figure 3.16 shows a three-dimensional illustration of a recorded image, which shows Gaussian behavior. The PSF is analyzed with the same setup as the one used for the measurement of the radius of curvature. As shown in figure 3.17, a CCD Camera is set at about 2 m distance from the target screen perpendicular to the imaging spot on the front surface of the Spectralon. This distance g is also measured. The reflected image is then recorded with the CCD camera and also a background image for which the halogen lamp is screened. The correction of the raw image is made using the subtraction method explained at the beginning of this chapter. The next step in the analysis procedure uses a macro as follows. At first, the center of the light spot image is determined by assuming a Gaussian spot shape for the horizon-

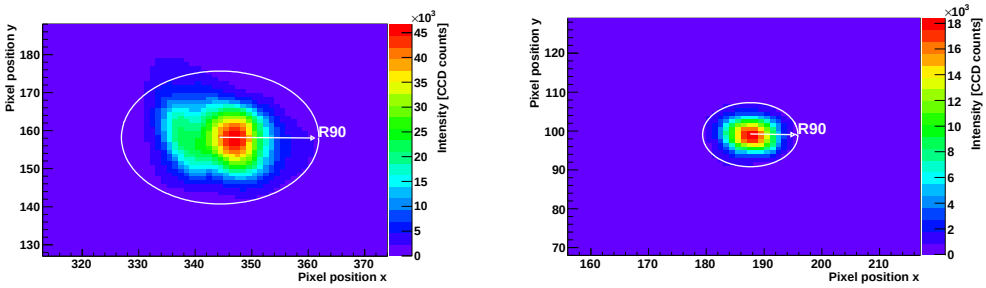

(a) As the spot is not symmetrical, the spot centre is not the geometrical one but the centre of gravity found by a two-dimensional Gaussian fit: The spot radius is larger than R90.

(b) The spot is rotationally symmetric: The spot radius is similar to the R90.

Fig. 3.15: Examples of evaluated R90s for a point light signal reflected from a mirror

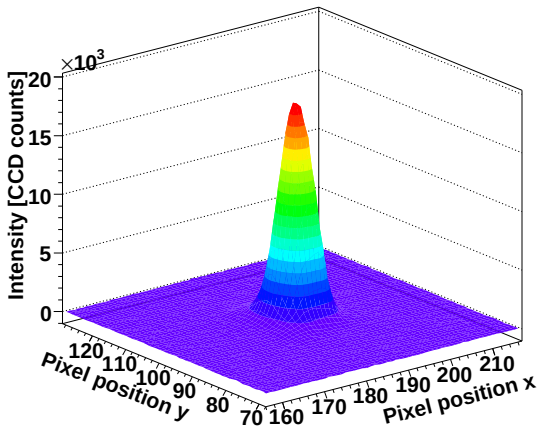

Fig. 3.16: Example of a recorded image with a two-dimensional Gaussian shape: The intensity distribution of the spot is very symmetric.

tal and the vertical intensity distribution. Within a sufficiently wide integration window the intensity is computed by adding up the intensity recorded by each pixel. Then, a radial integration in small steps in r is done, beginning from the determined spot center. The radial distance to the spot center is increased incrementally by one pixel and the integral of the light intensity is evaluated. As the

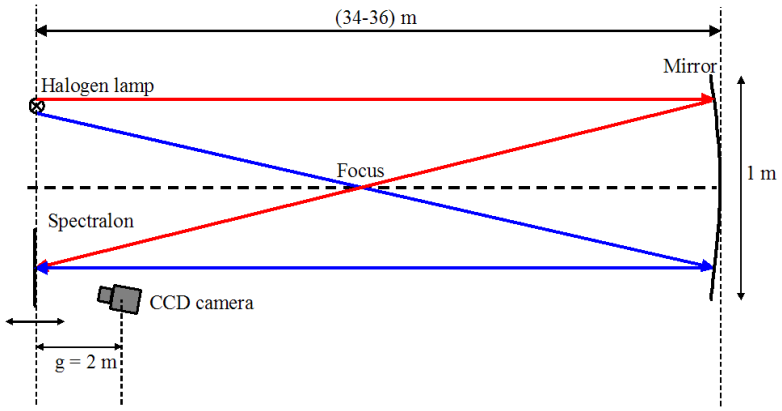

Fig. 3.17: Diagrammatic measurement setup for PSF analysis: The figure is not in scale.

pixel sizes are not infinitesimally small some extrapolation of the pixel area and the fraction of light within the given radius was necessary. If the integral equals nearly 90 % of the total signal the iterative integration is repeated once more. The respective R90 is calculated by interpolating between the previous and the actual radius. In this way the error of R90 can be slightly reduced. Since the unit of the evaluated R90 is defined by the number of pixels, it is finally converted to a metric distance. Therefore, the measured distance of the CCD camera to the Spectralon screen is used for computing the actual size of one pixel. This is done by using the imaging equation for a thin lens. The formal coherence is also illustrated in figure 3.18. The distance b of the image can be computed by the inverse of the subtraction of the inverse distance g of the object from the inverse focal length f of the lens.

$$b = \frac{1}{\frac{1}{f} - \frac{1}{g}} \tag{3.5}$$

The size of the image B can be calculated with the ratio of the distances g and b multiplied by the pixel size G, which is 9 microns according to the intercept theorems.

$$\frac{B}{G} = \frac{g}{b}$$

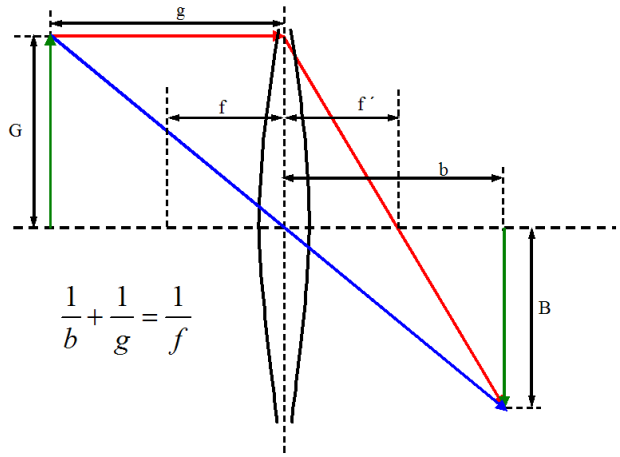

Fig. 3.18: Imaging equation of a thin lens

$$B = 9\mu\text{m}\left(\frac{g}{f} - 1\right) \tag{3.6}$$

In order to verify the correctness of the calculated pixel size, this value is compared to the pixel size that is determined by another procedure. A paper with a known grid of paper is placed on the Spectralon and recorded by the camera. Figure 3.19 shows the recorded image. From the size of one square of the grid, which is 5 x 5

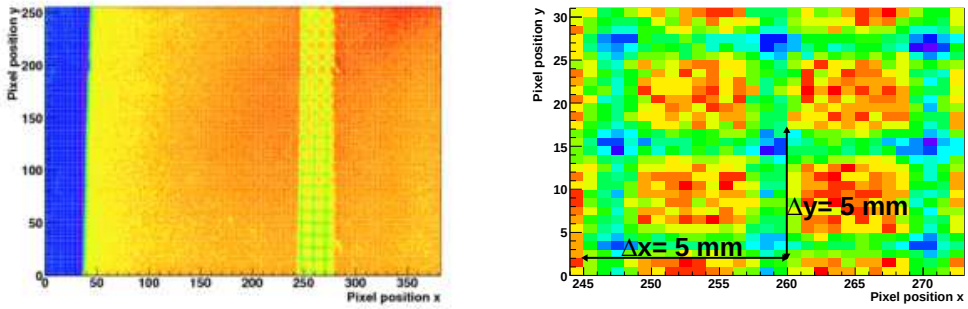

(a) Reference grid for metric pixel size calculation

(b) Zoomed CCD image of the reference grid: The number of pixels of the lateral length of one square equals 5 mm.

Fig. 3.19: Recorded Picture of the reflected Image and the paper grid

mm, one can calculate the pixel size. This is done by counting how many pixels fit along the lateral length of one square. The ratio of the number of pixels Δx and the lateral length (5 mm) equals the metric pixel size. The above mentioned

further calculation is more precise than this evaluation; therefore this method is only used for a crosscheck. The result of the multiplication of the R90 and the pixel size distance equals the metric R90. In figure 3.20 the light intensity versus

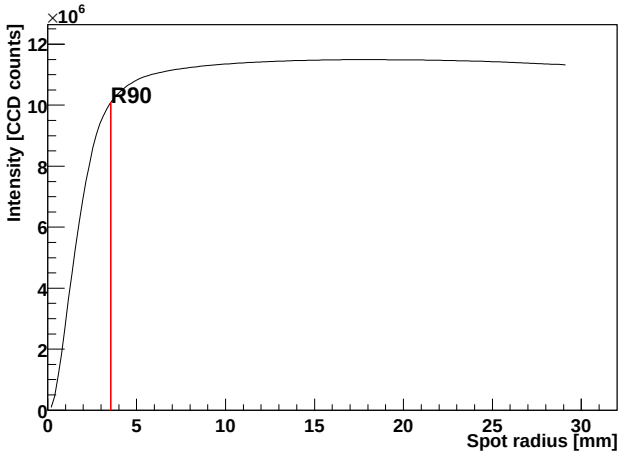

Fig. 3.20: Graphics of the detected light intensity versus distance from the spot's centre of gravity: Rhe R90 is also shown.

distance from the signal maximum is plotted. It affirms, that the evaluated R90 effectively contains 90 % of the reflected light of the mirror. As figure 3.21 shows, the specification for the PSF is much smaller than the radius of the pixel of the MAGIC camera is verified. The average R90 of all mirror panels was determined as

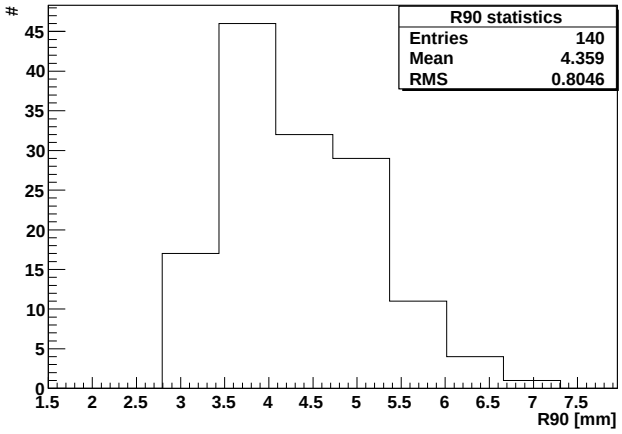

Fig. 3.21: Histogram of the Distribution of the evaluated R90

5.4 mm It affirms that the evaluated R90 effectively contains 90 % of the reflected

light of the mirror. The measurement accuracy, considering the expansion of the 1 cm light source, can be assumed to amount to 0.006 mm, due to the pixel of the CCD camera. Additionally, the error, due to the precision of the determined radius of curvature, which is 2 cm, the precision of the PSF equals in total $\approx$ 1 mm. This is taken into account regarding the binning. The error due to the CCD camera is calculated according to the imaging equation for concave mirrors, see figure 3.22. This can be used to evaluate the error ΔB of the image size B by

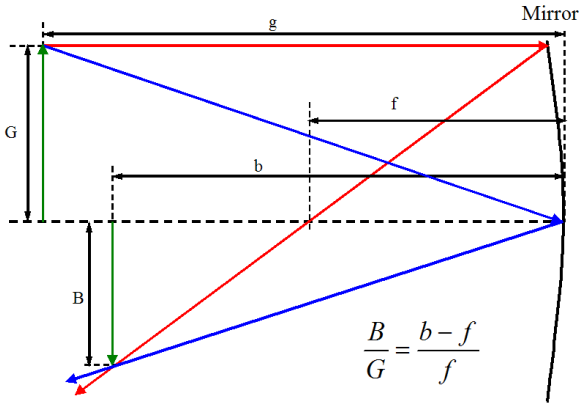

Fig. 3.22: Sketch of the optical path for the imaging of a concave mirror

Gaussian error propagation[24].

$$\Delta B = \frac{G}{f} \cdot |\Delta b| \tag{3.7}$$

Since the PSF and hence the R90 is proportional to the magnification, the error of the R90 is the same as half of the PSF precision. While carrying out the measurement of the PSF we found that some of the light was diffracted. Actually, the first order of diffraction was well visible in some cases, as shown in figure 3.23. Because of this observation further measurements have been made, which will be presented in section 3.4.

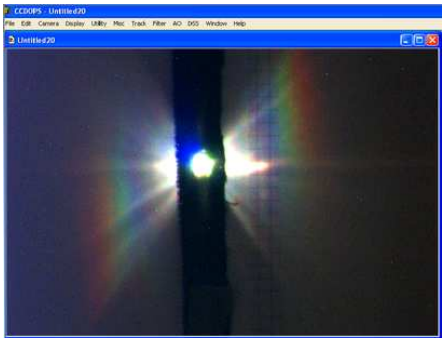

Fig. 3.23: RGB[3] image of the diffraction, observed in the focal plane with the CCD camera: Also, one sees dispersion.

3.3 Specular Reflectivity Spectrum of the Mirror Surface

For the spectral reflectivity of the surface measurement the reflectometer with build-in spectrophotometer Konica Minolta CM-2500d was used; see photograph in figure 3.24. Its mode of operation is appended in section E. The device can

Fig. 3.24: Measurement of a mirror reflectivity with the spectrophotometer CM-2500d

measure both the specular and diffuse reflection between 360 and 750 nm. The specular component is defined as the component, which falls into a cone of either a 2 or 8° radius around the normal reflectance. The measurement in a small cone is necessary because it is practically impossible to perfectly align the mirror under study with the measuring cell inside the device. Both the specular and diffuse reflectance components are shown in figure 3.25. The light source is a wideband

[3]RGB= Red Green Blue

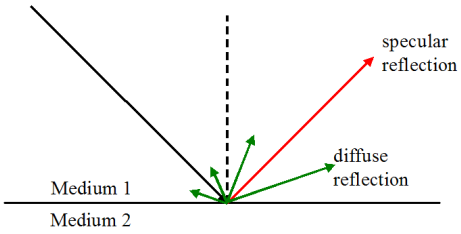

Fig. 3.25: Specular and diffuse components of a surface reflection: The specular component (red) results from the law of reflection. The diffuse component (green) is integrated in all emission angles except in the forward direction.

Xenon flash lamp. A measurement is carried out in the following way. After switching on the device one calibrates over the entire spectral range the 100 % level by using a precisely calibrated diffuse reflector provided by the manufacturer. Then the 'Zero' is calibrated by replacing the reflecting material with a special black standard. Then, the device is placed on a sample to be measured and a small number of light flashes initiated. For each flash the device records the spectra of the diffuse and the specular reflectivity and averages over the preselected number of flashes. Figure 3.26 shows the locations of the measurements on the mirror panel. With this pattern one has a good overview of the reflectivity as a function of the position on the mirror surface.

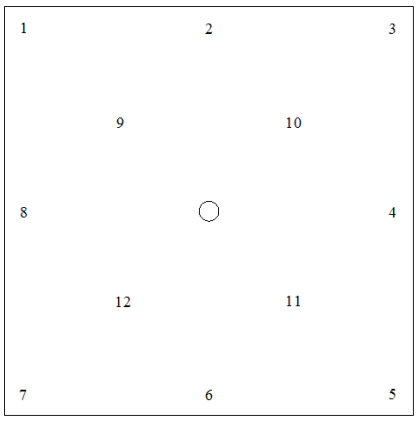

Fig. 3.26: Arrangement of the measurement points over the 1 x 1 m mirror area: For the measurement of the panel reflectivity 12 locations across the mirror were measured.

The final evaluation and tabulation of the reflectivity values was again carried out by a root-macro. This calculates among other things the specular reflectivity and plots it as a function of wavelength, see figure 3.27[4]. As one can see, the

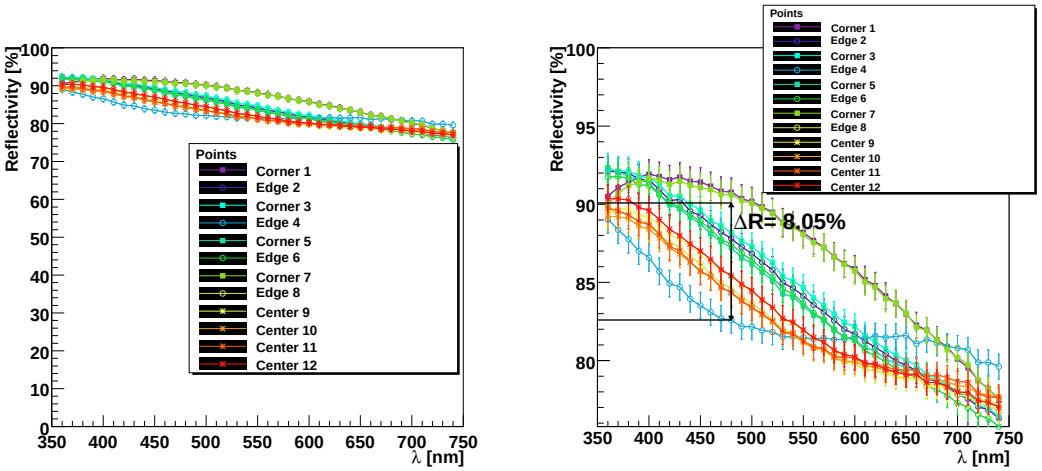

(a) Plot of the measured specular reflectivity versus wavelength. The legend indicates which measurement points belong to which measurement position according to their color

(b) Zoomed and clipped data plot. The differences in the specular reflectivity for one wavelength due to coating thickness variations is about 8 %. The coating thickness is less than about 80 nm.

Fig. 3.27: Plot of the specular reflectivity versus wavelength[5].

variation of the coating thickness induces a variation of the curve of the specular reflectivity spectrum. The coating is usually thinner at the outer regions of the mirror surface due to the production method, see section 2.5.3. Consequently, because of interference effects, the maxima and minima of the specular reflectivity are shifted to longer wavelengths. (Note that due to the limited spectral range of the CD-2500d one does not observe the lowest interference maximum). The area under the reflectivity curves is calculated numerically to obtain the average specular reflectivity of the mirror. This is done according to the trapezoidal rule[24]. Moreover, the spectral reflectivity data are convoluted by the QE of the photo detectors, as well as by the spectrum of the Cherenkov light emission. The resulting values have the dimensions shown in the figure caption, as presented in

[4]The single data points are aligned although the exact course of graph is unknown. The measurement error is specified to be 1 %. Although KONICA specifies a repeatability of 0.2 %[25] the measurements showed a divergence higher than 1 %.

[5]Since there is no explicit maximum or minimum observable, the exact coating thickness is not computable using the reflectivity data. But by comparison with the spectral shape shown in figure fig:requirements5 one can roughly estimate the coating thickness.

figure 3.28. This plot shows that detection is maximal for wavelengths close to UV

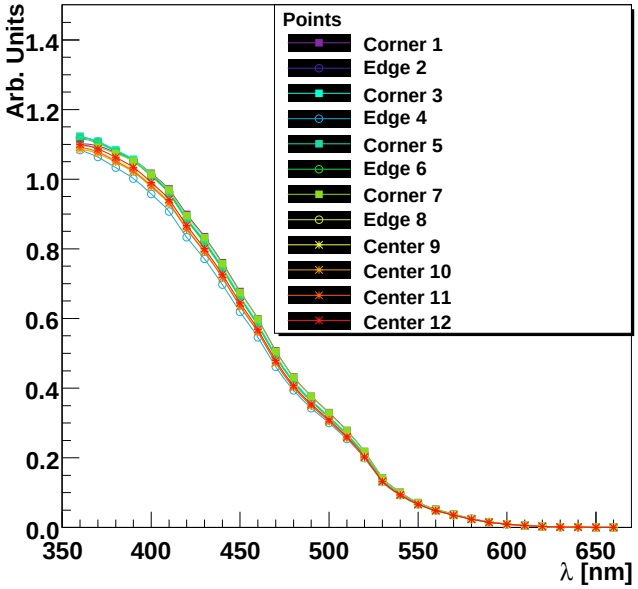

Fig. 3.28: Convolution of the measured reflectivity data with the QE of the PMTs and the Cherenkov emission spectrum: The maximum is located at 350 nm.

as is required for Cherenkov light detection. The comparison of the data shows that the coating process has been optimized to the needs to measure Cherenkov light with PMTs having a bialkali photocathode. It was also found that the homogeneity has been improved for mirrors of later production compared to the production at the beginning[6]. This is confirmed by figure 3.29. As one can see, the position of the maximal reflectivity varies depending on the position on the mirror surface due to different interference effects. This is because of the position that depends on a change in the coating thickness. During the coating process there are turbulences of the coating plasma at the rim of the mirror surface, see section 2.5.3. This is why the coating is thicker at the rim than it is at the centre of the mirror surface. But, since the edges and corners of the mirror surface

[6] At the beginning of the mirror production a coating thickness of 150 nm was chosen to assure a sufficient protection against damage. This however, implied a reflectivity maximum at longer wavelengths than the UV part. This is why the thickness has been reduced to 100 nm, shifting the maximal reflectivity to shorter wavelengths. The thickness variation is more than 40 nm. The coating thickness calculation is done as explained in section C.

[7] The coating thickness for the center of the mirror surface in figure 3.29(a) is about 100 nm.

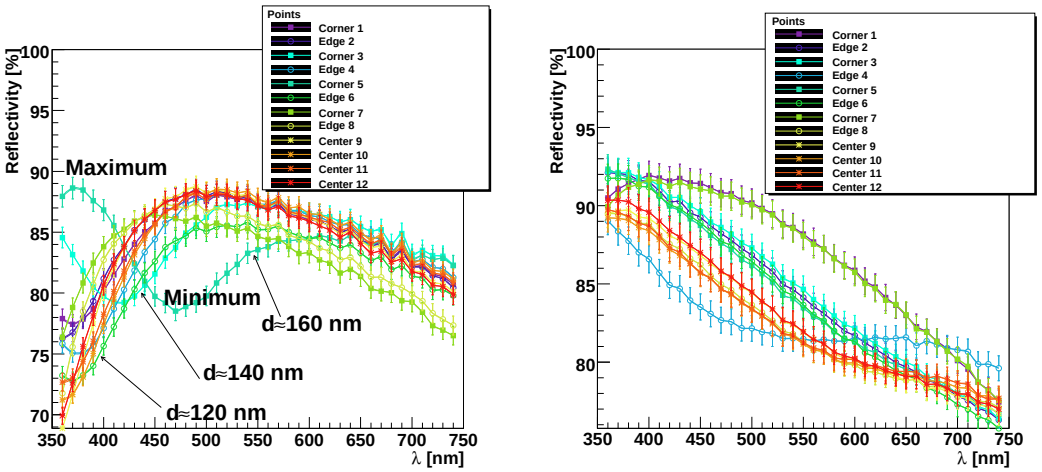

(a) Reflectivity of a mirror from the early phase of production: The coating thickness varies about a few tens of nm depending on the position on the mirror surface. This is the reason why the measured specular reflectivity varies too. The maximum, as well as the minimum result respectively from constructive and destructive interferences.

(b) Reflectivity of a mirror from the later production phase: The coating thickness is more homogeneous.

Fig. 3.29: Comparison of the spectral reflectivity of one mirror from the early production phase with one of the latest production phase[7]

only contribute to a small surface percentage, this shift is insignificant. Since the measurement range of the spectrophotometer extends only down to 360 nm, it is not possible to evaluate the reflectivity at shorter wavelengths[25], but it is possible to compute the average reflectivity of all measurement points over the entire measured wavelength range. One can conclude that, as required, (see section 2.4), the spectral reflectivity is more than 85 % within a wavelength range of 320 nm to 600 nm. At least, this is valid for positions at the center of the mirror. Whether the reflectivity is below 70 % for wavelengths from 280 nm to 320 nm cannot be validated. The results are shown in the distribution of figure 3.30. But, because of ridges aside of the grooves the specular reflectivity decreases due to diffuse reflection. The specular reflectivity loss can be estimated by evaluating the ratio r_{diffuse} of the average ridge width b, reflecting diffusely to the average groove width g, reflecting specularly:

$$r_{\text{diffuse}} = \frac{b}{g} \tag{3.8}$$

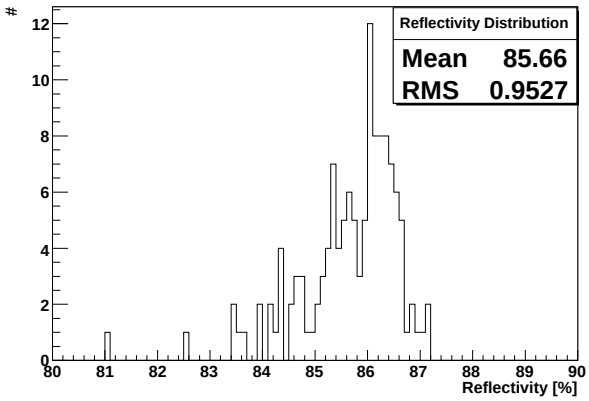

Fig. 3.30: Distribution of the average reflectivity: Binning is chosen arbitrarily.

,with

$$b = 3\ \mu\text{m}$$
$$g = 50\ \mu\text{m}$$

,so that

$$r_{\text{diffuse}} \approx 6\ \% .$$

Thus, assuming linearity between diffuse reflection and the ratio r_{diffuse}, the specular reflectivity is decreased by a diffuse reflection of about 6 %. In addition, a certain fraction $r_{\text{diffracted}}$ of light is diffracted due to the periodic milling grooves functioning as a diffraction grid. Figure 3.31 shows photos of the mirror surface and highlights the grooves due to the milling. These are the areas which cause the diffuse reflection. Thus, the specular reflectivity of the mirror panel is reduced.

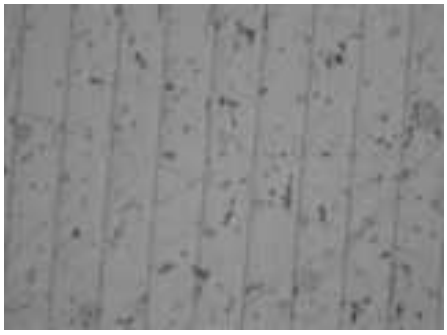

(a) Periodic groove pattern of the mirror surface due to the milling process

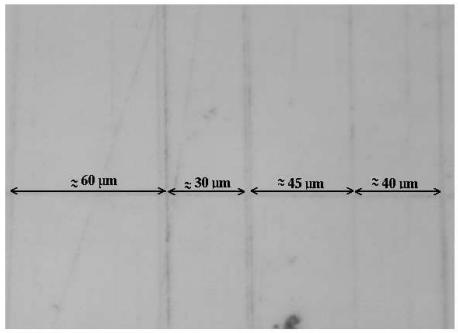

(b) Zoomed and clipped photo of single grooves of slightly differing width

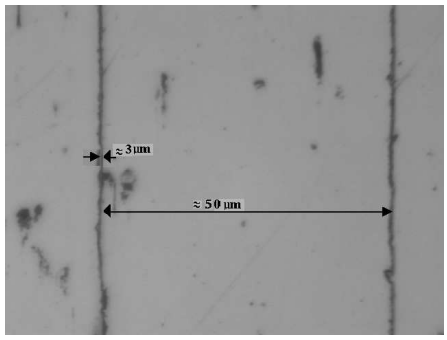

(c) Image of one single groove and: The average width of a ridge (black) aside of a groove is indicated.

Fig. 3.31: Microscopic images of the milled mirror surface: The measured width of a ridge averages 3 μm, the groove width is on average 50 μm.

This in turn, decreases the specular reflectivity too, which will be discussed in the following section.

3.4 Diffraction on the Mirror Surface

A part of the reflected light from the all-aluminium mirror is diffracted. This is because of some unavoidable periodicity due to the grooves caused by the milling. These periodic grooves act as a diffraction grid. It is necessary to estimate the light loss because of higher diffraction orders. The diffracted light could have an influence on the light detectors of the neighboring pixels of the MAGIC II camera. Thus, the distance between two diffraction maxima at the distance of the focal length has to be calculated. Also, the distance of the grooves of the mirror can be verified by measuring the diffraction. The measuring setup is illustrated in figure 3.32. A VCSEL is used as a light source which assures that one can carry

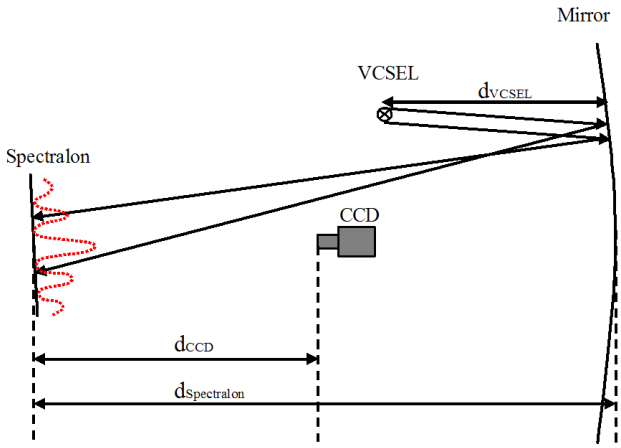

Fig. 3.32: Setup for the diffraction measurement: The figure is not in scale.

out the calculation on the assumption of a small spot source. The VCSEL emits light at 653 nm and has a light beam diameter of about 1 cm. Its light emission is monitored by a PIN photodiode, as described in section 3.5.1. Using a VCSEL one does not need any focusing instruments because the emitted light is almost parallel for a small diameter. The laser is positioned in front of the mirror at a distance of about 1 meter with a small horizontal and vertical angle of incidence. So, one can assume that the diameter of the light spot on the mirror is also about

1cm because the divergence of the VCSEL light beam is very small. Also, the angle of incidence is very small such that the effective light spot area on the mirror surface equals the area of the VCSEL emission area. Thus, the number N of grooves that have been illuminated is about 180[8]. An imaging screen is positioned at some distance from the mirror at which one can easily distinguish the diffraction peaks. The position of the CCD camera with respect to the imaging screen is chosen such that the horizontal and vertical angle of incidence are small and hence insignificant. In addition, it is verified that the CCD camera does not shadow the diffraction pattern which is visible. The measurement is performed in a dark room in order to minimize the stray light contribution. For the analysis of the signal and the background image the same procedure, as explained at the beginning of this chapter, is used. The distance of the CCD camera from the imaging screen, as well as the distance of the Spectralon towards the mirror, are measured. This measurement is repeated for nine different positions on the mirror's surface, as shown in figure 3.33. In doing so, one gets a better overview

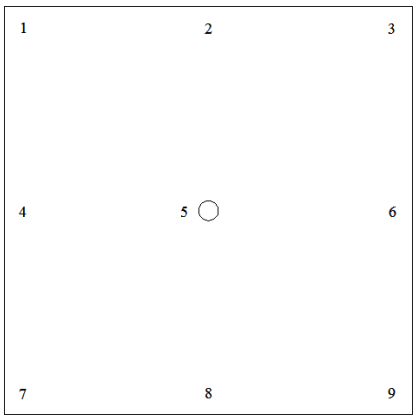

Fig. 3.33: Arrangement of the measurement points on the mirror surface for the diffraction measurement

of the diffraction characteristics of the entire mirror. Since the light source, the CCD camera and the Spectralon are repositioned without changing the respective distances of the light emission, one has to adjust the arrangement only once. Nevertheless, the distances change slightly so that the focusing has to be readjusted for each measurement point. In order to assure the correctness of the measured

[8]The dependency of the groove number N and the diffraction pattern is explained later.

distance to the aperture of the CCD camera, an external aperture is used. The CCD camera can only detect diffraction maxima of sufficiently high intensity. The VCSEL light emission has to be adjusted such that at least the first three diffraction orders can be analyzed. Three peaks are necessary for an adequate estimation of the diffraction. To calculate the fraction of the intensity, which is located in different diffraction orders, the intensity of each diffraction maximum has to be computed. This is done by adding up the pixel intensities belonging to each peak. From the ratio $r(\mathrm{m})$ of the intensity $I(\mathrm{m})$, accordant to the order 'm' of diffraction and the sum of the intensities I_{Total} of all detected diffraction maxima, the fractional intensity distribution can be evaluated.

$$I_{\mathrm{Total}} = \sum_{i=1}^{m} I(\mathrm{i}) \tag{3.9}$$

$$r(\mathrm{m}) = \frac{I(\mathrm{m})}{I_{\mathrm{Total}}} \tag{3.10}$$

As the intensity of the single diffraction orders depends on the inverse square law, the evaluated single ratios $r(\mathrm{m})$ are the same for the focal length f. Figure 3.34 shows such a diffraction pattern. Table 3.1 lists the intensities of the different

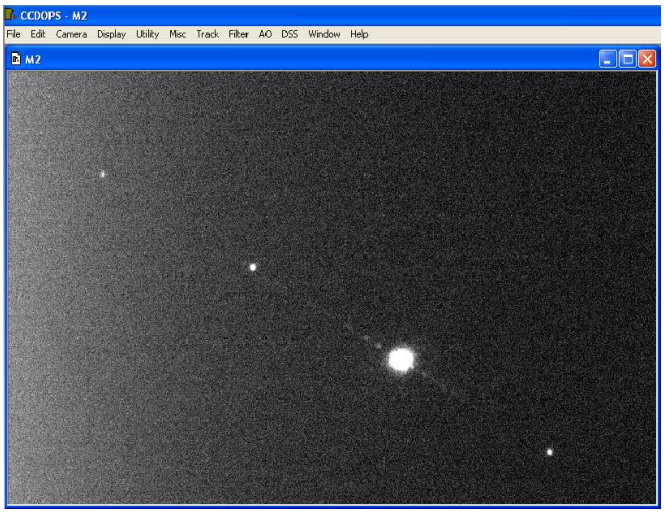

Fig. 3.34: Recorded pattern of diffraction. The CCD camera ST-402ME was used for this measurement.

diffraction maxima for measurement point 2 of two different mirrors.

Intensity [CCD counts]		
diffraction order m	Mirror of average quality	Mirror of good quality
0	$8.2 \cdot 10^5$	$3.3 \cdot 10^6$
1	$99.1 \cdot 10^3$	$3.9 \cdot 10^3$
-1	$6.3 \cdot 10^3$	$4.2 \cdot 10^3$

Tab. 3.1: Presentation of the evaluated intensities $I(\mathrm{m})$ of one measurement point for two mirrors of different quality: m has the values 0, 1 and -1.

The groove distance can be evaluated using vector analysis, as shown in figure 3.35. By determining the coordinates x_m, y_m and $x_{\mathrm{m}-1}$, $y_{\mathrm{m}-1}$ of the centers

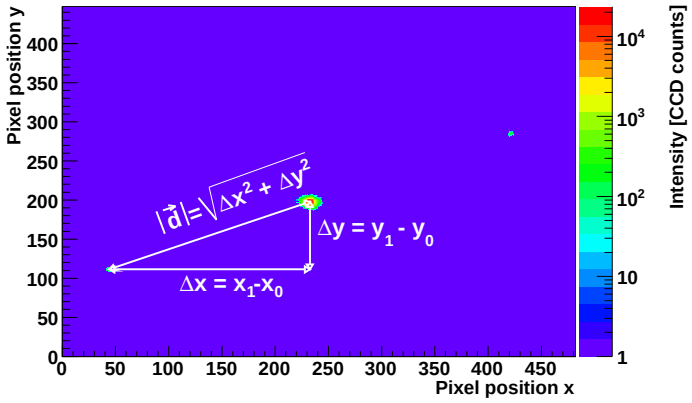

Fig. 3.35: Analysis of the diffraction pattern for the calculation of the distance between two neighboring diffraction maxima: The main maximum and the two first diffraction maxima are shown. The calculation of the distance $|\vec{d}|$ with the unit of the number of pixels by means of vector analysis is also shown.

of two neighboring intensity maxima the distances Δx and Δy can be computed with:

$$\Delta x = x_\mathrm{m} - x_{\mathrm{m}-1} \tag{3.11}$$

$$\Delta y = y_\mathrm{m} - y_{\mathrm{m}-1} \ . \tag{3.12}$$

These distances are converted to metric distances d_x respectively d_y by multipli-

cation with the real pixel size p according to section 3.2.2.

$$d_{\mathrm{x}} = \Delta x \cdot p \tag{3.13}$$

The norm of the resulting vector equals the real distance $|\vec{d_{\mathrm{metric}}}|$ between the different diffraction maxima.

$$|\vec{d_{\mathrm{metric}}}| = \sqrt{d_{\mathrm{x}}^2 + d_{\mathrm{y}}^2} \tag{3.14}$$

According to the theorem of intersecting lines, the distance of two neighboring diffraction maxima at the focus can be computed by the ratio of the focal length f of the mirror and the distance $d_{\mathrm{Spectralon}}$ of the Spectralon to the mirror multiplied by the evaluated metric distance of the diffraction maxima $|\vec{d_{\mathrm{metric}}}|$

$$|\vec{d_{\mathrm{Focus}}}| = \frac{|\vec{d_{\mathrm{metric}}}| \cdot f}{d_{\mathrm{Spectralon}}} \tag{3.15}$$

The assumption is that the contribution to the total light intensity will be negligible for diffraction orders for which m is larger than ± 1. Therefore, this calculation has been made only for the main maximum and both the first diffraction maxima[9]. Figure 3.36 shows the main maximum and one first maximum in two- as well as in three-dimensional. The groove distance g for which interferences are constructive can be calculated by the division of the wavelength λ of the light source by the sinus of the angle of observation α as shown in figure 3.37.

$$g = \frac{m \cdot \lambda}{\sin(\alpha)} \tag{3.16}$$

The angle of observation α depends on the respective diffraction order m. This can be evaluated by applying trigonometric rules.

$$\alpha = \arctan\left(\frac{|\vec{d_{\mathrm{metric}}}|}{d_{\mathrm{CCD}}}\right) \tag{3.17}$$

As this evaluation has been made only for the diffraction maxima of the first order m equals to 1 respectively to -1. This measurement has been done for three

[9]The calculation has also been made for diffraction orders up to m ± 2. The total light fraction being located in these diffraction orders well below 1 %.

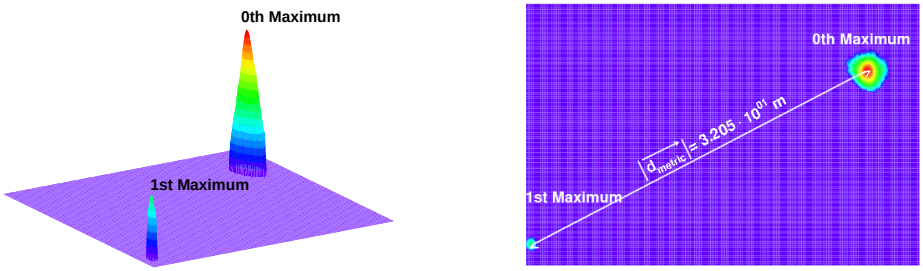

(a) Three-dimensional presentation: The peak intensity, detected in the first diffraction maximum is much lower than the main maximum.

(b) Two-dimensional presentation: The metric distance is indicated.

Fig. 3.36: Two-dimensional and three-dimensional logarithmic presentation of the main (0th) maximum and one first diffraction maximum: Both spots show very good symmetry of rotation.

different mirrors. Depending on the quality of the mirror surface the detected diffraction patterns differ significantly, which is proven by the different results for the ratio of the located light intensity in different diffraction maxima. Also, the number of diffraction orders depends on the quality of the mirror's surface. According to the measurement position the pattern of the single maxima differs. At the corner of the mirror surface the milling grooves have a curved shape, as one can see in figure 3.38. This is because the diamond milling head rotates across the surface, as explained in section 2.5.2[10]. Consequently, the recorded diffraction pattern orders are arranged diagonally. By contrast, the diffraction pattern is rather horizontal because the grooves in the mirror centre run almost parallel. Additionally, the roughness varies between 50 μm and 70 μm depending on the position on the mirror surface. This is caused by the production procedure. The diamond cutter needs a certain time for removing material from the mirror surface at one position while less material is removed when the mirror is moved forward underneath the fly cutter at another position of the mirror. The grooves could also have substructures caused by the shape of the diamond cutter. These substructures cause additional diffraction such that the measured main diffraction maxima are blurred, see figure 3.39. By contrast, if the surface is very homogeneous, the diffraction pattern is characterized by small, exactly bordered

[10]In figure 3.73 in section 3.5.2.1 one can see the course of the grooves along the mirror surface.

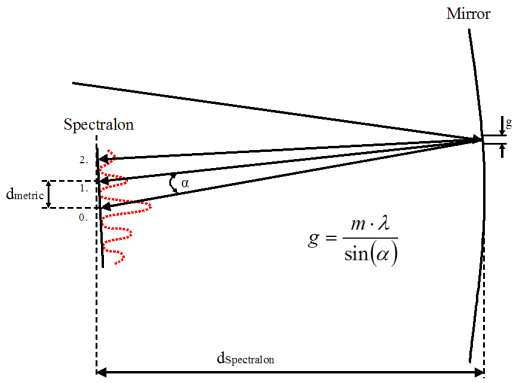

Fig. 3.37: Optical path for a diffraction at a grid: The calculation of the groove distance g of the mirror surface by means of diffraction criteria is shown.

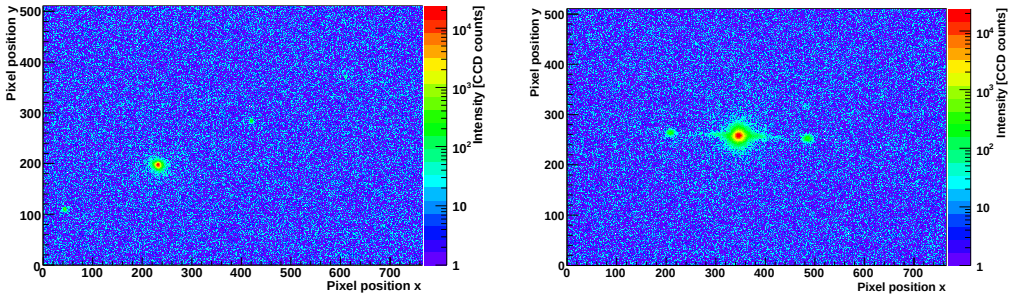

(a) Diagonal diffraction pattern of a position at the mirror surface corner: Here the milling grooves are slightly bent because of the rotation of the fly cutter.

(b) Horizontal diffraction pattern of a position at the mirror surface centre: The grooves run almost parallel.

Fig. 3.38: Comparison of two different diffraction patterns, one at the mirror corner and one in the mirror centre.

maxima, as shown above. Furthermore, the number of grooves N functioning as a grid has an impact on the amplitude of the single diffraction maxima. The reason is that the amplitude A is proportional to the number of grooves N squared because of the so-called function of interference[22].

$$A \sim N^2 \tag{3.18}$$

Moreover the width b of the diffraction maxima is reciprocally proportional to

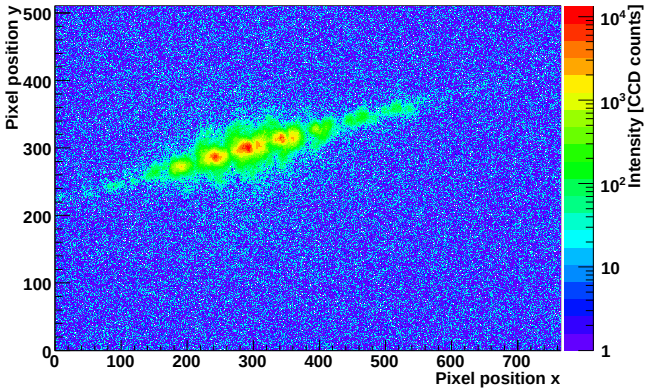

Fig. 3.39: Blurred diffraction pattern of a mirror surface of bad quality: The single diffraction maxima merge.

the number N of grooves.

$$b \sim \frac{1}{N} \tag{3.19}$$

Hence, the more sharper diffraction orders are visible, the more grooves, illuminated by the laser, are periodic. It is remarkable that one mirror only showed a few or even no diffraction at all across its entire surface. Figure 3.40 shows such an example. In table 3.2 the evaluated intensity ratios of two mirrors of different

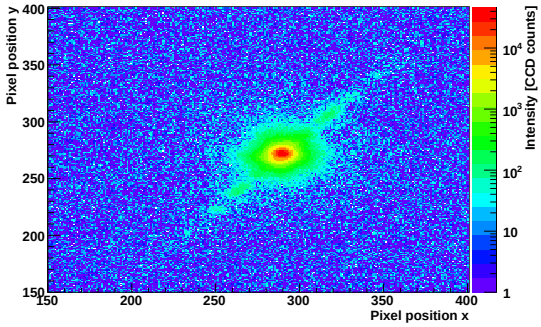

Fig. 3.40: Diffraction pattern of a mirror surface of good quality: One can see only a slight blurr of the main maximum and there are no diffraction maxima. The main maximum is only slightly diagonally enlarged.

quality are listed. On average, the amount of light that is present in the two first diffraction orders varies between less than 1 % and almost 5 % depending on the

position	Intensity fraction [%]			
	Mirror of average quality		Mirror of good quality	
	main maximum	subordinate maxima	main maximum	subordinate maxima
1	98.17	1.83	100	n/
2	97.12	2.88	99.75	0.25
3	97.09	2.91	100	n/a
4	95.41	4.59	99.44	0.56
5	95.79	4.21	99.79	0.21
6	n/c	n/c	99.29	0.71
7	n/c	n/c	100	n/a
8	n/c	n/c	100	n/a
9	n/c	n/c	100	n/a

Tab. 3.2: Comparison of the calculated intensity ratios of two mirrors of different quality: For the subordinate maxima m equals ± 1. The indication n/a means that no significant diffraction was measurable. When the ratios could not be calculated because the diffraction pattern was blurred, an n/c is marked.

position on the mirror surface and on the surface quality. For some positions the calculation could not be made because the single diffraction orders were not distinguishable from each other. The distance between the main maximum and both first diffraction orders in the focal plane varies between 15 to 20 cm depending on the groove distance. This is more than the pixel diameter of the MAGIC camera. However, diffraction can be considered as not too important because of the rather low rate of intensity that is located in the first maxima. But, this result implies that the reflected light in the focus is not all concentrated in one spot and the measurement of the mirror reflectivity measured directly on the mirror surface gives a value that is too high. If both diffraction and diffuse reflection are taken into account then a total reduction of about 11 %[11] This has been verified by measuring a parameter called focused reflectivity. The measurement procedure and the obtained results will be presented in the following section.

[11]Since this measurement has only been performed with a laser at 653 nm, one can only assume that the loss by diffraction is the same for other wavelengths. This still has to be determined by some other measurements for the specular reflectivity is expected.

3.5 The Focused Reflectivity

In section 3.3 the method and the results of the measurement of the specular reflectivity of the mirror surface have been presented. It is also important to know how much of the light reflected by the surface will actually be located in a small spot on the focal plane. As explained in the previous section, the total amount of reflected specular light will be reduced by diffraction and scattering. As explained in the previous sections 3.3 and 3.4, the estimation is a total loss of specular reflectivity of about 11 %. That means that the measured specular reflectivity of 86 %, e.g. at 620 nm, drops to 75 %. This might be confusing for the reader because the name 'specular' should refer only to the light focused onto a small spot on the focal plane. The confusion comes from the fact that the used Minolta instrument uses the definition of specular light for light collected within a cone of 2° radius around the normal reflection, i.e., this cone contains still some light from small off-axis angles. In this section a new parameter is introduced called focused reflectivity. It refers to the amount of reflected light in an area defined by the PSF on the mirror focal plane. The focused reflectivity is a very crucial parameter as it has to be used for the MC simulation comparison with real data. In order to exclude potential errors in the measurement setup several reference tests have been performed to cross-check the standard measuring procedure. These tests will be presented in the following

3.5.1 Reference Measurements

Since the measurement of the focused reflectivity is carried out with the CCD Camera, its parameters such as focusing, exposure time and aperture influence the measured light, losses have to be measured. Also, the directional characteristic, as well as the reflectivity of the Spectralon have an impact on the computation of the focused reflectivity. Moreover, the validity of distance law for the setup for the measurement of the focused reflectivity needs to be verified. The setup, which has been used for reference measurements, is shown in figure 3.41[12]. The

[12]Only the analysis of the influence of the exposure time and the directional characteristic have been measured with a slightly different setup. This will be explained in further detail in the respective sections 3.5.1.1 and 3.5.1.5.

CCD camera is mounted on an optical bench. The Spectralon is fixed with a

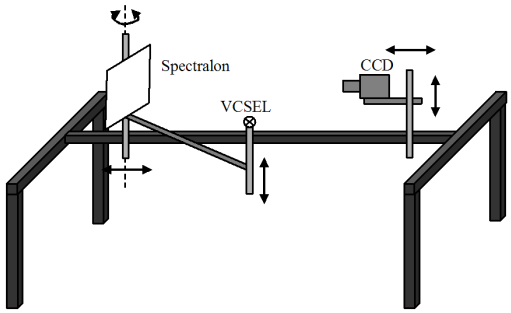

Fig. 3.41: Setup for the reference measurements

clamp that can be moved along the optical bench. In addition, this clamp can be pivoted in two directions. A scale is added to the clamp to read the angular position. As for the diffraction measurement, see section 3.4, the VCSEL laser is used as a light source. An additional advantage of the VCSEL is that its light emission is quite stable. This has been proved with another test. In figure 3.42 one can see the photo current that was measured by a PIN photodiode. The observed

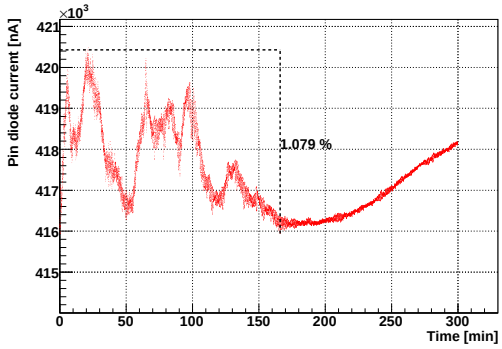

Fig. 3.42: Plot of the light emission fluctuation of the VCSEL: The maximal divergence of the light emission is about 1 %.

light output of the VCSEL varies only by about 1.1 %. The VCSEL can either be mounted on a second pivoted clamp or it can be fixed on the same clamp as the Spectralon depending on the measurement. In both cases, the light source is positioned in front of the Spectralon with a gallows construction. For most of the measurements the angle between the CCD camera and the Spectralon is 0°. Hence, the angle of incidence of the VCSEL is adjusted in such a manner

that its light beam does not interfere with the body of the CCD camera. Since the angle of incidence does not change during each measurement except for the analysis of the directional characteristic (see section 3.5.1.5),its impact on the measurement can be neglected. A part of the parallel light beam emitted by the VCSEL is directed to a PIN photodiode with a beam splitter, as shown in figure 3.43. Its current is amplified by an operation amplifier and read out with

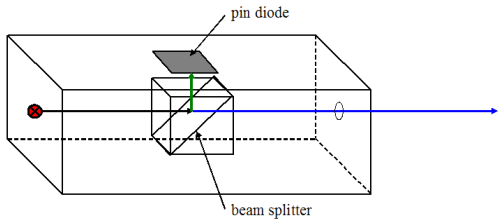

Fig. 3.43: Setup for the light emission monitoring: A beam splitter is used to reflect a certain part of the emitted light on a pindiode. The pindiode current in return is read out with a multimeter and additional software. In this way, the light emission can be monitored during the measurement by means of the pindiode current.

a multimeter at intervals of one second. This in turn is attached to a computer. With a corresponding software the multimeter is remote-controlled. The acquired data are recorded with this software and are later saved to a txt-file. Figure 3.44 shows the remote control panel. At the end of each measurement the time of the recorded signal picture is compared with that of the recorded pindiode current using a macro. This selects the pindiode current which has been detected at the point of time of data acquisition and writes it into a file. In this way, one can check later whether potential divergences of the detected light intensities have been caused by light emission fluctuation indicated by large fluctuations of the detected pindiode current. Furthermore, assuming a proportionality between the fluctuation of the pindiode current and the emitted light intensity one can determine the maximal relative error. Measurements were performed in a dark room with the purpose to improve the signal-to-noise ratio.

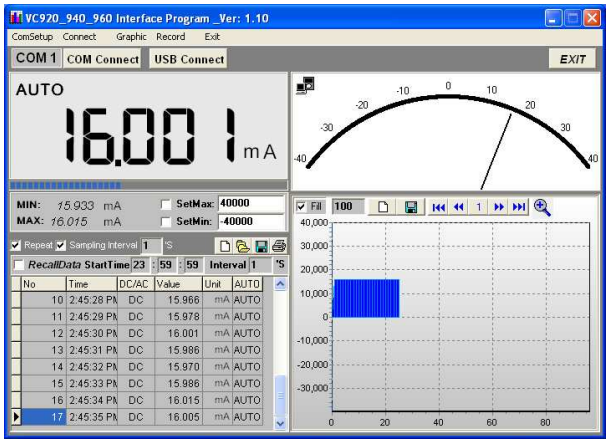

Fig. 3.44: Illustration of the remote control panel of the light emission monitoring: The measured pindiode current is displayed in four different ways, as a single number, as a tabular, as a graph and as an analogue display.

3.5.1.1 Influence of the Exposure Time

One important camera parameter is the exposure time. The following measurement was performed to verify that the intensity of the CCD camera is proportional to the exposure time. As the range of the emitted light intensity of the laser is too faint, this measurement was performed with an LED, detecting directly the light emission without any imaging screen, As pretest of several hours showed, the light emission of the LED fluctuates around 5 %. The figure of the data acquired with a pindiode is presented in figure 3.45. It shows the detected pindiode current versus elapsed measurement time. Probably, these fluctuations are caused both by oscillation of the voltage supply of the light source and by variation of the ambient temperature[13]. Therefore, the LED is operated with a constant current source. There are two reasons for doing so. First, this reduces the fluctuation to a value of less than 1 % which is probably just caused by temperature variations. Figure 3.46 shows the detected pindiode current versus elapsed measurement time. Secondly, because of the exponential shape of the LED's characteristic line it is better to operate the LED with current for its variations generate only a slight fluctuation of the voltage. Apart from these two reasons there is another advantage provided by the constant current source. Since it features a continuous potentiometer, the

[13]The elimination of emission fluctuation due to temperature variation is in this case not possible.

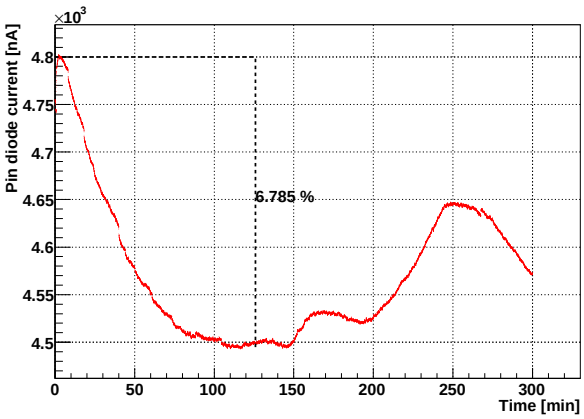

Fig. 3.45: Measured fluctuation of the light emission of an LED operated with a constant voltage power supply: The Peak at the beginning of the measurement could have been the effect of a stabilization phase. The maximal divergence of the light emission is almost 7 %.

adjustment of the light emission is more precise. The constant current source can be operated with a maximal 10 V of a power supply. The output of the constant current source is an appropriate current. The entire measurement is performed with maximal opened aperture. In addition, the camera is focused on the light source. The exposure time is first set to 60 seconds. Then, the light emission of the LED is adjusted to a value for which the CCD camera is just below saturation. For these settings, a signal and a background image are recorded. For the background image the LED is shut. Afterwards, the exposure time is decreased, first in a step size of 5 seconds later in a smaller step size, until the detected light

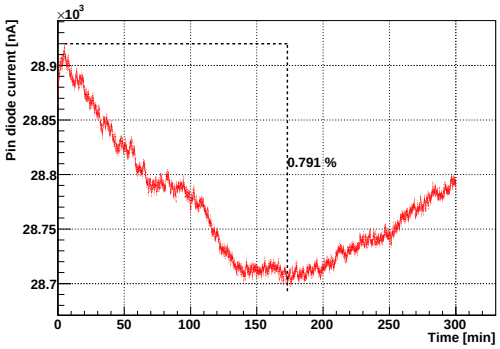

Fig. 3.46: Measured fluctuation of the light emission of an LED operated with a constant current source: The maximal divergence is less than 1%.

intensity differs only marginally from the background. For the respective exposure the measurement is repeated twice in order to have an overlap of the data measurement. Once, it is performed with the precedent settings, the second time the LED emission is increased until the CCD camera just does not saturate. This measurement procedure is repeated until the minimum exposure time is reached. The step size is lowered according to the exposure time. The data are read out afterwards with the macro mentioned in the beginning of this chapter. The integration limits for the evaluation of the detected light intensity are set for the longest exposure time. With this procedure the complete range of the exposure time is covered and hence, the data are comparable. As one can see in figure 3.47, the assumption of a linear dependency between exposure time and detected light intensity is fulfilled. However, one can also see from figure 3.48 that the assump-

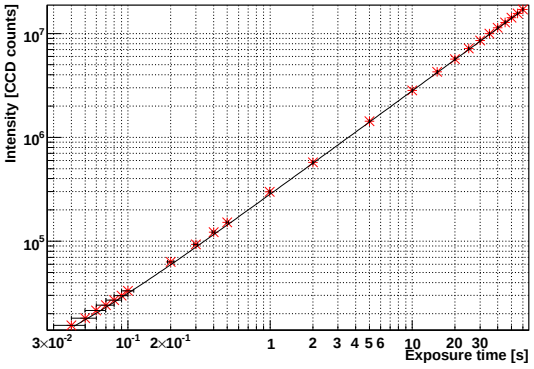

Fig. 3.47: Logarithmic presentation of the exposure time data analysis: The data are fit with a one-degree polynomial. Due to the defective exposure time the data differ from the fit for shorter exposure times.

tion of a proportionality is not correct for shorter exposure times. This is why the time-normalized intensity is not constant, although it should be. A possible reason therefore could be that the speed of the electromechanical shutter is too slow so that the actual exposure time is slightly longer than the indicated one. That would mean that the exposure time is afflicted with a constant error. By fitting the data with a linear function this error can be determined. The exposure time error is the intersection with the x-axis of the graph. This can be computed with the obtained fit parameter. If this error is taken into account, the linearity is also valid for shorter exposure times. Figure 3.49 affirms this result. The time error is about 0.01 seconds. This is why shorter exposure times are more afflicted

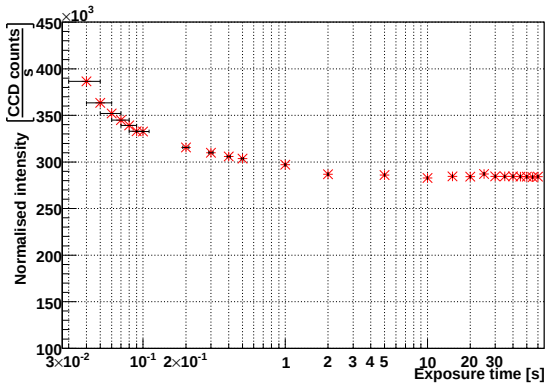

Fig. 3.48: Figure of the exposure time-normalized light intensity versus exposure time: The time-normalized intensity is too high for short exposure times. For long exposure times the time-normalized intensity is constant as expected.

than longer ones. This measurement was repeated three times. The resulting time

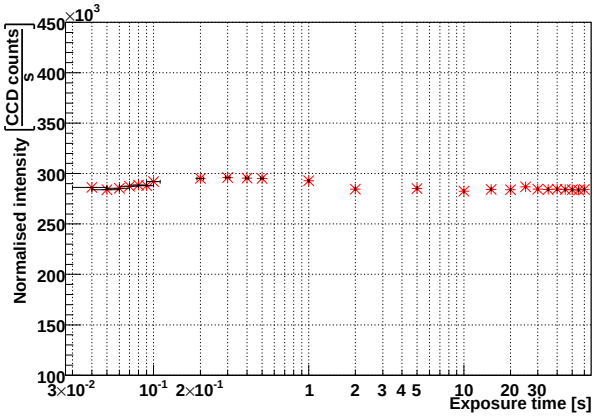

Fig. 3.49: Figure of the error corrected exposure time-normalized light intensity versus exposure time: The calculated time-normalized intensity is constant.

error could be reproduced with an accuracy of 0.0013 s[14].

[14]The accuracy is calculated according to the standard deviation.

3.5.1.2 Influence of the Camera Aperture

Another important parameter is the aperture of the CCD camera. Normally, one would assume a quadratic connection between light intensity and aperture radius, respectively to the aperture radius. But, since it is unclear whether the aperture diameter, which is numerically stated by the manufacturer, is correct this was analyzed as follows. The light emission of the laser is adjusted to the maximal aperture and the exposure time is set to its minimum. The focus is set on the spectralon. Then the signal and background image are recorded for each camera aperture. Figure 3.50 shows the acquired data which were analyzed. The integration limits were set for the largest aperture. The data analysis shows that

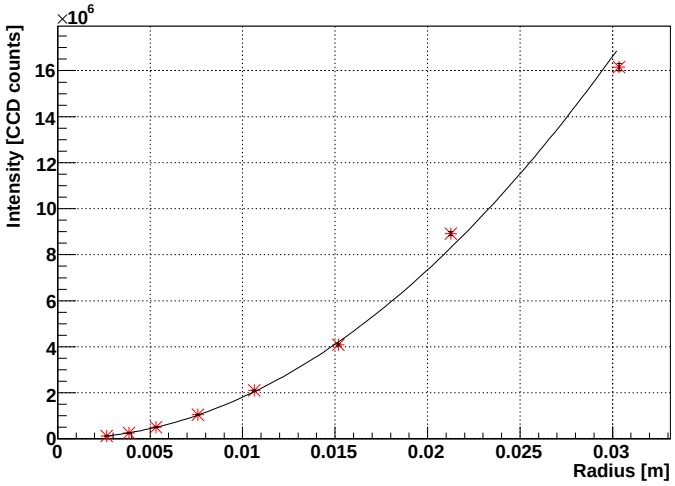

Fig. 3.50: Plot of the light intensity versus aperture radius: The data are fit with a two-degree polynomial.

the indication of the aperture by the f-number k by the manufacturer is not very precise. Knowing the f-number k and the focal length f, one can calculate the aperture diameter D.

$$k = \frac{f}{D} \tag{3.20}$$

The area-normalized light intensity varies although it should be constant, as shown in figure 3.51.

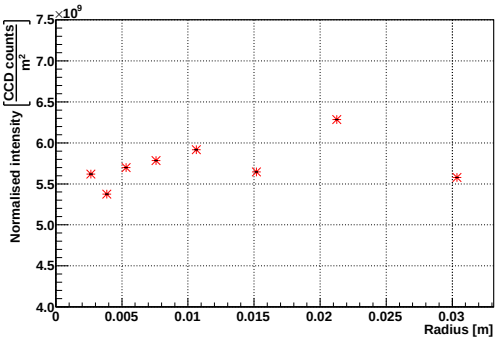

Fig. 3.51: Figure of the area-normalized intensity versus aperture area: Against the expectation of a constant area-normalized intensity this varies slightly.

A potential reason could be an inaccurate manufacturing of the aperture diameters. Therefore, the measurement was repeated using an external diaphragm with a defined diameter[15], as illustrated in figure 3.52.

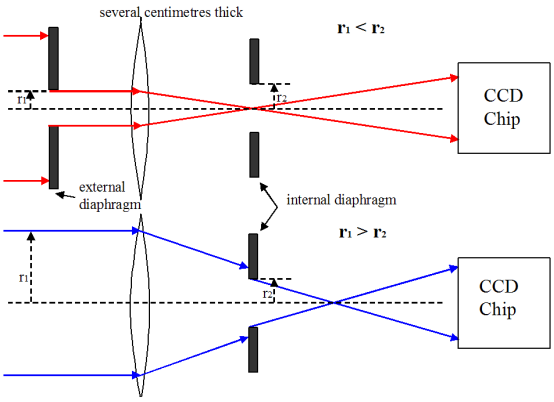

Fig. 3.52: Schematic optical path with (blue) and without (red) an external diaphragm. If the internal diaphragm is smaller than indicated, outer beams are cut off. If an external diaphragm of a defined diameter is used limiting the light beam diameter, the correct area-normalized intensity can be calculated

[15]Several external diaphragms with differing diameters were tested. The diaphragm of 40 mm diameters turned out to be sufficiently small in order to limit the entering light while the aperture of the CCD camera was maximal. One has to note that the external diaphragm should not cut off any marginal rays of the light spot.

This assures, aside from the fact that the exact aperture diameter is known, that one knows the position of the effective entrance window which has an important influence on the measurement conditions of sections 3.5.1.3 and 3.5.1.4. Figure 3.53 confirms that the detected intensity is in fact, limited by the external diaphragm as long as the aperture of he CCD camera is sufficiently larger than the external one.

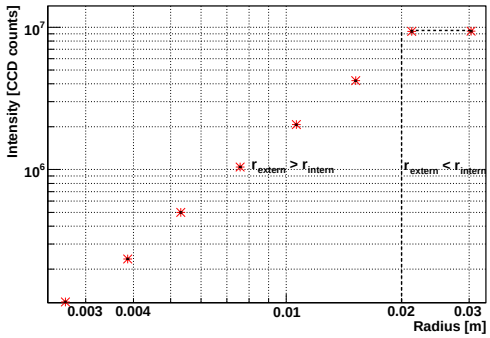

Fig. 3.53: Logarithmic figure of the intensity versus aperture area using an external diaphragm. As long as the radius of the external diaphragm is smaller than that of the internal diaphragm, the detected intensity is constant. If the radius of the internal diaphragm is minimized so that it is smaller than the radius of the external diaphragm, the detected light intensity changes according to the square of the area of the internal diaphragm.

3.5.1.3 Influence of the Focusing

The third camera parameter whose influence on the detected light intensity has to be determined is focusing. Usually, focusing should not have any influence on the integrated intensity of the light spot, unless the distance between the CCD camera and the light spot is large enough. When the light spot is out of focus, the local intensity decreases but the area of the image increases accordingly so that the area-normalized intensity is constant. To verify this, data were recorded for different focusing. The light emission of the laser was adjusted for the correct focusing at maximal aperture and minimal exposure time. Thus, the CCD camera does not saturate for any of the images. The integration limits are adjusted according to the maximal detected light beam. Figure 3.54 presents the

results of this measurement. In contrast to the above mentioned expectation, the

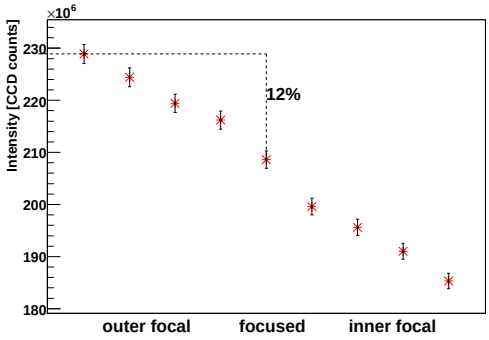

Fig. 3.54: Illustration of intensity versus focusing: The maximal divergence of the detected light intensity for both outer focal and inner focal focusing from the measured light intensity of the correct focused adjustment is 12 %.

detected intensity depends on focusing. The detected intensity is higher for outer focal focusing and lower for inner focal focusing[16] compared with the actual intensity measured for correct focusing. The maximal divergence for minimal inner focusing and maximal outer focusing is 12 %. A reason for this could be that the internal diaphragm of the camera is integrated in a position where the light is not parallel. Thus, depending on the focus more or less light is cut by the diaphragm, see figure 3.55. Consequently, the effective aperture is a function of the focusing.

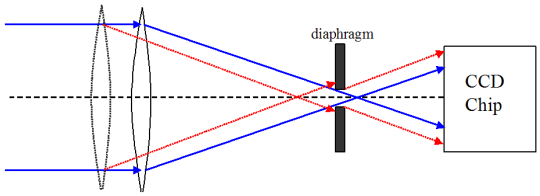

Fig. 3.55: Schematic optical path for two different focusings: If the focssing is correct (blue), no light beams ar cut off by the diaphragm. For an other focusings (red) the detcted light intensity is reduced because the diaphragm limits the light beam diameter.

[16]For Outer focal focusing the CCD camera is focused on a distance which is larger than the distance between the CCD camera and the light spot. In turn, for inner focal focusing the CCD camera is focused on a distance which is shorter than the distance between the CCD camera and the light spot.

But, for the measurement of the focused reflectivity it is necessary to change the focusing as explained in section 3.5.2. Nevertheless, the detected area-intensity has to be constant. Hence, the measurement was repeated using the external diaphragm. The external diaphragm cuts away the outer light beams in the CCD camera which are affected by the internal diaphragm. The internal diaphragm thus has no longer any effect, as long as it is opened sufficiently. As can be seen in figure 3.56 the integrated intensity of the image is now independent of the focus[17].

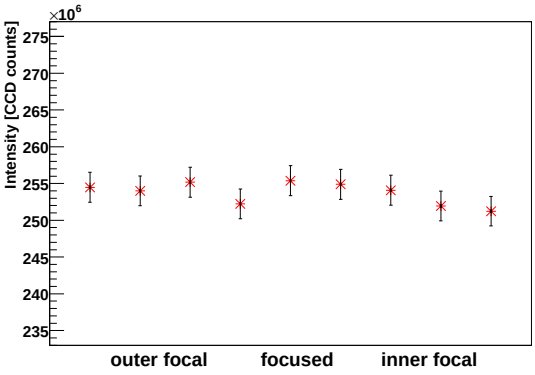

Fig. 3.56: Figure of the re-measured dependency of the intensity versus focusing using an external diaphragm: The divergence could be reduced to less than 1 %.

3.5.1.4 Influence of Distance

The measurement of the distance law is the following. An image of a light spot, imaged on the spectralon was taken at several different distances using the CCD camera. The distance is measured from the aperture of the objective. Since an inverse dependency of the illuminance to the square of the distance is expected, the light emission is adjusted to the minimal distance in order to avoid an image saturation during the measurement. In order to compare the acquired data the integration limits were adjusted for the maximal distance. In figure 3.57 the data are shown.

[17]The divergence amounts only to 0.7 % which is probably caused by light emission fluctuations

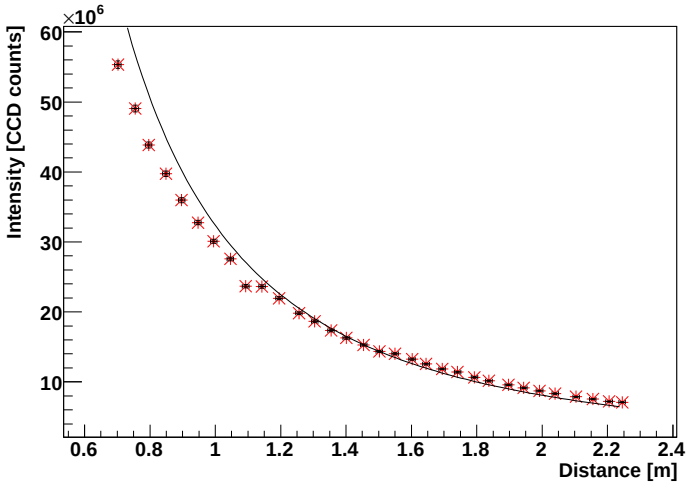

Fig. 3.57: Plot of the intensity versus distance: For short distances the data differ from the expected distance law (black).

One can see that the data do not exactly follow the expected curve. Especially for shorter distances the divergence is more significant as figure 3.58 confirms. The reason for this is probably the same as explained in the sections 3.5.1.2

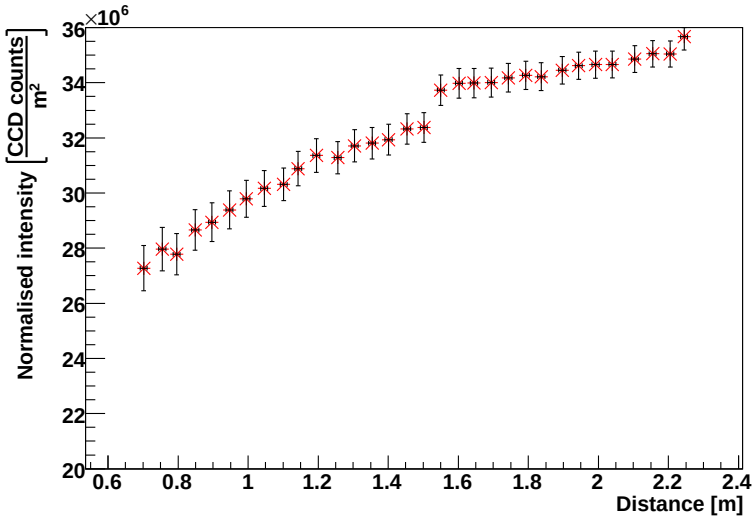

Fig. 3.58: Graphic of the distance-normalized intensity versus distance: The distance-normalized intensity is not constant.

and 3.5.1.3. This would mean that the expected distance-dependency is not given for the aperture for it does not limit the amount of entering light. However,

since the external diaphragm has to be used for the measurement of the focused reflectivity, in order to assure the correctness of the above-mentioned physics the measurement was redone applying the external diaphragm. As a result, the data fit exactly with the expected quadratic curve shape as one can conclude from figures 3.59(a) and 3.59(b).

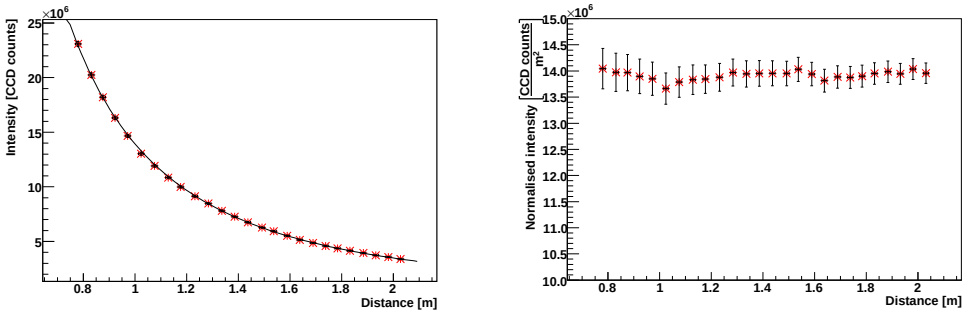

(a) Detected intensity versus distance: The data follow the distance law.

(b) Distance-normalized intensity versus distance: The variation of the distance-normalized intensity is negligible.

Fig. 3.59: Presentation of the re-measured distance-dependency of the detected light intensity using an external diaphragm

3.5.1.5 Influence of the Angle

For the second measurement method of the focused reflectivity, see section 3.5.2.2, the diffuse reflecting material called spectralon is used. Hence, one has to verify its reflecting characteristic which is expected to show Lambertian behavior. Also, the absolute value of its spectral reflectivity has to be known. Therefore, the intensity, reflected by the spectralon, is measured as a function of the angle of the reflected beam. The measuring setup is shown in figure 3.60. The light source is positioned at a large distance r in front of the spectralon with an angle of incidence of 0°. Behind this light source the CCD camera is set. In this way, the light's depth of impression, which is $6 - 7$ mm can be neglected with regards to the distance r. The spectralon is turned such that the angle between the camera and the reflecting surface can be changed from $-90°$ to 90°. The position of the light spot on the spectralon is adjusted such that it lies on the axis of rotation of the spectralon. Thus, the distance r of the light spot and the CCD camera is the

same for the complete measurement. A flat grinded LED is used as a light source. The purpose of polishing is to ensure a point source of radiation. Also, just as for the analysis of the exposure time, see section 3.5.1.1, a constant current source is used so that the light emission does not fluctuate significantly. The light beam of

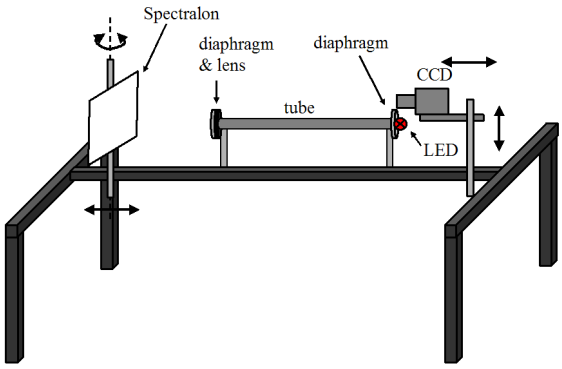

Fig. 3.60: Schematic measurement setup of the determination of the angular dependency of the intensity reflected by spectralon

the LED is limited by a diaphragm of 1 mm diameter. This is positioned in the focal length of a lens emitting a parallel beam of light. An additional diaphragm is used for eliminating lens aberrations and diffraction. Considering this, it has to be assured that the lens and the second diaphragm are out of the field of view of the CCD camera.The reflectivity of the spectralon is measured for three different wavelengths.For an ideal diffuse reflecting surface, the radiation characteristic of the light intensity $I(\phi)$ of a point light source is described by the law of Lambert. This means that the intensity follows a cosine.

$$I(\phi) = I(0°) \cdot \cos(\phi) \tag{3.21}$$

As one can see in figure 3.61, the emission is not characterized by Lambert. When the angle of observation equals the angle of incidence which is 0°, one measures aside from the diffuse reflectance a specular component which amounts to about 10 % of the detected light intensity. The assumption of a specular component is confirmed by an additional measurement which was done with the spectrophotometer CM-2500d, shown in figure 3.62. Furthermore, as mentioned above, the light permeates several millimeters into the spectralon. Hence, light is not only reflected by the spectralon's surface but also from its inside. Consequently, the

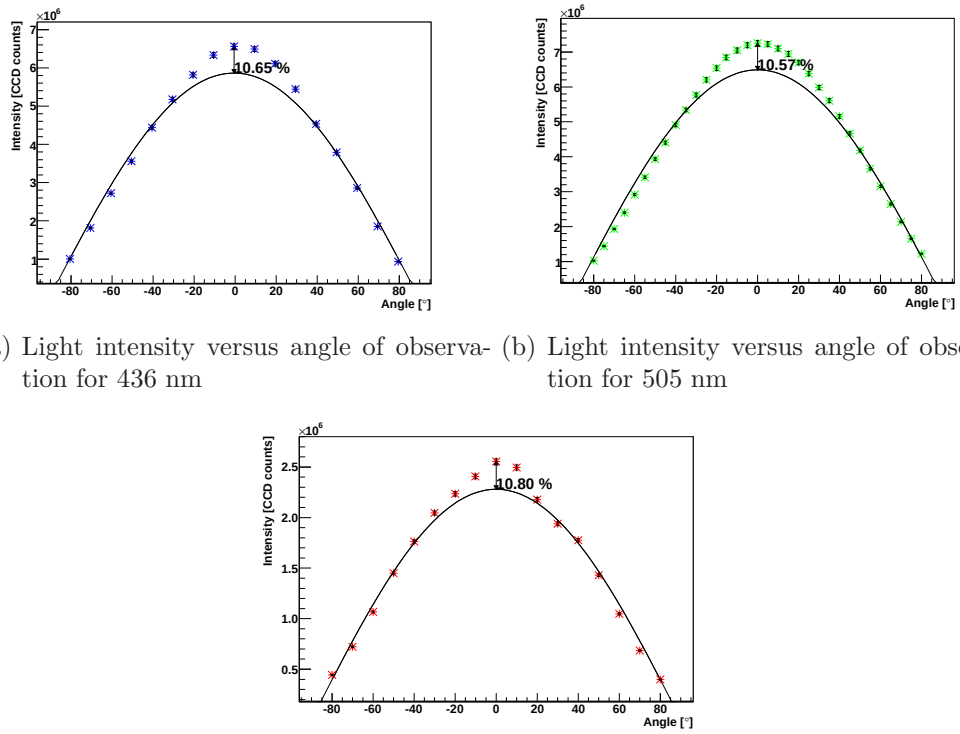

(a) Light intensity versus angle of observation for 436 nm

(b) Light intensity versus angle of observation for 505 nm

(c) Light intensity versus angle of observation for 625 nm

Fig. 3.61: Light intensity versus angle of observation for three different wavelengths. For angles between $-30°$ and $30°$ the directional characteristic differs from Lambertian behavior (black fit). When the incidence angle equals the angle of observation, the divergence is about 10 %.

light has to transit differing ways from the inside of the spectralon, depending on the direction of diffuse reflection. For long distances the light is absorbed by the spectralon. Hence, the solid angle Ω into which light is reflected is smaller than it is for Lambertian behavior, as shown in figure 3.63. This divergence of the expected Lambertian behavior has to be taken into account for the reflectivity calculation of the spectralon. As figure 3.64 shows, the measured direction characteristic fits to a fourth-degree polynomial. Generally, the total light intensity $I_{\text{Spectralon}}(\lambda)$ reflected by the spectralon can be calculated as the integral of the detected light intensity $I(\lambda, \phi)$ as a function of the angle ϕ of radiation over the

[18]For Lambertian behavior the solid angle Ω equals π.

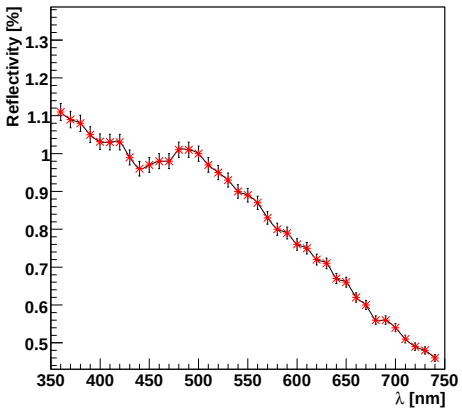

Fig. 3.62: Specular reflectivity of the spectralon versus wavelength measured with spectrophotometer CM-2500d: Although the spectralon should only reflect diffusely, a small specular component could be measured.

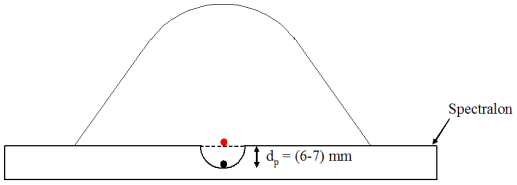

Fig. 3.63: A sketch of the directional characteristic of spectralon (red) compared to ideal Lambertian behavior (black): Due to absorption in the inside of the spectralon, the directional characteristic differs from Lambert. Hence, the solid angle Ω is supposed to be smaller than π[18].

area A_{Sphere} of a half sphere, as shown in figure 3.65.

$$I_{\text{Spectralon}}(\lambda) = \int_{\theta=0}^{2\pi} \int_{\phi=0}^{\frac{\pi}{2}} I(\lambda, \phi) \cdot r^2 \cdot \sin(\phi) \mathrm{d}\phi \mathrm{d}\theta$$

The light intensity $I(\lambda, \phi)$ can be described as a fourth-degree polynomial, having a_0, a_2 and a_4, as constant factors[19]. Also, the aperture area $A_{\text{CCD}}$of the CCD caemera has to be taken into acount.

$$I(\lambda, \phi) = \frac{I_0(\lambda) \cdot (a_0 + a_2\phi^2 + a_4\phi^4)}{A_{\text{CCD}}}$$

[19]The constant factors were evaluated by fitting the data with ROOT.

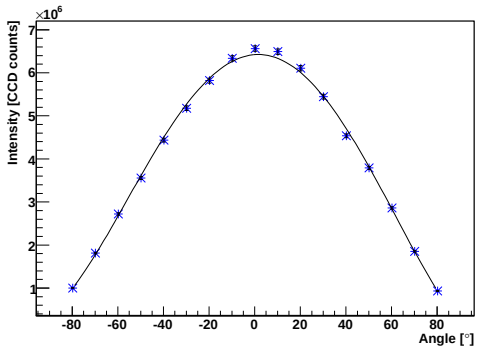

Fig. 3.64: Fourth-degree polynomial fit of the measured direction characteristic: Assuming an axially symmetric shape the factors of the odd terms are set to 0. So, the fit's formula is $I(\lambda\phi) = I_0(\lambda) = a_0 + a_4 \cdot \phi^2 + a_4 \cdot \phi^4$.

So $I_{\text{Spectralon}}(\lambda)$ can be calculaletd as:

$$I_{\text{Spectralon}}(\lambda) = \frac{2\pi \cdot Rr^2}{A_{\text{CCD}}} \int_{\phi=0}^{\frac{\pi}{2}} \left(a_0 + a_2\phi^2 + a_4\phi^4\right) \cdot \sin(\phi)\mathrm{d}\phi \ . \tag{3.22}$$

The intensity emitted by the light source is measured directly with the CCD

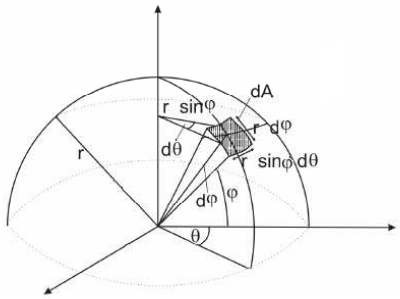

Fig. 3.65: A sketch of the area of a half sphere spanned by its radius of curvature r and the angles θ and ϕ.

camera. In order to do so, the emission of the LED was adjusted for minimal exposure time. For the measurement of the light reflected from the spectralon for an angle of observation of 0° the exposure time was increased to have a measurable signal. By consequence, the demanded reflectivity $R_{\text{Spectralon}}(\lambda)$ of the surface is

calculated by the ratio of the entire reflected intensity of the surface $I_{\text{Spectralon}}(\lambda)$ to the directly detected intensity $I_{\text{Lightsource}}(\lambda)$ taking the different exposure times $t_{\text{Lightsource}}$ and $t_{\text{Spectralon}}$ into account.

$$R_{\text{Spectralon}}(\lambda) = \frac{I_{\text{Spectralon}}(\lambda) \cdot t_{\text{Lightsource}}}{I_{\text{Lightsource}}(\lambda) \cdot \cos(\phi) \cdot t_{\text{Spectralon}}} \tag{3.23}$$

,with the parameters as shown in table 3.3

Parameter	436 nm	505 nm	625 nm
a_0	$7.80 \cdot 10^5$	$7.30 \cdot 10^5$	$7.54 \cdot 10^5$
a_2	$-4.97 \cdot 10^5$	$-4.80 \cdot 10^5$	$-5.22 \cdot 10^5$
a_4	$8.25 \cdot 10^4$	$7.85 \cdot 10^4$	$9,57 \cdot 10^4$
$I_{\text{Spectralon}}(0°)$	$7.97 \cdot 10^5$	$7.37 \cdot 10^5$	$7.46 \cdot 10^5$
$I_{\text{Lightsource}}$	$1.54 \cdot 10^7$	$1.39 \cdot 10^7$	$1.39 \cdot 10^7$

Tab. 3.3: Listing of the obtained fit parameter and data for the reflectivity calculation of the Spectralon

$$\begin{aligned} t_{\text{Spectralon}} &= 30 \text{ s} \\ t_{\text{Lightsource}} &= 0.04 \text{ s} \\ R &= 2.19 \text{ m} \\ A_{\text{CCD}} &= 1.3 \text{ mm}^2 \text{ .} \end{aligned}$$

Also, the correct solid angle Ω in which the spectralon reflects has to be calculated using the obtained fit parameters. Since $I_0(\lambda)$ is a constant, it does not have to be taken into account for the evaluation of the integral, see equation 3.22. This is just a function of the angles θ and ϕ that equal the solid angle as Ω generally can be computed with

$$\Omega = \int_{\theta=0}^{2\pi} \int_{\phi=0}^{\frac{\pi}{2}} \sin(\phi) \mathrm{d}\phi \mathrm{d}\theta \text{ .}$$

So, by calculating the accordant integral one obtains the solid angle:

$$\Omega = \int_{\theta=0}^{2\pi} \int_{\phi=0}^{\frac{\pi}{2}} (a_0 + a_2\phi^2 + a_4\phi^4) \cdot \sin(\phi) \mathrm{d}\phi \mathrm{d}\theta \text{ .}$$

This can be simplified to

$$\Omega = 2\pi \left(a_0 \int_{\phi=0}^{\frac{\pi}{2}} \sin \mathrm{d}\phi + a_2 \int_{\phi=0}^{\frac{\pi}{2}} \phi^2 \cdot \sin \mathrm{d}\phi + \int_{\phi=0}^{\frac{\pi}{2}} \phi^4 \cdot \sin \mathrm{d}\phi \right) .$$

The resulting formula is

$$\Omega = 2\pi \cdot (a_0 + 1.15 \cdot a_2 + 1.89 \cdot a_4) .$$

But, the parameters obtained from the fit still include $I_0(\lambda)$. By dividing the parameters by $I_0(\lambda)$ this can be eliminated.

$$\Omega = 2\pi \cdot \frac{(a_0 + 1.15 \cdot a_2 + 1.89 \cdot a_4)}{I_0(\lambda)} . \tag{3.24}$$

As expected, the solid angle evaluated for three wavelengths is smaller than the solid angle of the spherical half space (π). Moreover, for shorter wavelengths the solid angle is higher than for longer wavelengths. This is because the depth of permeation d_p is wavelength-dependent. This means that shorter wavelengths have a shorter permeation depth:

$$d_\mathrm{p} \sim \lambda . \tag{3.25}$$

The results are presented in table 3.4 .

λ [nm]	$\Omega_{\mathrm{Spectralon}}$ [sr]
436	2.84
505	2.76
625	2.70

Tab. 3.4: Presentation of the calculated solid angle for different wavelengths

The calculated reflectivity for the corresponding wavelengths, as well as the reflectivity measured with the spectrophotometer CM-2500d are presented in table 3.5. Compared to the diffuse reflectivity measured with the spectrophotometer, see

	Reflectivity [%]	
λ [nm]	measured with CCD camera	measured with spectrophotometer CM-2500d
436	85.2	94.0
505	84.6	94.5
625	86.4	95.0

Tab. 3.5: Presentation of the reflectivity of the spectralon for different wavelengths

also figure 3.66, the reflectivity, calculated with the data of the CCD camera measurement are significantly smaller. Assuming that the solid angle for mea-

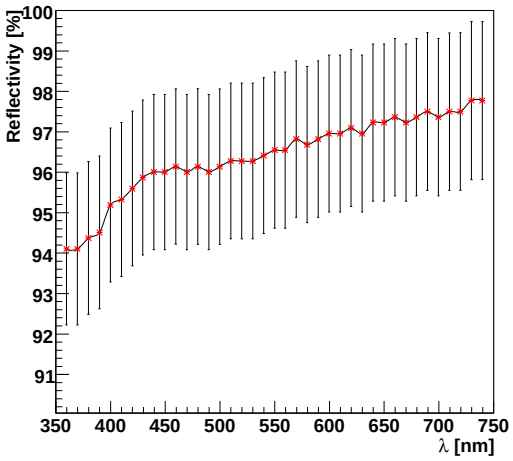

Fig. 3.66: Diffuse reflectivity of the spectralon versus wavelength measured with spectrophotometer CM-2500d

surement with the spectrophotometer is defined as that of a spherical half space, the evaluated reflectivity values should be higher of about a constant factor. So, the ratio of the different results for the reflectivity R_{CCD} and $R_{\mathrm{CM-2500d}}$ should be equal to that of the different results of the solid angle, Ω_{CCD} and $\Omega_{\mathrm{CM-2500d}}$.

$$\frac{R_{\mathrm{CCD}}}{R_{\mathrm{CM-2500d}}} \stackrel{!}{=} \frac{\Omega_{\mathrm{CCD}}}{\Omega_{\mathrm{CM-2500d}}} \tag{3.26}$$

The results of the factors are shown in table 3.6 Since the assumption of a constant

	Ratio	
λ [nm]	Reflectivity ratio r_R	Solid angle ratio r_Ω
436	1.1	1.1
505	1.1	1.1
625	1.1	1.1

Tab. 3.6: Listing of two ratios concerning the Spectralon's diffuse reflectivity and its solid angle, evaluated with two different methods

factor has been proved, the reflectivity results obtained with the spectrophotometer can be considered wrong, for they are obviously calculated with the specification of a wrong solid angle. The divergence of Lambertian behavior could be reproduced. Also, the specular component was repeatedly measured. For the reflectivity calculation of the spectralon the error propagation was not made.

3.5.2 Results and Measurement Setup for the Focused Reflectivity

As shown in figure 3.67, the setup for this measurement is the following. The

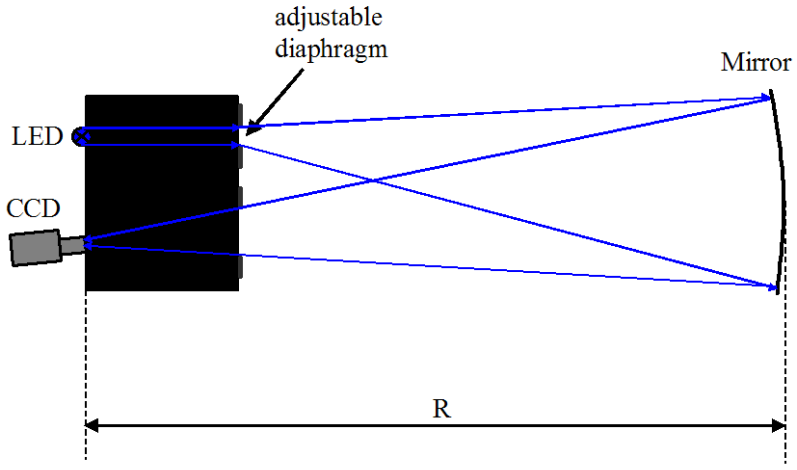

Fig. 3.67: First setup of the measurement of the focused reflectivity

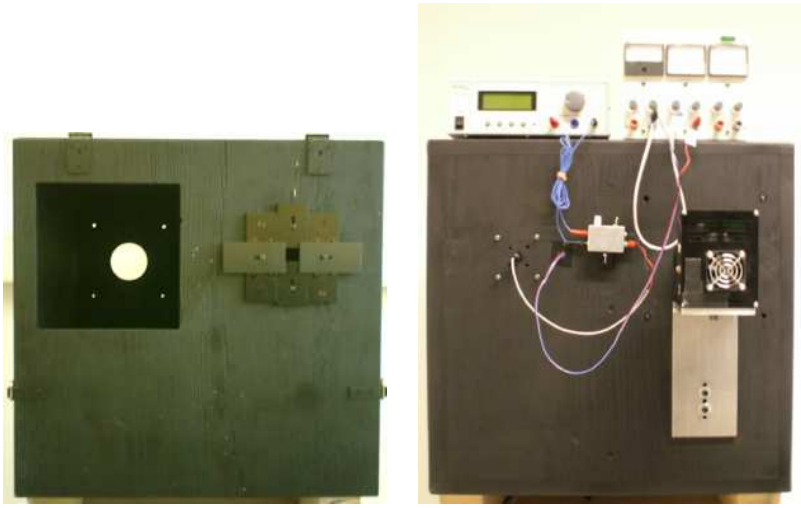

(a) Front side of the black box (b) Back side of the black box

Fig. 3.68: Setup of the black box

black box is presented in figure 3.68. In the distance which equals to the mirror's radius of curvature R a light source is positioned. The light source is the same LED as used for the measurement of the directional characteristic described in section 3.5.1.5. Moreover, the light emission is monitored by using the same procedure as described in section 3.5.1. Additionally, the light source is mounted on the back side of a black box which consists of two separated chambers. There is an adjustable squared blind at the right front side. In this way the diameter of the light beam is limited. In this way, unwanted reflections within the optical path and hence measurement errors can be reduced. On the left front side the reflected light enters the left chamber of the black box. On its back side either the CCD camera or the spectralon can be mounted at the same height as the light source. The measurement is performed at night for which a low background is desired. This assures that the contribution of stray light in the measured light intensity is insignificant. The distance between the mirror and the light source has to be about 34 m. Therefore, the measurement has been performed in a shaded corridor. The measurement itself is performed according to the following procedure. First the position for which the distance of the light source to the mirror equals that of the minimal spot size of the reflected light is searched. Then, the diaphragm of the black box is adjusted so that the mirror is completely illuminated. Afterwards, the position of the spot of the reflected light is set so that it

enters approximately the centre of the external aperture attached to the CCD camera. This is realized by adjusting the mirror position. After this, the correct focusing is done. Finally, the light emission is regulated for minimal exposure time so that the dynamic range is optimized. Several signal and background pictures are recorded, whereas the LED is not switched off but covered by an opaque box. The reason for this is that switching off of the light source could cause some light emission fluctuations. Repeated recording allows the determination of the variance of the data. Thereafter, the CCD Camera is put in front of the black box and the spectralon is attached to its back side as shown in figure 3.69. Thereby, the distance of the CCD camera to the spectralon should be maximized. The height of the CCD camera is not changed compared to the previous position . Also, the horizontal angle of observation of the CCD camera should be optimized without interfering with the optical path. The exposure time is adjusted to a value for

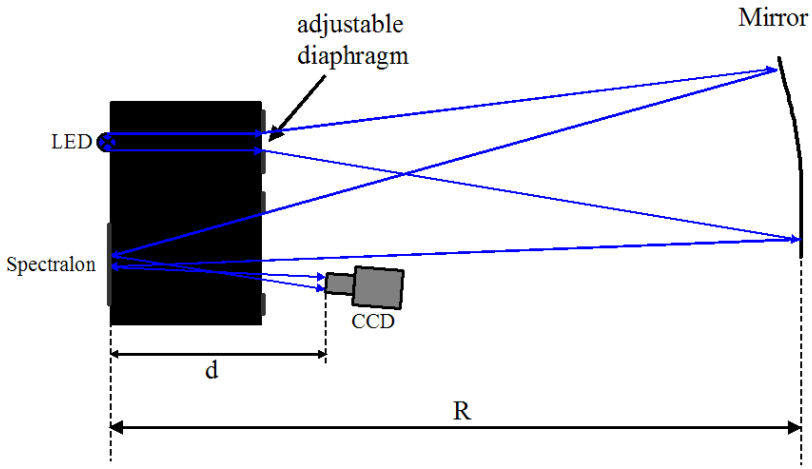

Fig. 3.69: Second setup of the measurement of the focused reflectivity

which the signal is sufficiently high compared to the background. Again, several frames are recorded in order to improve accuracy. After this, the position of the CCD camera is changed again. A rack is placed in the plane of the mirror where the CCD camera can be mounted as shown in figure 3.70 In this way the light field can be determined at nine different positions of the mirror which are the same as shown in figure 3.33 in section 3.4. Furthermore, the homogeneity of the illumination of the mirror, which has to be implicitly assured, can be verified.

Fig. 3.70: Illustration of the rack used for the measurement of the light field

Figure 3.71 shows the schematic setup. For this measurement focusing is rele-

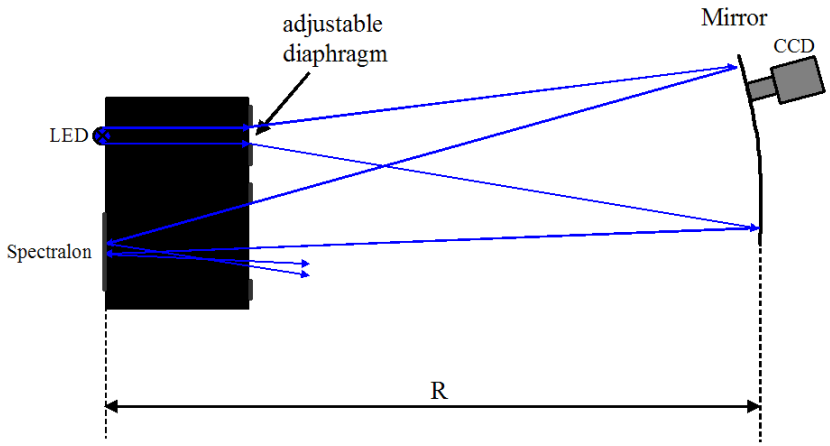

Fig. 3.71: Third setup of the measurement of the focused reflectivity

vant. The reason for this is that depending on the focusing the diameter of the detected light field varies. Once the CCD camera is focused on a distance close to the exit pupil of the light source, the diameter of the light beam is very small. Consequently, detected intensity depends significantly on the sensitivity of each pixel. Aside from this effect, it could be that a photon is not detected because it hits an area between two neighboring pixels which is not light sensitive. So, the focusing must be adjusted, fulfilling two conditions. The diameter of the light field has to be sufficiently large and the detected signal still has to differ enough from the background at minimal exposure time. After this adjustment, the data

are recorded for the nine measurement positions.

3.5.2.1 Focused Reflectivity Direct Method

The calculation of the focused reflectivity is the following. The entire light intensity $I_{\text{Lightfield}}(\lambda)$ that illuminates the mirror is calculated as follows. Having verified that the illumination is constant over the entire mirror surface the intensity $I_{\text{Lightfield}}(\lambda)$ results from the intensity detected by the CCD camera $I_{\text{CCD}_3}(\lambda)$ normalized on the surface of the aperture A_{CCD} and scaled on the mirror surface A_{Mirror}:

$$I_{\text{Lightfield}}(\lambda) = \frac{I_{\text{CCD}_3}(\lambda) \cdot A_{\text{Mirror}}}{A_{\text{CCD}}} \ . \tag{3.27}$$

The expectation is that the intensity $I_{\text{Focus}}(\lambda)$ which is detected at the minimal position has a Gaussian shape, as shown in figure 3.72. Therefore, the detected intensity does not depend on the surface of the aperture unless this is sufficiently large with regards to the size of the reflected image. s This means that the inten-

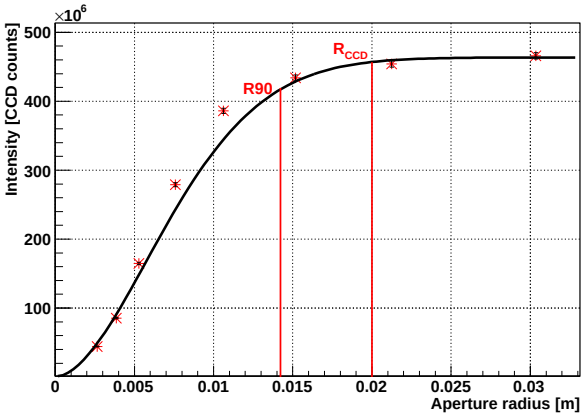

Fig. 3.72: Plot of the intensity versus aperture surface for the radiance of the reflected image, assuming a two dimensional Gaussian shape: The R90 and the radius of the CCD camera aperture R_{CCD} are indicated.

sity of the reflected image $I_{\text{Focus}}(\lambda)$ corresponds to the detected intensity $I_{\text{CCD}_1}(\lambda)$. This is computed as an integral of the intensity of the reflected image's surface which is shown in figure 3.73. The average an the the RMS[20] of the acquired data

[20]For the error calculation the RMS is assumed to be the error of the measured light intensity.

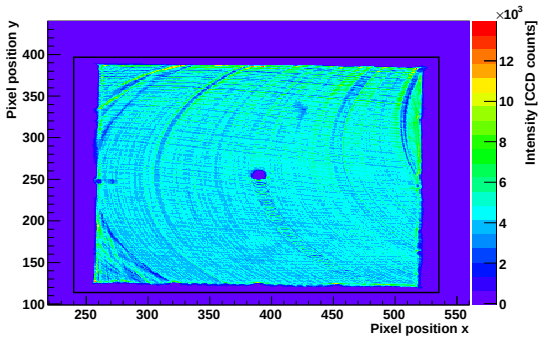

Fig. 3.73: The reflected image the focus recorded for the focused reflectivity calculatio: The integration limits (black) are included. One can see from which position of the mirror light gets reflected into the focus. Also, the milling grooves are identifiable

is calculated. The detected intensity, emitted by the LED is evaluated with the same procedure. The detected intensity is shown in figure 3.74. All acquired data

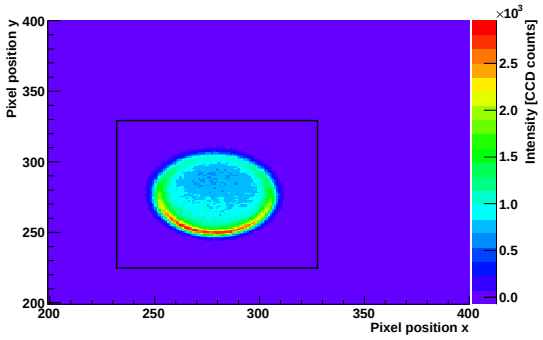

Fig. 3.74: The detected light intensity emitted by the LED of the focused reflectivity measurement. The integration limits (black) are shown.

were analyzed with the basic procedure as already described. The analysis shows that the light intensity at the mirror surface is, as required, position-independent. With these data, the reflectivity $R_{\mathrm{Focus}}(\lambda)$ can be calculated by the ratio of the intensity, $I_{\mathrm{Focus}}(\lambda)$ detected in the focus, and the calculated intensity $I_{\mathrm{Lightfield}}(\lambda)$ which illuminates the mirror.

$$R_{\mathrm{Focus}}(\lambda) = \frac{I_{\mathrm{Focus}}(\lambda)}{I_{\mathrm{Lightfield}}(\lambda)}$$

$$R_{\mathrm{Focus}}(\lambda) = \frac{I_{\mathrm{CCD1}}(\lambda)}{I_{\mathrm{CCD3}}(\lambda)} \cdot \frac{A_{\mathrm{CCD}}}{A_{\mathrm{Mirror}}} \tag{3.28}$$

The error of this calculation is determined by Gaussian error propagation:

$$\Delta R_{\mathrm{Focus}}(\lambda) = \left(\begin{array}{l} \left(\frac{\partial R_{\mathrm{Focus}}(\lambda)}{\partial I_{\mathrm{CCD_1}}(\lambda)} \cdot |\Delta I_{\mathrm{CCD_1}}(\lambda)| \right)^2 + \left(\frac{\partial R_{\mathrm{Focus}}(\lambda)}{\partial A_{\mathrm{CCD}}} \cdot |\Delta A_{\mathrm{CCD}}| \right)^2 \\ + \left(\frac{\partial R_{\mathrm{Focus}}(\lambda)}{\partial I_{\mathrm{CCD_3}}(\lambda)} \cdot |\Delta I_{\mathrm{CCD_3}}(\lambda)| \right)^2 + \left(\frac{\partial R_{\mathrm{Focus}}(\lambda)}{\partial A_{\mathrm{Mirror}}} \cdot |\Delta A_{\mathrm{Mirror}}| \right)^2 \end{array} \right)^{\frac{1}{2}} \tag{3.29}$$

3.5.2.2 Focused reflectivity Indirect Method

As already explained in section 3.5.1.5, the entire light intensity $I_{\mathrm{Spectralon}}(\lambda)$ can be calculated as the Integration of the detected light intensity $I_{\mathrm{CCD_2}}(\lambda)$ over the area of a half sphere. For this calculation concerning the solid angle $\Omega_{\mathrm{Spectralon}}$ and the reflectivity of the spectralon $R_{\mathrm{Spectralon}}$ are used. Additionally, the distance d and the aperture area A_{CCD} of the CCD camera are taken into account.

$$I_{\mathrm{Spectralon}}(\lambda) = \frac{d^2 \cdot I_{\mathrm{CCD_2}} \cdot \Omega_{\mathrm{Spectralon}}}{A_{\mathrm{CCD}} \cdot R_{\mathrm{Spectralon}}} \tag{3.30}$$

The angle of observation ϕ is estimated to be insignificant since it equals a few degrees so that the measured light intensity $I_{\mathrm{CCD_2}}(\lambda)$ is assumed to equal the light intensity reflected with an angle of radiation of 0°. The detected intensity $I_{\mathrm{CCD2}(\lambda)}$ is calculated by integration of the recorded intensity of the reflected image seen on the spectralon. Figure 3.75 shows the recorded image. Thus, the focused reflectivity $R_{\mathrm{Focus}}(\lambda)$ equals the ratio of the integral of the light intensity $I_{\mathrm{Spectralon}}(\lambda)$, detected in the focused position of the reflected figure which is imaged on the spectralon, and the integral of the light intensity $I_{\mathrm{Lightfield}}(\lambda)$ detected at the mirror as described in section 3.5.2.1. Since these intensities are measured with different exposure times $t_{\mathrm{CCD_2}}$ and $t_{\mathrm{CCD_3}}$, this has to be taken into account by normalization.

$$R_{\mathrm{Focus}}(\lambda) = \frac{I_{\mathrm{Spectralon}}(\lambda)}{I_{\mathrm{Lightfield}}(\lambda)}$$

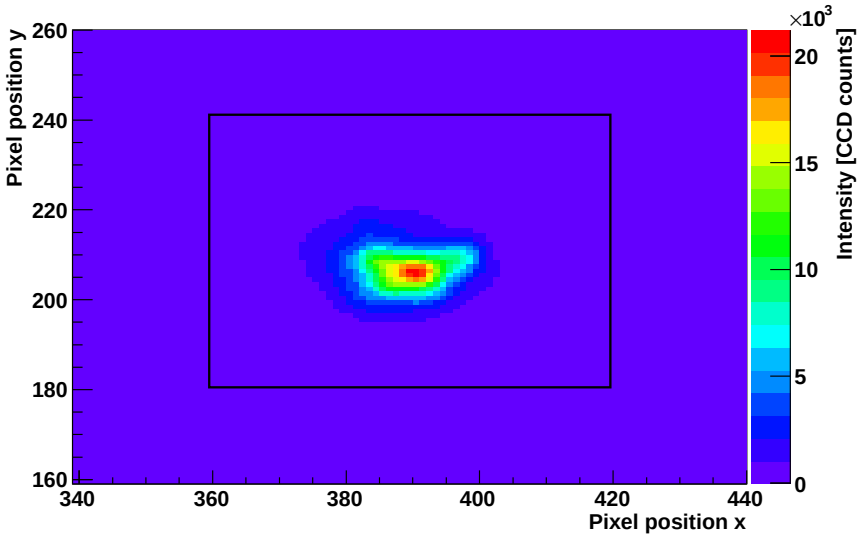

Fig. 3.75: The image reflected by the Spectralon recorded for the focused reflectivity calculation: The integration limits (black) are also shown.

$$R_{\mathrm{Focus}}(\lambda) = \frac{I_{\mathrm{CCD_2}}(\lambda) \cdot t_{\mathrm{CCD_3}}(\lambda) \cdot \Omega_{\mathrm{Spectralon}} \cdot d^2}{I_{\mathrm{CCD_3}}(\lambda) \cdot A_{\mathrm{Mirror}} \cdot t_{\mathrm{CCD_2}} \cdot R_{\mathrm{Spectralon}}(\lambda)} \tag{3.31}$$

The error of this calculation is determined by Gaussian error propagation:

$$\Delta R_{\mathrm{Focus}}(\lambda) = \left(\begin{array}{l} \left(\frac{\partial R_{\mathrm{Focus}}(\lambda)}{\partial I_{\mathrm{CCD_2}}(\lambda)} \cdot |\Delta I_{\mathrm{CCD_2}}(\lambda)| \right)^2 + \left(\frac{\partial R_{\mathrm{Focus}}(\lambda)}{\partial r} \cdot |\Delta d| \right)^2 \\ + \left(\frac{\partial R_{\mathrm{Focus}}(\lambda)}{\partial t_{\mathrm{CCD_3}}} \cdot |\Delta t_{\mathrm{CCD_3}}| \right)^2 + \left(\frac{\partial R_{\mathrm{Focus}}(\lambda)}{\partial I_{\mathrm{CCD_3}}(\lambda)} \cdot |\Delta I_{\mathrm{CCD3}}(\lambda)| \right)^2 \\ + \left(\frac{\partial R_{\mathrm{Focus}}(\lambda)}{\partial A_{\mathrm{Mirror}}} \cdot |\Delta A_{\mathrm{Mirror}}| \right)^2 + \left(\frac{\partial R_{\mathrm{Focus}}(\lambda)}{\partial t_{\mathrm{CCD_2}}} \cdot |\Delta t_{\mathrm{CCD_2}}| \right)^2 \\ + \left(\frac{\partial R_{\mathrm{Focus}}(\lambda)}{\partial R_{\mathrm{Spectralon}}(\lambda)} \cdot |\Delta R_{\mathrm{Spectralon}}(\lambda)| \right)^2 \end{array} \right)^{\frac{1}{2}} \tag{3.32}$$

In table 3.7 the data used for the calculations explained above are shown.

Parameter	436 nm	505 nm	625 nm
$I_{\mathrm{CCD_1}}$ [CCD counts]	$1.72 \cdot 10^9$	$8.34 \cdot 10^8$	$1.32 \cdot 10^9$
$I_{\mathrm{CCD_2}}$ [CCD counts][21]	$3.36 \cdot 10^6$	$7.37 \cdot 10^5$	$2.54 \cdot 10^6$
$I_{\mathrm{CCD_3}}$ [CCD counts]	$3.06 \cdot 10^6$	$1.53 \cdot 10^6$	$2.53 \cdot 10^6$
$\Delta I_{\mathrm{CCD_1}}$ [CCD counts]	$4.21 \cdot 10^6$	$5.15 \cdot 10^5$	$1.01 \cdot 10^6$
$\Delta I_{\mathrm{CCD_2}}$ [CCD counts]	$4.21 \cdot 10^5$	$5.05 \cdot 10^4$	$2.00 \cdot 10^4$
$\Delta I_{\mathrm{CCD_3}}$ [CCD counts]	$3.64 \cdot 10^3$	$1.79 \cdot 10^3$	$1.79 \cdot 10^3$

Tab. 3.7: Presentation of the data used for the calculation of the focused reflectivity

$$
\begin{aligned}
t_{\mathrm{CCD_1}} &= 0.04 \text{ s} \\
t_{\mathrm{CCD_2}} &= 1.00 \text{ s} \\
t_{\mathrm{CCD_3}} &= 0.04 \text{ s} \\
d &= 2.10 \text{ m} \\
A_{\mathrm{CCD}} &= 1.26 \text{ mm}^2 \\
A_{\mathrm{CCD}} &= 1.26 \cdot 10^{-3} \text{ m}^2 \\
\Delta t &= 0.01 \text{ s} \\
\Delta d &= 0.003 \text{ m} \\
\Delta A_{\mathrm{Mirror}} &= 1 \cdot 10^{-3} \text{ m}^2 \\
\Delta A_{\mathrm{Mirror}} &= 1.26 \cdot 10^{-4} \text{ m}^2
\end{aligned}
$$

3.5.2.3 Comparison of the Focused Reflectivity and the Surface Reflectivity

Table 3.8 shows the results of the focused reflectivity measurements and the average spectral reflectivity measured at the mirror surface. As the comparison of both measurement methods of the focused reflectivity shows, the evaluated reflectivities show a very good conformance[22]. As one can see, the focused reflectivity

[21] $\phi \approx 0°$.

[22] Before using the external diaphragm the results of these measurement methods showed a difference of a factor of about 1.5.

	focused reflectivity [%]			surface reflectivity [%]
λ[nm]	direct	indirect	expected	minolta
436	59.9± 0.30	61.9± 0.07	≈ 77.42	88.42±0.1
505	69.5±0.35	70.9±0.08	≈ 77.52	88.52±0.1
625	66.4±0.3	69.6±0.08	≈ 76.48	86.48±0.1

Tab. 3.8: Comparison of the different reflectivity measurements[23]

is much less than the reflectivity measured on the mirror surface. This is because of diffraction through what a certain amount of light is scattered arbitrarily into the focal plane. However, the expected focused reflectivity is still higher than the measured one. One reason could be that the reflectivity loss is underestimated. Both results of the focused reflectivity, measured with two slightly different methods show a good agreement. They vary about 5 % maximum. The reason could be that the angle of observation of the CCD camera equals the angle of incident of the reflected image on the spectralon. If so, as described in section 3.5.1.5, one detects aditionally the specular component of the reflection. Also, as shown in section 3.5.1.1, the exposure time is defective which especially falsifies the indirect measurement method of the focused reflectivity.
The fact that the reflectivity is less for shorter wavelengths than for longer ones is noticeable because of the coating. It is actually expected to be maximal for shorter wavelength as measured on the mirror surface, see section 3.3. One possible reason for this effect could be that the diffraction for light of shorter wavelengths is broader than for longer wavelengths for the diffraction angle α is inversely proportional to the wavelength λ of the light.

$$\alpha \sim \lambda \tag{3.33}$$

Thus, it is possible, that light of shorter wavelength is diffracted out of the aperture of the CCD camera, whereas the diffraction of light of longer wavelength is probably rather insignificant. More important is the fact that the specification of a minimal reflectivity of 85 % from 320 nm to 600 nm is actually not fulfilled.

[23]The expected focused reflectivity is calculated by subtracting the estimated loss of 11 % due to scattering and diffraction from the average surface reflectivity. Since this is a rough estimation, no error is indicated. For the surface reflectivity the average of the 12 measured specular reflectivity data has been computed for each wavelength.

3.5.2.4 Scattered Light Measurement

As the measurement of the diffraction shows, a certain part of the reflected light is scattered and hence is located somewhere in the focal plain, but not in the focused spot. Although it is not possible to scan the entire focal plane for potential position of scattered light it is at least important to prove that there are other positions than the focused spot where light is reflected and light is located. Thus, in order to get qualitative information on whether the divergence between the surface reflectivity and the focused one of the mirror is primarily caused by scattered light the CCD camera is put into some arbitrary positions where the light intensity is measured. The exposure time has to be adjusted in such a manner that a sufficiently high signal can be detected. The measurement results show that a marginal shifting of the CCD camera out of the position where the reflected image is situated already changes the intensity distribution of the figure. This is also illustrated in figure 3.76(b). Additionally, a calculation of the scattered light

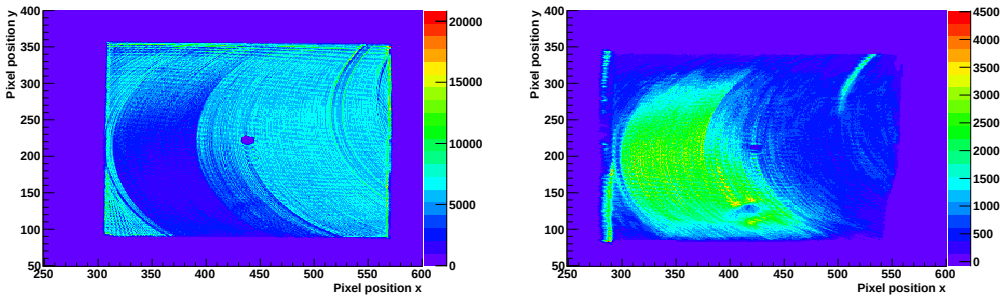

(a) Detected intensity distribution in the position of the focused reflected spot

(b) Detected intensity distribution of the focused reflected spot in a slightly shifted position of the CCD camera

Fig. 3.76: Comparison of the detected light intensity for two positions in the focal plane. In figure 3.76(a) a significant fraction of the mirror surface dos not seem to reflect light to the focused spot. By contrast, this fraction reflects light to a position nearby a focused spot, see figure 3.76.

by summing up the light intensities of a few positions for which the scattered light is measured shows that the total diffuse reflectivity of all of the measured positions is almost 4 %. This explains the potential differences between the focused reflectivity and the one measured at the mirror surface, see section 3.5.3.

3.5.3 Xenon Lamp Measurement

In order to compare the spectral reflectivity with the focused one within a large wavelength range, the focused reflectivity has to be measured for several wavelengths. Since this measurement of the focused reflectivity is very time-consuming a xenon lamp is used, as one can see in figure 3.77. This emits a continuous light

Fig. 3.77: Xenon lamp unit with the power supply[26]

spectrum down to almost 200 nm[26]. Hence this offers the possibility of analyzing the focused reflectivity at a large wavelength range. The detection is done with the Andor Shamrock SR-303i spectrograph which is presented in figure 3.78. This

Fig. 3.78: The spectrograph Andor Shamrock SR-303i[27]

is provided with a CCD camera, as well as with three blazed grids. The principle of a blazed grid is that it is used for splitting up the detected light into its spectral components by diffraction. Hereby, the maximal light intensity is located in a higher diffraction order than the zeroth one one[24]. Having different efficiencies these grids are optimized for the analysis of different wavelength ranges. The

[24]The zeroth diffraction order is simply a specular reflection.

operation mode is the following one.The light enters the spectrograph through a slit with an adjustable width. Afterwards, the light enters the selected grid which splits up the light into its single components. After this wavelength separation the single components are detected with the CCD Camera, whereas each wavelength is detected by different areas of the CCD. The CCD camera contains 1024 columns and 256 rows. These rows are summed up for each column afterwards in order to compute the total of the detected intensity of each spectral component. An accessory software is used for the adjustment of the parameter of the spectrograph such as the slit width, the exposure time or the wavelength range which has to be analyzed. By using the wavelength selector the selected grid is turned. In doing so, different spectral subranges can be analyzed. Due to the turning of the grid the angle of reflection changes. According to the divergence between the actual angle of reflection and the optimized one, the detected light intensity differs. Figure 3.79 shows this. The two advantages of using a xenon

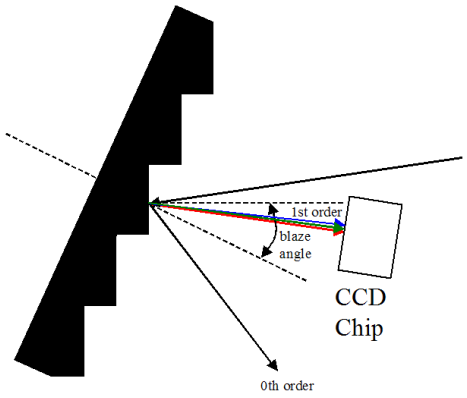

Fig. 3.79: Functionality of the blaze grid

lamp for the evaluation of the focused reflectivity is that it is time-saving, because one can measure the spectral shape of the focused reflectivity at the same time. Furthermore, the evaluation can be done for short wavelength where the Cherenkov radiation is stronger. Before measuring the focused reflectivity with the xenon lamp, its emission stability was checked by measuring this over a time period of 30 minutes. The xenon lamp turned out to be stable. In principal, the setup for the measurement of the focused reflectivity with the xenon lamp is similar to that described in section 3.5.2 except for the fact that the light detector

and the light source are different. Also, the black box is not used for this setup but instead a diaphragm is put in front of the xenon lamp in order to limit the diameter of the emitted light. Also, a respective band pass filter is used for detection in order to suppress higher harmonic oscillations. With the detector two spectra are recorded. One is the spectrum emitted by the xenon lamp. This is measured in the plane of the mirror. The other one is the reflected one which is detected at the position of the minimum size of the reflected spot. For both measurements the spectra are corrected by the measured respective background spectrum. Since one cannot analyze the complete wavelength range from 200 nm up to 800 nm the analysis is done once for three subranges. These are selected in such a way that there is a certain overlap, As the grid has to be turned for observing different ranges the detected intensities differ between the measurements for the above mentioned reasons. This becomes noticeable by offsets between the different subranges. Thus, the subranges have to be corrected for these offsets. The measurement of the focused reflectivity that is performed with the xenon lamp is only a relative one. The reason is that both the diameter of the emitted light and the diameter of the minimal size of the reflected figure are much larger than the maximal width of the spectrograph. Consequently, the total amount of the reflected light cannot be detected. Therefore, this measurement is only used in order to determine the spectral focused reflectivity $R_{\mathrm{Focus}}(\lambda)$ in arbitrary units by dividing the reflected intensity spectrum $I_{\mathrm{reflected}}(\lambda)$ through the emitted one $I_{\mathrm{emitted}}(\lambda)$.

$$R_{\mathrm{Focus}}(\lambda) = \frac{I_{\mathrm{reflected}}(\lambda)}{I_{\mathrm{emitted}}(\lambda)} \tag{3.34}$$

Since the focused reflectivity was measured for several wavelengths separately, these can be used for rescaling the obtained spectrum. The resulting data equals the spectral shape of the focused reflectivity, as shown in figure 3.80. Whether the evaluated spectral reflectivity is consistent with the actual reflectivity spectrum is not yet clear. The reason is that the evaluated reflectivity spectrum was not reproducible. So, it is possible that the spectrum is inaccurate due to potential systematic measurement errors. Therefore, further measurements have to be done in order to obtain a more reliable spectrum which shows more conformance concerning the trend of the overlapping subranges. This spectrum e.g. has

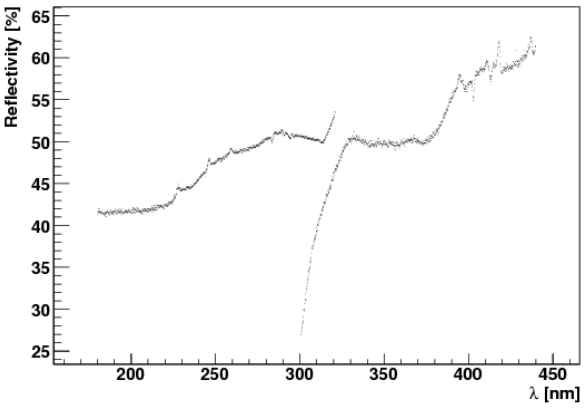

Fig. 3.80: The rescaled focused reflectivity spectrum, showing two subranges at UV: The gap at 300 nm is because the data of the two subranges differ. This is an undesired effect which still has to be analyzed.

a contradictory intersection between both subranges. It is still unclear whether this effect is caused by emission fluctuations or by the spectrograph, respectively by its blazed grid. Having a reliable spectrum, one could analyze the potential differences between the surface reflectivity and the focused one. Because of the existence of diffraction and scattered light, see sections 3.4 and 3.5.2.4, one would expect certain differences concerning the spectral shape of the reflectivity of the mirror surface and the focused reflectivity.

3.5.3.1 Flatfield Box

The single optical parts of the CCD camera usually cause a certain image error. Possible errors are vignettng, dust on filters or even the CCD itself, as shown in figure 3.81.

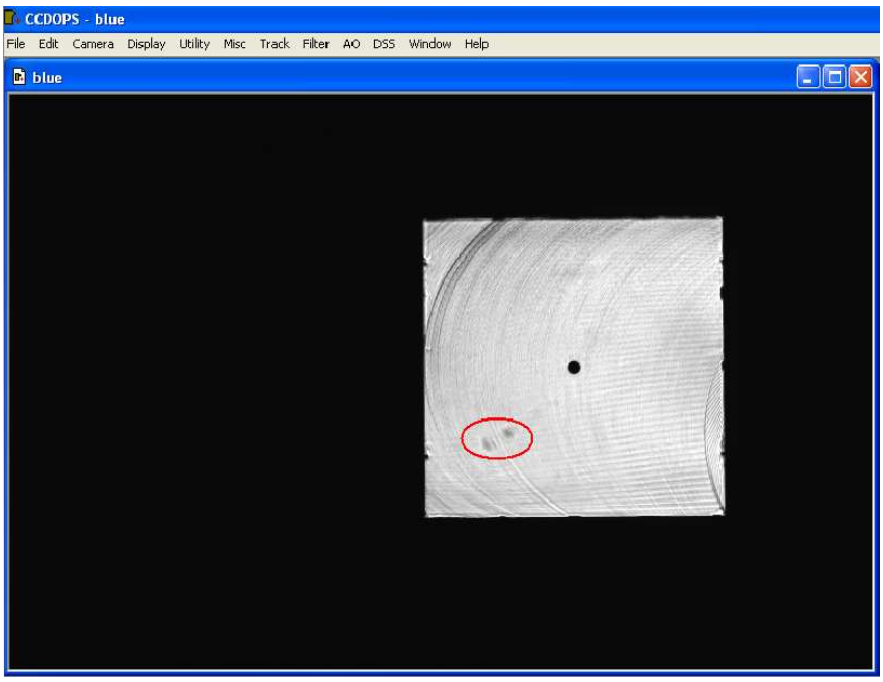

Fig. 3.81: Recorded image including some imaging errors

Therefore, a so-called flat field is generated with which these errors can be corrected. Moreover, the differing sensitivity of each pixel can be equalized. In doing so, a light box is used. Figure 3.82 shows the light box that has to fulfill several criteria in order to assure a uniform illuminance of the CCD.

- Its material has to be reflective.
- It should feature an opaque glass for diffusing purposes.
- The illumination of the light box has to be indirect and uniform
- It has to be larger than the aperture diameter

The flat field box consists of three parts. The back and front side are made of spectralon between which an opaque disc is placed. Since it is unclear whether the quality of the taken data images becomes significantly better by flat field correction this shall be verified in the following. Also, the procedure of how to create a proper flat field will be described. First, the light box is attached to the camera objective. Second, the front side as well as the opaque disc of the flat field box are removed. Third, focusing is adjusted. Neither the camera position nor focusing are changed until the flat field, the background image and signal image

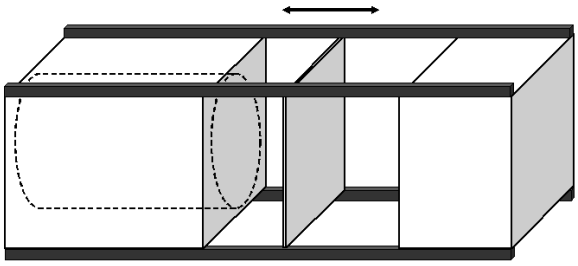

Fig. 3.82: Flatfield Box

are taken. After having taken the background and the signal image, the front side and the opaque disc of the light box are attached. A halogen lamp is used for the uniform and indirect illumination of the light box. The exposure time is set so that the saturation of the pixels is about 50 % up to 75 %. Several background flat fields and signal flat fields are made for increasing the measurement precision. These data are analyzed with a macro that averages the data and subtracts the average of the dark flat field from the signal flat field. Finally, the resulting flat field is rescaled according to the maximal value which has been detected. In a final step the background corrected signal image, see 3, is divided by the flat field. In doing so, the afore-mentioned potential imaging errors should be removed. As one can see in figure 3.83, the upper right and left corner of the taken flatfield possess vignetting[22]. This means that the actual data images include the same error. By correcting the data image for the flat field these errors can be reduced. As one can see in figure 3.84, the dust on the image could not be removed. But the quantity of the detected light intensity increases. If one compares the two computed integrals of the recorded intensity, one will notice that the difference between both is 6 %. Since this difference does not lie within the emission fluctuations it is not negligible. But, as it is a constant error, each recorded image that contains it must not be taken into account for reflectivity calculation.

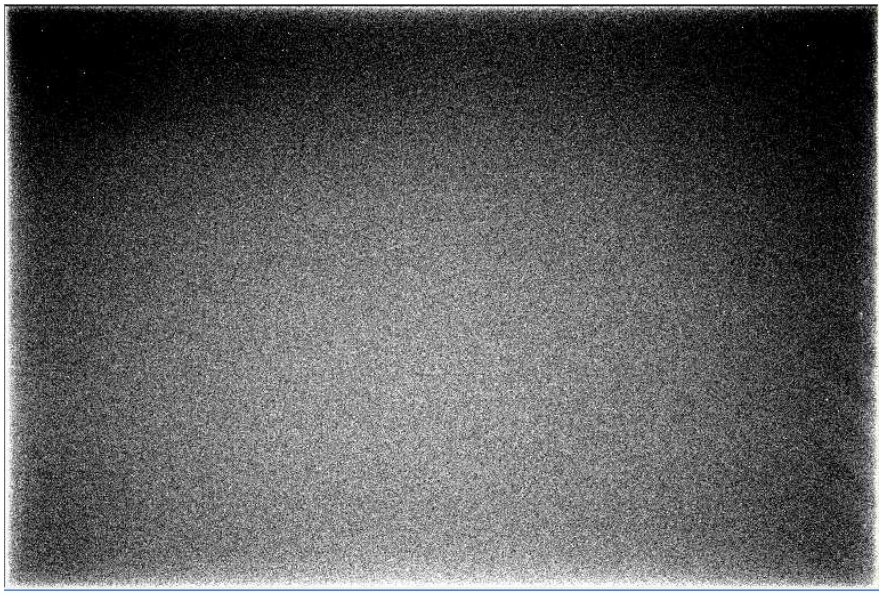

Fig. 3.83: Presentation of the measured flatfield

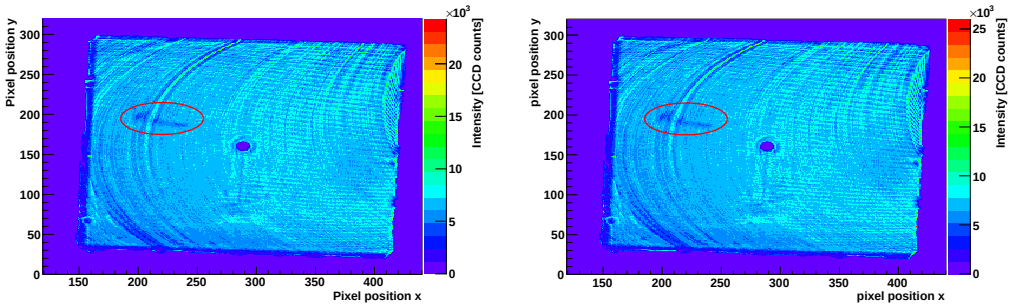

(a) Background corrected image including errors

(b) Background and flat field corrected image

Fig. 3.84: Comparison of an image without and with flat field correction. The flat field correction has an influence on the detected light intensity

4 Silicon Photomultiplier for Future Cherenkov Telescopes

In the eighties and nineties of the last century a novel solid state detector being able to detect single photons, has been developed in Russia (for a review see[28]). These detectors, based on matrices of small avalanche photodiodes (called correctly cell and not, as frequently in the literature, cells) working above breakdown in the so-called Geigermode were pursued by many groups and have nowadays reached a level of maturity to be considered for many applications. The developments are nevertheless still ongoing and many improvements are possible. There are many different names used for many design variants, one of the most popular name being Silicon Photomultiplier[1]. There are several reasons why Silicon Photomultipliers[29] are a potential replacement for conventional photomultipliers in IACTs. Firstly, SiPMs have the capability not only to detect single photons and produce a well defined output signal but also are able to resolve many photons hitting the SiPM at different places. This is the consequence of the high internal amplification and the standardized output signal for the triggering photoelectron. Depending on the construction and cell size of the matrix elements the gain can be easily above 10^6 and comparable to the gain of PMTs. As we will see later, this high gain is actually also one of the main problems. Secondly, SiPMs can have a very high quantum efficiency (QE) for their active area, similar to Silicon PIN photodiodes. The quantum efficiency defines the percentage of photons hitting the photodiode, which produce an electron-hole pair in the sensitive volume. The QE is a wavelenght-dependent parameter[30]. In practice the QE of the sensitive area cannot be reached in current designs because the useful signal depends mainly on the probability to trigger an avalanche multiplication process

[1]The name of silicon photomultiplier is a bit misleading because the photo-multiplication, as we will see later, is actually one of the biggest problems in these devices.

and in turn a detectable signal. The probability to trigger an avalanche depends on the overvoltage above breakdown as well as the status of the hit cell (sensitive or in a recovery state after a breakdown). Therefore it is much more suitable to replace the QE by a practical quantity, called photon detection efficiency (PDE), which quotes the probability that a photon is converted into a measurable signal. While PMTs should be in principle also be specified by their PDE instead by the photocathode QE the use of PDE is much more appropriate for SiPMs because this quantity is strongly depending on the overvoltage. In PMTs one can separate the PDE (an stabilize it by a fixed voltage between photocathode and first dynode) from the gain but this is not possible in SiPMs, see later discussion. SiPMs are insensitive to magnetic fields unlike PMTs and, as well, very compact and robust. In addition, they can be operated with a lower voltage than PMTs. Furthermore, they can be exposed to ambient light when under bias voltage without being damaged. These characteristics offer a big advantage compared to PMTs and quantify them of having a significant potential to improve in the Cherenkov telescope sensitively. This can decrease the detection threshold of the IACT.

4.1 Concept and Functionality of the Silicon Photomultiplier

A photodiode[31] is a p-n-junction implemented in silicon close to the surface where external photons have a sufficient probability of entering the junction. Depending on the geometry and wavelength an incident photon can create an electron-hole pair in the depletion layer. Both the electron and the hole travel in the opposite direction along the electric field in the p-n-junction. Thus, a ‘photo current‘ flows. This current is proportional to the number of incident photons converted in the junction. If a reverse bias voltage is applied to the photodiode, the electric field in the p-n-junction, as well as the depleted volume, increase. Thus, the response of the photodiode to the incident photons becomes faster for pulsed light and furthermore, the QE efficiency can be slightly increased due to the increased depleted volume. Nevertheless, PIN photodiodes do not allow single photon detection because the diodes have gain 1 and , in addition, a large serial noise. Even the best photodiodes have a minimal detection threshold of

$\approx 200 - 300$ photoelectrons in the case of a reduced bandwidth for noise minimization. From a certain reverse bias voltage onwards the so-called avalanche effect starts. This means that the primary electron from the electron-hole pair is sufficiently accelerated by the electrical field such that impact ionization can occur, i.e. an extra e-h pair can be created. Depending on the field strength and extension of the high field zone the process can repeat and further charge carriers are generated and in turn amplification occurs. Holes are normally not sufficiently accelerated to produce also electron hole pairs due to their larger virtual mass and lower mobility. Actually, in linear mode avalanche photodiodes (which operate at a few Volts below the breakdown voltage) the hole multiplication is a highly unwanted process because this can produce large signal fluctuations. In principle, also photons are produced by the avalanche process. These photons can travel a certain distance and, when absorbed on the p-side of the p-n structure create again an e-h pair from which the electron can again be accelerated to sufficiently high energy creating again an e-h pair. The photon production process has a very low probability and plays no role in low gain linear mode avalanche photodiodes. If the bias voltage is raised above the breakdown voltage, the number of secondary e-h pairs increases dramatically and a sizeable fraction of holes is also able to create new e-h pairs and multiplication is initiated on both sides of the p-n structure. This multiplication is, in contrast to avalanche multiplication below the breakdown voltage, continuous because it is fuelled by free charge carriers from both sides of the p-n junction as long as external charge can be supplied. It is basically a secondary avalanche multiplication process. If one did not provide any external current limitations, the ongoing multiplication would increase the current and the device would be destroyed. If, on the other hand, one were to connect the small capacitance of the p-n junction and allow only a small current by a high ohmic resistor, then the multiplication process would go on only until the stored energy is used up and the overvoltage on the capacitance would drop to the breakdown voltage (may be even a bit below) i.e., the avalanche is quenched. If as normal all the free charge carriers were transported away and no new ones generated, the small capacitance would be charged up again until a new free charge carrier, for example generated by an absorbed photon or a thermally generated e-h pair, would start the process again. The principle of a small p-n volume with a small capacitance charged above breakdown and the avalanche multiplication started

by a free charge carrier in the 'dielectric' between the capacitor plates and the limitation of the external recharging current by a resistor acting as a quencher of the discharge very much resembles the gaseous detector designed by Geiger in the 1920s for the observation of radioactive particles. Therefore, these photon detectors are generically called Geigermode avalanche photodiodes (G-APD). In the past, single cell G-APDs used mostly external resistors while nowadays the quenching/recharging resistors are integrated into the device. The gain G, i.e., the amplification by the avalanche process is given by the available charge stored in the p-n junction capacitance set by the difference of the overvoltage and the breakdown voltage.

$$G \approx C \cdot (U_{\mathrm{Bias}} - U_{\mathrm{Breakdown}})$$

$$G = C \cdot U_{\mathrm{Ecxess}} \tag{4.1}$$

$$G^2 = 2.4 \cdot 10^6$$

,with C being the capacitance of the p-n structure. Another important reason why the SiPM functions at all is the fact that a very small volume p-n diode can be biased for a short time well above breakdown voltage and remain for some time in such a 'superbiased state'. Any free charge carrier, weather an electron from the absorption of an external photon or a thermally generated e-h pair or from a 'field emission' carrier by the high field of the p-n junction can start the avalanche process and, due to the well-defined stored energy in the capacitance, generates a well-defined electrical signal. A condition for this operation is that the time for biasing the small diode above breakdown is much shorter than the mean time at which an e-h hole pair is generated thermally. It is obvious that this superbiased state cannot be sustained for a very long time (except by strong cooling). Also, low quality semiconductor materials are unsuitable because of the high rate of dark currents. In large volume p-n devices a large number of thermal e-h pairs are always generated and thus it is impossible to charge up the diode capacitance to sufficiently high values. A SiPM consists of an array of small volume avalanche photodiodes, the so-called cells, operated in the Geiger-mode. Each cell of predefined capacitance is linked via an integrated resistor to

[2]The gain is specified by Hamamatsu for the MPPC 100MU device, type number S106362-11-100U, sample number 54.

a common bus. On this common bus 'quantized' signals from each avalanche process show up respectively and add up if more than one cell fires at the same time. Each cell is separated from its neighbors by some insensitive material, i.e. by some silicon material inefficient for photon detection and that also stop transverse extensions of the avalanche process. The basic design of one SiPM cell is shown in figure 4.1. In order to stop/quench the avalanche the multiplication of two

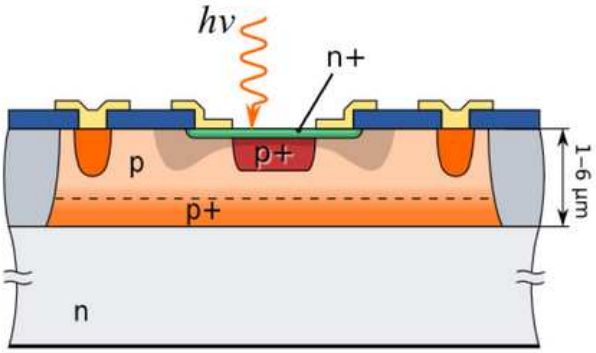

Fig. 4.1: Schematic Design of a Silicon Photomultiplier pixel [32]

different methods, passive and active quenching, can be used. The use of a large resistor, called passive quenching stops the Geiger-mode because the charging current is too small to sustain the avalanche process after the stored 'overcharge' has been consumed. On the contrary, with active quenching the avalanche is stopped because for a short time the connection to the external power supply is cut and no external current can flow for a few nsec. Then, after the time needed to clear the junction from all free charge carriers, the capacitance of the cell is recharged much more rapidly than by a resistor. Active quenching needs a complex electronics circuit for each cell and is thus unpractical for a multicell SiPM. The SiPM that has been analyzed in the study described below is passively quenched. Once an avalanche is started an extra photon cannot trigger an additional avalanche in the same cell at the same time, i.e., the cell is a digital device with only two states. On the one hand, the large number of cells in a SiPM (typically 100 to a few 1000 /mm^2) allows one to detect a large number of photons provided they are randomly distributed over the area and mostly only one photon hits on average a single cell. On the other hand, a too large a number of photons will result in saturation and SiPMs therefore, have a more limited dynamic range

than for example PMTs. A peculiarity linked to the avalanche process and that poses severe limitations to the PDE is the above mentioned production of a few photons. This process seems to be not fully understood. Experimentally one has determined[29] a rate of

$$\approx 3-4 \text{ photons (between} 1-1.4 \text{ eV energy)/gain of} 10^5 \ . \tag{4.2}$$

Photons of this energy can travel out of cells and there is a high probability they will be absorbed in neighboring cells thus giving rise to unwanted local avalanches in these cells and faking a larger photon flux. This process is called optical crosstalk. If the gain is high, such as in the studied Hamamatsu MPPCs, the increase of the bias voltage will on the one hand increase the PDE but on the other increase the unwanted photons to a level that nearly all cells will be fired by secondary processes. Using the key features of SiPMs listed above one clearly sees the dilemma of the construction of SiPMs with a high PDE:

- Cells should be not too small otherwise the necessary fraction of dead material between the cell becomes too large and the mean QE will be too low and in turn the achievable PDE very limited.
- On the other hand, the depleted cell volume should be not too large otherwise the cell would nearly always be in a low state because of a high number of thermally generated e-h pairs giving rise to permanently small avalanches.
- To produce a large active area cell with a low volume means that the depleted layer has to be as thin as possible. Typical SiPMs have a depleted layer of a few microns of thickness.
- A thin depletion layer for low noise means automatically a high cell capacitance.
- In order to achieve a high PDE, one needs a significant overvolatge.
- For a significant overvoltage and a high cell capacitance, one will automatically get a high gain and in turn a high optical cross talk.

Therefore, often for large cell sizes one only has the choice of lowering the overvoltage and keeping the optical crosstalk in acceptable ranges and paying it by

accepting a low PDE well below the limit of the QE. There were ideas to use trenches between the individual cell. These trenches would again, at least partially, suppress optical crosstalk but one would pay by lowering the limit in average QW due to the large increase in inefficient area. To get a clearer and more quantitative picture of the optical crosstalk a study on a promising SiPM, the Hamamatsu MPPC 100U was carried out.

4.2 Crosstalk Analysis

In order to verify the correlation between crosstalk, bias voltage and PDE some measurements were performed. The setup for the crosstalk measurement is shown in figure 4.2. This instrument was developed by Kolja Prothmann[33], a diploma student, whom I assisted during the construction. The measurements and analyses were done together. The setup for the crosstalk measurement is shown in figure 4.2. The Setup, shown in figure 4.2(a), is built up on a positioning table. The entire setup can be covered with a coping so that no external light falsifies the measurement. The optical equipment consists of a microscope using an objective lens, the M Plan Apo NIR 100X, focused to infinity and coupled to a tube lens with a beam splitter that allows both to view an object and project it onto a CCD camera, the MT-L, also from Mitutoyo. Using this microscope, the SiPM is imaged onto the CCD camera ICX205AL from SONY. The 'infinity corrected' object lens, being free of spherical aberration, creates parallel rays for each image point in the focal plane. Correspondingly, it focuses the parallel light, emitted by a laser and coupled through the other viewing port into one point in the focal plane. This means that the diameter of the focused light spot is sufficiently small in order to analyze at least a 25 μm diameter cell at 5 spatial points because of the maximum spot size of 5 μm diameter. The positioning accuracy of this setup is about 1 μm. Positioning is done by moving the preamplifier board onto which the SiPM is soldered. The setup is screwed onto an adapter, which is attached to an XYZ-stage MTS25XYZ by Thorlabs, thus the SiPM can be moved inside the field of view of the microscope in all three dimensions. The focusing of the laser spot can be checked with the camera. Once the surface is on the focal plane, the laser is coupled in with a beam splitter, which is positioned in the

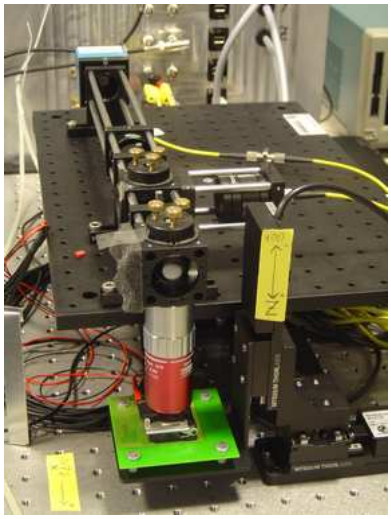

(a) Image of the setup for the crosstalk measurement: the mounting of the SiPM (green) as well as the objective lens (red) can be seen.

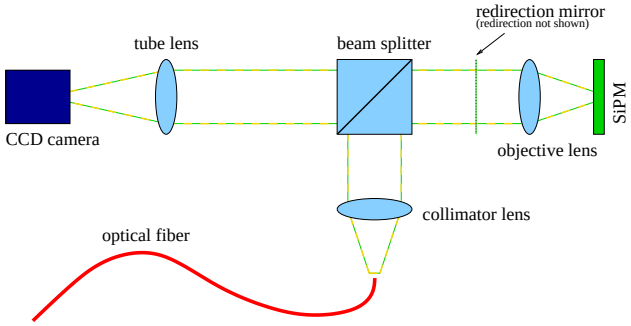

(b) Schematic optical path of the Laser spot, focused on the SiPM by means of a colimator lens, a beam splitter and an objective lens.

Fig. 4.2: Illustration of the crosstalk measurement setup[33]: With this setup a laser spot can be focused on one SiPM cell. So, the crosstalk of a single cell can be analyzed. First, one can focus on the SiPM by means of a microscope consisting of a CCD camera, a tube lens and an objective lens. Afterwards the laser spot, being focused on the SiPM can be coupled by using a beam splitter.

optics, see figure 4.2(b). The position of the laser spot on the cell can be checked by the back reflection from then SiPM surface. Moreover, the spot size can be verified by the CCD camera image, which shows also the dimensions of the SiPM structures. Such an image is shown in figure 4.3. The laser is a semiconductor laser that cam be either used in continuous wave mode (CW) or in pulsed mode, emitting light at 835 nm with a pulse duration of 50 ps. The laser is coupled to the microscope optics via a 50 μm optical fiber at the end of which a collimator lens parallelizes the light. This is necessary as the end of the fiber optics has a certain roughness. Hence the laser light is slightly scattered. Because of this effect the minimal achievable spot size is 2 μm. If the laser beam is not perpendicular with the SiPM surface, the positioning on the XY-plane can be faulty. Therefore, a redirection mirror is used for correcting this inaccuracy. Positioning has to be carried out manually. Afterwards, the coordinates of three point vertices of the

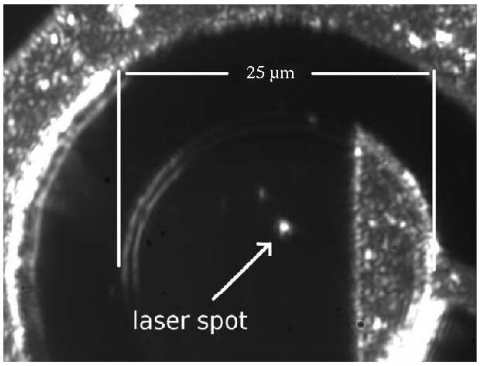

Fig. 4.3: Image of an illuminated HLL SiPM cell and the laser spot seen with the CCD camera[33]: The laser spot is much smaller than one cell. Its diameter equals ≈ 2 μm diameter.

SiPM, which define the surface plane of the SiPM, can be saved to a LabView program. This allows one to correct any further movements on the surface plane. For the simultaneous detection of the SiPM signal a 4 GHz Agilent oscilloscope, as well as a Lecroy oscilloscope are used. Both measurements show good agreement, which gives confidence in the correctness of the data acquisition. As the first analysis step the recorded raw data are saved by the LabView data acquisition system. In the second step the data are cleaned on a PC. For this, a Java script is used with which dark pulses and afterpulses[3] can be removed. The cleaned data are then analyzed in a further step by a root macro.

4.2.1 Crosstalk Measurement Procedure

Before the actual crosstalk measurement has been performed a reference measurement has to be done, assuring that the diameter of the laser spot is smaller than the diameter of one cell and that no other cell is illuminated. This check is carried out by measuring the change of the so-called dark rate. For this reference measurement the laser intensity is attenuated with optical attenuators, and the optical crosstalk is measured. The optical crosstalk, as a function of the laser intensity attenuation in dB, is shown in figure 4.4. As one can see, the crosstalk is independent of the laser intensity and confirms the operation principle that

[3]Afterpulses are generated by electrons of the created electron-hole pairs which got trapped in the lattice defects[29].

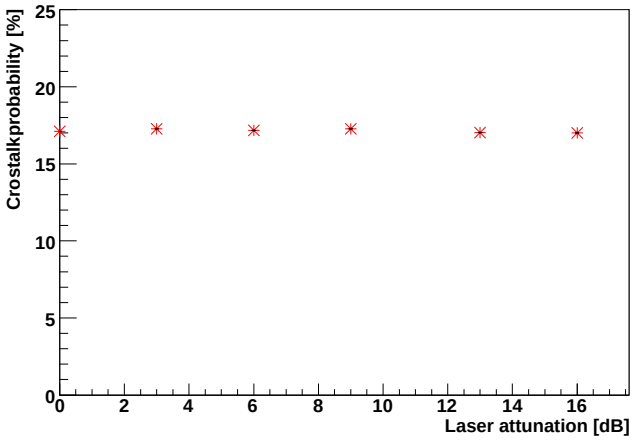

Fig. 4.4: Crosstalk rate versus laser intensity attenuation in dB: As expected, the crosstalk rate does not depend on the laser intensity.

the first converted photon triggers the cell and no change in amplitude of this cell occurs, independently of the number of further photons. The actual crosstalk measurement is performed as follows. The laser is focused on one SiPM cell of a Hamamatsu MPPC 100U, shown in figure 4.5. Here, the SiPM is illuminated with

Fig. 4.5: Image of the Hamamatsu MPPC 100U[30]

a cold light source such that one can be sure that the laser is both focused on the cell and positioned on its centre instead of hitting its border. Otherwise, potential beam diffraction could falsify the measured crosstalk. The laser is first operated in continuous wave mode for focusing and then switched to pulsed mode for measuring. Using the afore-mentioned measurement software, 20.000 waveforms, which assure sufficiently high statistics, are recorded for different bias voltages. The recorded waveforms are then conditioned by removing afterpulses and dark rate with another software tool. A peak amplitude spectrum is created for each bias

voltage, using a root macro. Figure 4.6 shows such a peak amplitude spectrum. Its single photoelectron (PE) peak is fitted with a Gaussian algorithm. Actually,

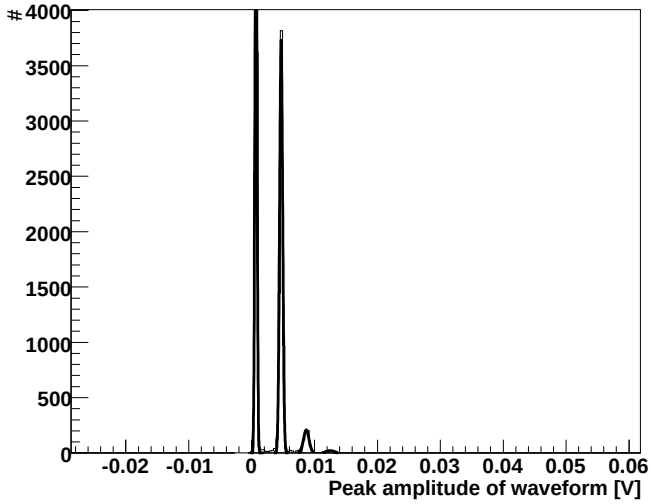

Fig. 4.6: Cleaned peak amplitude spectrum of the Hamamatsu MPPC 100U recorded for the crosstalk measurement: Normally, one would only see the pedestal peak and the 1Pe peak, since one cell is illuminated. But, due to crosstalk there are also peaks of higher PE events.

there should only be one peak besides the pedestal peak, because only the cell, onto which the laser is pulsing, should fire. But, due to optical crosstalk, other cells are firing as well. From the other peaks in the pulse spectrum one can now determine the crosstalk probability. By using the parameters of the single Gaussian fits of the peaks, the pulse integral of each peak is calculated. With these, the crosstalk rate $r_{\mathrm{Crosstalk}}$ can be computed with the ratio of the sum of the 2 and higher PE peaks and the 1PE events.

$$r_{Crosstalk} = \frac{\sum_{i=2}^{n} i\mathrm{PE}}{1\mathrm{PE}} \tag{4.3}$$

The error of the evaluated crosstalk rate is determined according to Gaussian error propagation. Since the detected PE events follow the Poisson distribution, the error of these events can be computed by the square root of the total number

of events.

$$\Delta i\mathrm{PE} = \sqrt{i\mathrm{PE}} \tag{4.4}$$

Since the gain G_{SiPM} of the SiPM depends on the overvoltage bias, this crosstalk number is computed for each bias voltage. This can be calculated by the ratio of the distance d between the pedestal and the 1PE peak in the peak amplitude spectrum and the gain of the amplifier G_{Amp} multiplied by the elementary charge q_{e}.

$$G_{\mathrm{SiPM}} = \frac{d}{G_{\mathrm{Amp}} \cdot q_{\mathrm{e}}} \tag{4.5}$$

The gain of the amplifier G_{Amp} is about 8.9. As figure 4.7 of the calculated gain versus bias voltage shows, it is in first order proportional to the bias overvoltage. Since the crosstalk predominantly depends on both the PDE, which is

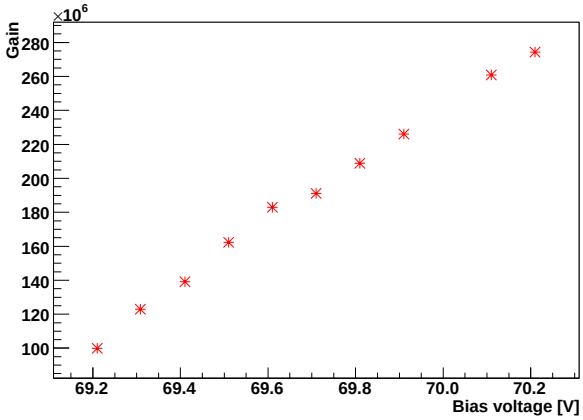

Fig. 4.7: Plot of the gain versus bias voltage of the Hamamatsu MPPC 100U: The gain seems to be proportional to the bias voltage.

proportional to the gain, as well as on the gain, it rises quadratically with the bias overvoltage, respectively with the gain. This can be seen in figure 4.8. This quadratic rise in crosstalk can easily be explained. Initially, photons in the first avalanche trigger some neighboring cells. In a second step these avalanches also emit light and trigger further cells. It is now obvious that operating a SiPM well over the breakdown voltage to achieve a high PDE can eventually set a chain reaction to trigger all cells by optical crosstalk. It is clear that if one wants a high

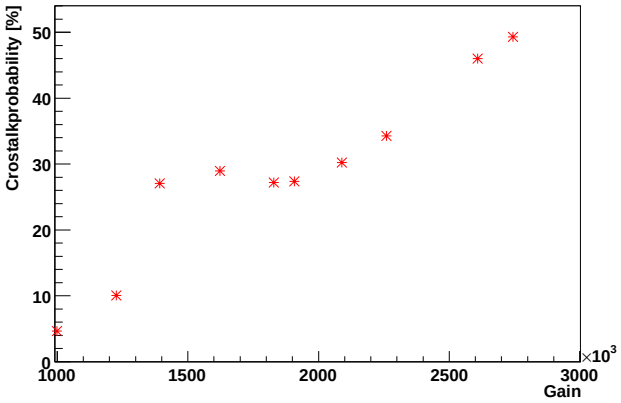

Fig. 4.8: Crosstalk in the SiPM MPPC 100U from Hamamatsu as a function of the gain when illuminating one cell with a laser pulse

PDE, one has to lower the intrinsic gain of cells by design consideration.

4.2.2 Comparison to conventional method

The conventional measurement of the crosstalk is to calculate the crosstalk rate $r_{crosstalk}$ by the ratio of the 1.5PE rate $r_{1.5PE}$ and the 0.5PE rate r_{05PE}[30].

$$r_{crosstalk} = \frac{r_{1.5\mathrm{PE}}}{r_{0.5\mathrm{PE}}} \tag{4.6}$$

These rates are measured with the SiPM in the 'dark mode' using a discriminator and a counter. The discriminator threshold is at first set to 0.5PE to measure the dark rate; afterwards it is set to 1.5PE. This measurement is done with a so-called threshold scan that automatically ramps the thresholds and measures the corresponding counter rates for dark rate, i.e., showing plateaus for the 1PE, 2PE and so on. As a result, one obtains almost a staircase function, as shown in figure 4.9. By fitting the first and second plateau the crosstalk can be evaluated with the above mentioned formula 4.6. Since the gain cannot be measured with this method as easily as in my method the crosstalk, measured for different bias voltages, is presented as a function of the bias voltage, as presented in figure 4.10. One can conclude, that the crosstalk, measured by the threshold scan, rises also in first order quadratically with the overvoltage. The comparison of the deter-

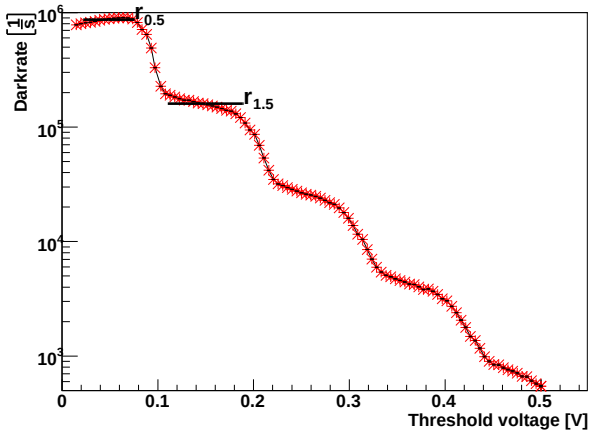

Fig. 4.9: Darkrate measured with counter threshold scan as a function of the threshold voltage of the Hamamatsu MPPC 100U: One sees that the plateaus are sufficiently distinctive.

mined crosstalk rate for different methods with that measured by Hamamatsu is presented in table 4.1. The differences between the measurement results can be

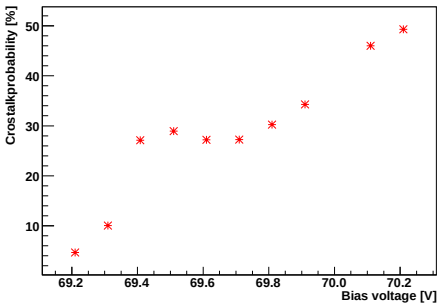

(a) crosstalk of a SiPM cell induced by a laser as a function of the bias voltage for the Hamamatsu MPPC 100U

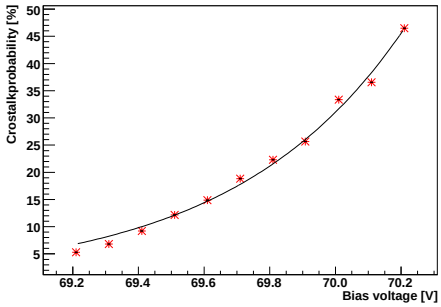

(b) Crosstalk evaluated with the counter threshold scan as a function of the bias voltage of the Hamamatsu MPPC 100U: The data are fitted with a with a polynomial function of second degree.

Fig. 4.10: Graphics of the evaluated crosstalk rate measured with the two used methods

traced back to temperature differences, since the breakdown voltage and hence the gain is temperature-dependent. Also, the width of the window used for pulse detection has an influence on the height of the peak amplitude spectrum. Hence this influences the crosstalk rate computation because one potentially cuts a part

of the pulses (It would in principle be better to use a pulse peak height analysis than a pulse charge analysis). Also it could be that the crosstalk rate depends on the cell position within the matrix. A cell located at or close to the outer rim of the SiPM should produce less crosstalk than a centered one because of the its number of neighboring cells. According to the data sheet, the Hamamatsu

Crosstalk rate [%]		
Laser induced crosstalk	Threshold scan	Threshold scan by Hamamatsu
≈ 26	≈ 19	22.6

Tab. 4.1: Presentation of the determined crosstalk rates for the Hamamatsu MPPC 100U at room temperature and 69.7 V bias voltage[4]

MPPC 100U has a gain of $2.4 \cdot 10^6$ already at a small overvoltage of 1.5 V. According to formula 4.2 the avalanche would generate around $75 - 100$ photons that can trigger by crosstalk many addition cells. This is quite critical because at such a low overvoltage the probability of triggering an avalanche is still well below 100 % and in turn the PDE will be quite low. In order to really reach a high PDE , which automatically requires a large cell size with a minimal dead area, one has to reduce the gain by reducing the cell capacitance. According to private communications (E. Lorenz) there are intense discussions ongoing with Hamamatsu to lower the capacitance of the 100 x 100 μm cells. This reduction in capacitance and hence the gain can only be achieved by increasing the depleted 'n' layer behind the high field zone and by accepting a small increase in dark rate due to the larger volume of temperature generated holes, which still have a much lower probability of starting an avalanche than electrons do.

[4]Note that the crosstalk rate, indicated by Hamamastu, has been emasured for 655 nm whereas the wavelengths of the used semiconductor laser is 835 nm. Since optical crosstalk is assumed to be wavelength-dependend this is one possible reason for the divergence of the different results.

5 Conclusion and Outlook

In this thesis the optical parameters of the aluminium mirror panels of the MAGIC II telescope were determined. Their verifyfication showed that they are of good quality. Therefore, a good optical performance of the reflector of the telescope can be expected. Moreover, the data can be used for the Monte Carlo simulation of the telescope. This simulation can be improved by using the newly introduced parameter, called focused reflectivity. Due to the verification of its repeatability and its measurement method this is a reliable parameter. In order to measure the spectral dependence of the focused reflectivity, future experiments should be carried out, for example, the emission characteristic of the xenon lamp, as well as the functioning of the blaze grid could be analyzed. By evaluating this spectrum the Monte Carlo simulation could be greatly improved. More important, the evaluation of the focused reflectivity shows that the total reflectivity is lower as specified within the declared wavelength range due to light scattering. This leads to the question whether the production method for the all-aluminium mirrors should be improved in order to further reduce the light scattering. Concerning the setup of the measurements of the optical parameters further improvements could meliorate the measurement accuracy. A major improvement would be to perform all the measurements in an empty and completely dark room in order to decrease light from the background. Additionally, it would be interesting to do simultaneous measurements with a second CCD camera in order to minimize measurement errors due to camera characteristics. Moreover, by using a cooling system for the semiconductor light source, light emission fluctuation could be further decreased. Alternatively, a feedback system based on a photodiode driving the current source, could be used. In order to comprehend why the focused reflectivity is lower for a shorter wavelengths than that for longer wavelengths (although it should be the other way around) further clarifying measurements should be made. In the other study, dealing with SiPMs for future light sensors

in IACTs, a new method of measuring optical crosstalk has been tested. The results of the measurements show good agreement with existing data acquired by conventional measurement methods. The measurement shows that the tested SiPM type has a too high gain, thus limiting the PDE well below the limit set by the device QE. There was no time to carry out a quantitative measurement. The determination of the optical crosstalk of the SiPM can nevertheless be used to choose the correct bias voltage for which the operating is optimized. Also, the acquired results give a better understanding of the detection performance of SiPM. Knowing this, the use of modified SiPM for future IACTs becomes quite possible. Also, the data can be used for appropriate future Monte Carlo simulations. A major improvement of the setup could be the implementation of temperature monitoring. In this way potential divergences of the acquired data due to temperature fluctuations can be reconstructed. By another analysis one should investigate the coherence between ambient temperature and bias voltage. Also, the dependency of optical crosstalk due to temperature changes should be evaluated. In summary, SiPMs for the detection of Cherenkov light should be 'blue sensitive', have a cell area similar to the studied SiPMs but a considerably lower cell capacitance in order to operate at higher overvoltages and higher PDEs. As in IACTs one is confronted with a large night sky background light a likely increase in dark count rate is tolerable.

Appendix

A Appendix

Description of the different classes of cosmic γ-ray sources

Active Galactic Nuclei (AGN)

Figure A.1 shows an active galactic nucleus (AGN). Basically, it consists of a super-massive black hole surrounded by an accretion disk. In addition, it has two jets which are perpendicular to the accretion disk's plane. The jets are composed of matter ejected from the accretion disk[34]. As briefly

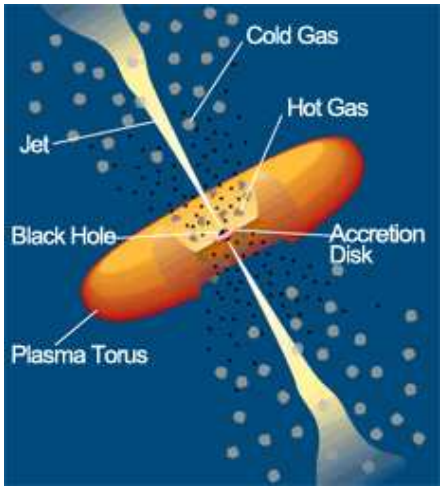

Fig. A.1: Sketch of an AGN [35]

described above, γ-radiation is produced via SSC scattering.

Microquasars

A microquasar[2] is a smaller AGN that has a strong and variable radio emission. These are so-called binary systems as they are composed of a

compact object such as a black hole or a neutron star. This object is accompanied by a large star, a red giant, for instance. Figure A.2 represents such a microquasar. Matter is accreted from this companion star and formed to an accretion disk that also has two jets perpendicular to its plane. Similar to that of the AGN the γ-production is assumed to be caused by SSC scattering.

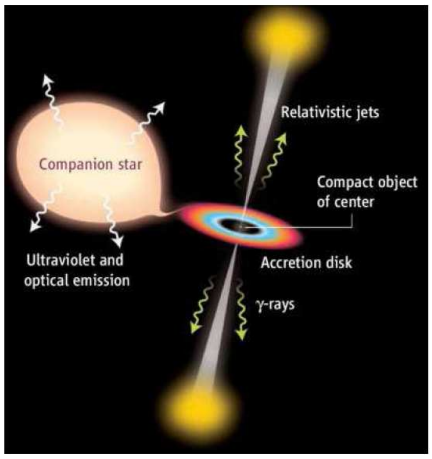

Fig. A.2: Sketch of a microquasar[2]

Supernova Remnants (SNR)

A SNR[4] is the resulting structure due to a stellar explosion. Following this explosion, named supernova, material is ejected. This material composes the SNR which is bound by an expanding shock wave. A supernova can come about either following a core collapse when a massive star ceases to generate fusion energy or when the accumulation of material from a companion star reaches a critical mass. This leads to a thermonuclear explosion. There are three possible mechanisms which can lead to γ-rays. The accelerated electrons inside the expanding shockwave can either interact with the cosmic microwave, or with the interstellar magnetic field. The respective mechanisms are IC and SSC scattering. Gamma-rays are also produced by Bremsstrahlung due to the electron's interaction with other particles.

Gamma Ray Bursts (GRB)

GRBs[2] are very short, high-energy explosions in the universe emitting gamma rays. Their duration normally varies from a few seconds up to several

minutes. Such a GRB is followed by a so-called afterglow which continues to fade for several weeks.

Pulsars and Pulsars Nebulae

A pulsar[36] is a rotating neutron star. Its magnetic field's axis of symmetry differs from the axis of rotation as shown in figure A.3. Therefore, a pulsar emits synchroton radiation along its resulting dipole axis. This radiation can be transformed into gamma rays by the above mentioned IC scattering.

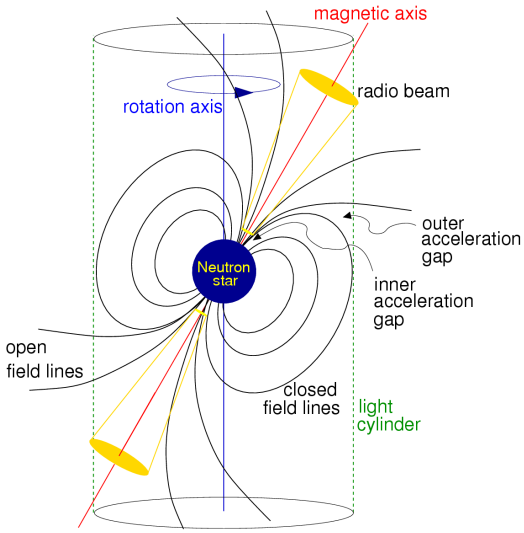

Fig. A.3: Schematic of a Pulsar [36]

B Appendix

Description of the active mirror control

The function and the components of the AMC are schematically shown in figure B.1. comprised the following elements:

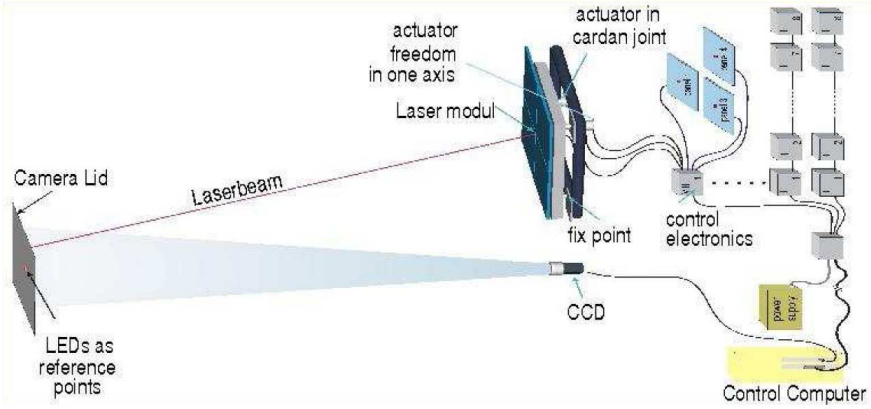

Fig. B.1: Functioning and components of the AMC[12]

- Two computer controlled actuators with a 20 micron positioning resolution
- A fixing element with a cardan joint
- A computer controlled laser pointer in the mirror element center that allows to check the mirror element deviation from its nominal position.
- A computer controlled laser pointer in the mirror element center that allows to check the mirror element deviation from its nominal position.
- A computer controlled laser pointer in the mirror element center that allows to check the mirror element deviation from its nominal position.

- A video camera that measures the actual laser spot of an element
- A video camera that measures the actual laser spot of an element
- A control computer that determines the deviation of a laser spot from its nominal position and corrects the mirror element orientation by sending the appropriate signals to the actuators.

Figure B.2 shows the telescope during repositioning.

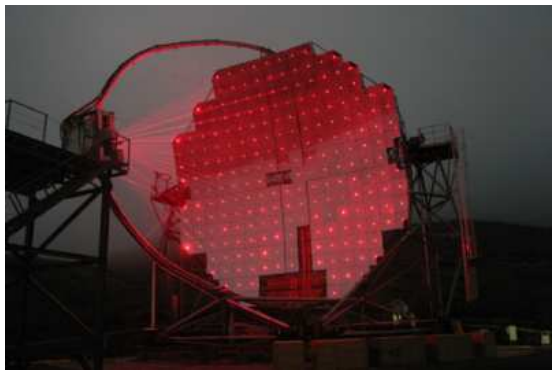

Fig. B.2: Laser calibration system for the repositioning of the mirror elements being switched on[12]

C Appendix

Calculation of the protective coating thickness

As shown in figure C.1, the influence of interference effects due to the protective coating can be evaluated as follows. The difference δ of the optical path of both

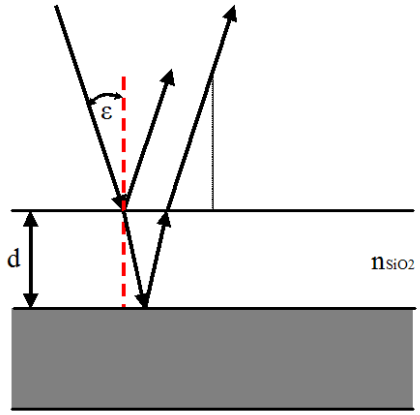

Fig. C.1: Interference effects at a coated surface. The light reflected by the coating interferes with the reflected light of the metallic surface

light beams can be computed by knowing the thickness d and the refractive index n_{SiO_2} of the coating, as well as the angle of incidence ϵ.

$$\delta = 2d\sqrt{{n_{SiO_2}}^2 - \sin^2(\epsilon)} \tag{C.1}$$

In the case of destructive interference the phase difference $\Delta\phi$ is maximal. It can be calculated by the addition of the phase jump π at the protective coating and the difference δ of the optical path.

$$\Delta\phi = \pi + \delta \tag{C.2}$$

If δ is 2π, the phase difference $\Delta\phi$ is maximal. This means that δ equals one entire wavelength λ. Therefore, the coating thickness d can be calculated as follows.

$$d = \frac{\lambda}{2\sqrt{{n_{SiO_2}}^2 - \sin^2(\epsilon)}} \tag{C.3}$$

The respective refractive index n of quartz is about 1.57. The angle of incidence ϵ is assumed to be 30°. Because of destructive interference the specular reflectivity has a minimum at 340 nm. Depending on the coating thickness this minimum of specular reflectivity is shifted to different wavelengths.
The above mentioned calculation can only be made for interference minima or maxima. The reason behind this is that one knows the exact phase of the light reflected from the coating and the light reflected from the $AlMgSi_1$ surface. In order to calculate the expected curve of the reflectivity of the coated mirrors a computation of the theoretical curve of the spectral reflectivity can be done with the following, see figure C.2. The light $I_{01}(\lambda)$, reflected at the air-quartz boundary

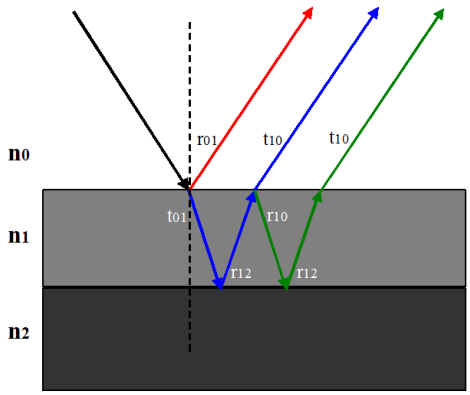

Fig. C.2: Layout of the reflectivity computation of a thin coated surface: The single multiple reflections on the quartz coating and on the $AlMgSi_1$ surface

and the light $I_{21}(\lambda)$ reflected at the aluminium surface crosses different optical distances. Therefore, they interfere with a phase difference $\Delta\phi$ which depends on the wavelength[1] The intensity $I_{01}(\lambda)$ results from the calculation of the reflectance

[1]Further multiple reflections are also taken into account for the reflectivity calculation. Their mathematical description will not be explained.

$r_{01}(\lambda)$ at the boundary layer between medium$_0$ and medium$_1$, which are air and quartz coatings. This is done by means of the respective refraction indices n_{air} and $n_{\text{SiO}_2}(\lambda)$[2].

$$I_{01}(\lambda) = (r_{01}(\lambda))$$

$$I_{01}(\lambda) = \left(\frac{n_{\text{air}} - n_{\text{SiO}_2}(\lambda)}{n_{\text{air}} + n_{\text{SiO}_2}(\lambda)}\right) \tag{C.4}$$

The intensity $I_{21}(\lambda)$ that is reflected from the AlMgSi_1 layer can be computed by the multiplication of the spectral reflectance factor $r_{21}(\lambda)$, the spectral transmittance factors $t_{01}(\lambda)$ and $t_{10}(\lambda)$

$$I_{12}(\lambda) = r_{21}(\lambda) \cdot t_{01}(\lambda) \cdot t_{10}(\lambda) \tag{C.5}$$

, with

$$\begin{aligned} r_{21}(\lambda) &= \left(\frac{n_{\text{SiO}_2}(\lambda) - n_{\text{AlMgSi}_1}(\lambda)}{n_{\text{SiO}_2}(\lambda) + n_{\text{AlMgSi}_1}(\lambda)}\right) \\ t_{01}(\lambda) &= \left(\frac{2n_{\text{air}}}{n_{\text{air}} + n_{\text{SiO}_2}(\lambda)}\right) \\ t_{10}(\lambda) &= \left(\frac{2n_{\text{SiO}_2}(\lambda)}{n_{\text{air}} + n_{\text{SiO}_2}(\lambda)}\right) \ . \end{aligned}$$

The addition of the intensities $I_{01}(\lambda)$ and $I_{12}(\lambda)$ considering the phase difference $\Delta\phi$ is approximately the spectral reflectivity $r(\lambda)$ of the mirror surface.

$$r(\lambda) = r_{01}(\lambda) + \left(t_{01}(\lambda) r_{21}(\lambda) t_{10}(\lambda) e^{-2j\delta}\right) \tag{C.6}$$

Considering further multiple reflections for the calculation of the reflectivity this computation is a geometric series with the following structure[24].

$$1 + q + q^2 + ... = \frac{1}{1-q} \tag{C.7}$$

, with

$$q = r_{01}(\lambda) r_{21}(\lambda) e^{-2j\delta} \ . \tag{C.8}$$

[2]The spectral refraction index $n_{\text{SiO}_2}(\lambda)$ of the SiO_2 coating is calculated by linear interpolation between existing data for the respective wavelengths.

Thus, $r(\lambda)$ can be computed as

$$r(\lambda) = r_{01}(\lambda) + t_{01}(\lambda)r_{21}(\lambda)t_{10}(\lambda)e^{-2j\delta} \cdot \frac{1}{1-q}$$

$$r(\lambda) = r_{01}(\lambda) + \frac{t_{01}(\lambda)r_{21}(\lambda)t_{10}(\lambda)e^{-2j\delta}}{1 + r_{01}(\lambda)r_{21}(\lambda)e^{-2j\delta}} \ . \tag{C.9}$$

The transmittance factor $t_{01}(\lambda)$ according to the energy conservation law is equal to

$$t_{01}(\lambda) = \sqrt{1 - r_{01}(\lambda)^2} \ . \tag{C.10}$$

Hence, the calculation can be simplified. Thus, the calculation can be made using the following formula:

$$r(\lambda) = \frac{r_{01}(\lambda) + r_{21}(\lambda)e^{-2j\delta}}{1 + r_{01}(\lambda)r_{21}(\lambda)e^{-2j\delta}} \ . \tag{C.11}$$

By the multiplication with its conjugate-complex term, one can obtain the spectral reflectivity.

$$R(\lambda) = r(\lambda) \cdot r(\lambda)^* \tag{C.12}$$

, where $\Delta\phi$ is the phase of the second light beam that crosses the additional optical path length d_{optical}. This equals to twice the coating thickness d_{SiO_2} divided by the wavelength λ and multiplied by the maximal possible phase of 2π.

$$\Delta\phi = \frac{4\pi \cdot d_{\text{SiO}_2}}{\lambda} \tag{C.13}$$

But, the correct computation can be made, only knowing the parameters n and k of the complex refraction indices $\tilde{\text{n}}_{\text{SiO}_2}$ and $\tilde{\text{n}}_{\text{AlMgSi}_1}$ of the quartz coating and the AlMgSi_1. These are not known.

D Appendix

Glass mirror production

The procedure used for the production of the glass mirrors, is called cold slumping technique[37]. Basically it is a replica technique of an exact machined negative of the mirror surface. The production company is Media Lario Technologies, which developed this technique in collaboration with the INAF-Brera Astronomical observatory. For this technique a glass sheet of 1.7 mm thickness is elastically deformed. This is done by placing it on a convex negative, called mould, with the appropriate radius of curvature, which the glass mirror is supposed to have. Figure D.1 shows this mould, which has to machined precisely as otherwise each defect of the mould would be reproduced on the glass sheet. The mould is made

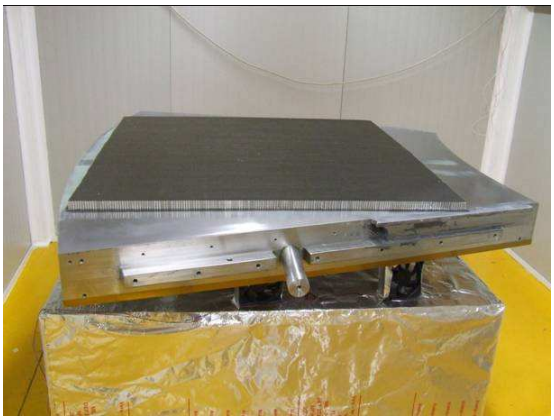

Fig. D.1: Mould of the cold slumping technique: A mirror is positioned on the mould.

of diamond milled aluminium. The mould has ventilation holes through which the air between the mould and the glass sheet is evacuated. The glass sheet is

therefore sucked into the mould reaching the required curvature. Then, a honeycomb structure with a 20 mm thickness is glued on top of the glass sheet. The honeycomb, which consists of Aluminium is used so that the glass sheet is maintains its curved shape. Afterwards, a second thin glass sheet is glued onto the honeycomb structure, again a sandwich structure of high stiffness and low weight is produced. The entire assembly is then placed inside a curing chamber. When the glue has dried the mirror assembly is released from the mould. Finally, the actual reflecting surface of Aluminium, as well as the quartz protection coating are vapor-deposited on the glass sheet with the concave shape. The schematic structure of the glass mirror is shown in figure D.2.The construction does not allow for a hole to house the laser in the centre that therefore can only be fixed to one edge. The total thickness of the glass mirror produced is about 24 mm and

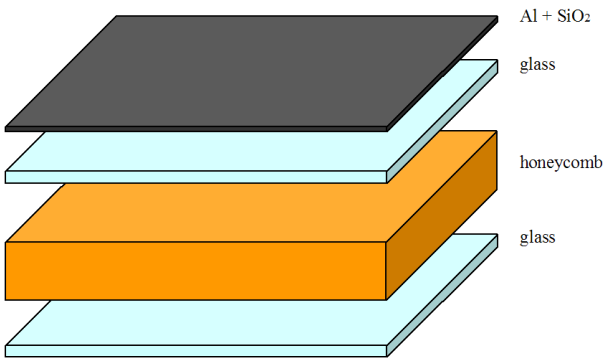

Fig. D.2: Schematic structure of the glass mirror produced

its weight is about 14 kg.

E Appendix

Spectrophotometer CM-2500d

With this device two measurements of the reflectivity can be performed simultaneously. One measurement includes the specular component, called SCI, which measures both components, the diffuse and the specular one. The other excludes this component and measures only the diffuse component. This is named SCE. For this type of measurement two light sources are used. The angle of illumination and the one for observation are inclined 8° towards each other. As one can see in figure E.1, two pulsed xenon lamps which emit a light spectrum from 360 nm to 740 nm are used for illumination. Via an internal optical path the detected light

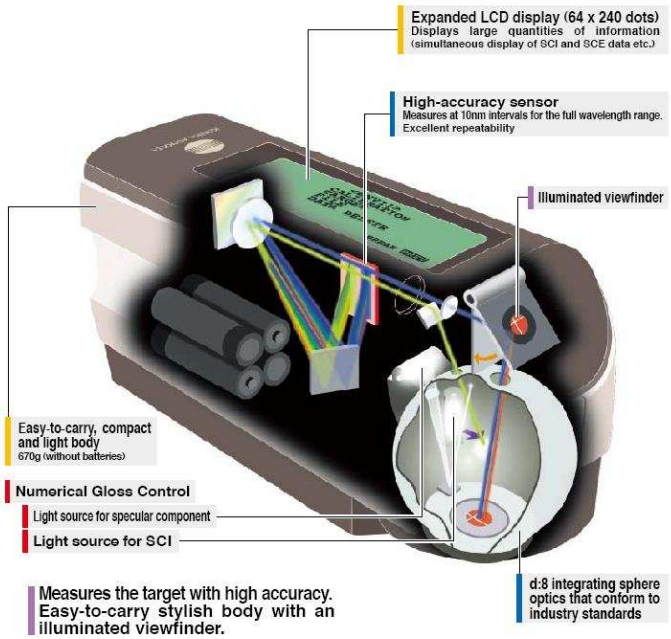

Fig. E.1: Schematic operation mode of CM-2500d[25]

is internally split up in its components via diffraction grating with a wavelength pitch of 10 nm. A silicon photodiode array detects the single spectral components. The disadvantage of this measurement device is the analysis wavelength range. This ends at 360 nm. It is, however, important to analyse the spectral reflectivity at a shorter wavelength where the Cherenkov radiation is still rather strong. More important, since the coating thickness is designed so that the spectral reflectivity is not falsified due to interference effects at 340 nm, this is not verifiable.

F Appendix

Comparison of the optical parameters of all-aluminium and glass mirrors

In this section, a brief comparison of the optical parameters of the different mirror types will be made. Since the quality check of the glass mirror elements has been carried out by Media Lario Technologies, only one of these mirrors has been analysed a second time in Munich at the MPI. As already mentioned, see section 2.4, the PSF of the glass mirrors is larger than that of the aluminium ones. It is 10 mm, whereas it is much smaller for the all-aluminium mirrors (less than 4 mm), see figure F.1. Nevertheless, the glass mirror PSF is still a lot smaller than the radius of a pixel of the MAGIC camera. Furthermore, there are differences

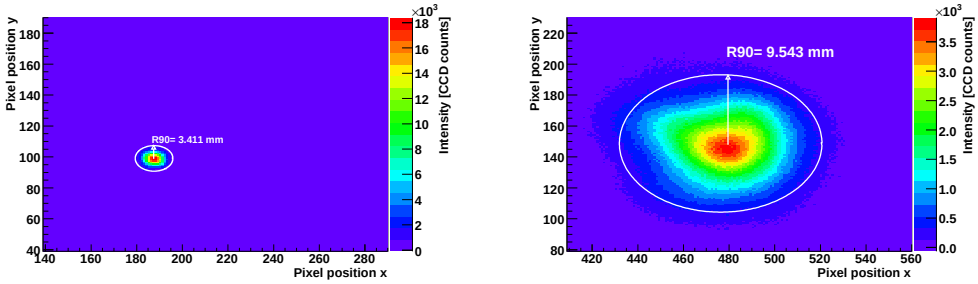

(a) PSF of an all-aluminium mirror

(b) PSF of a glass mirror

Fig. F.1: Comparison of the PSF of an all-aluminium and a glass mirror: The PSF of the all-aluminium mirror is only about a third og the glass mirror one's.

concerning the specular reflectivity spectrum. The glass mirror coating seems to be more homogeneous than that of the all-aluminium mirrors, as can bee seen in

figure F.2. Moreover, the average reflectivity seems to be slightly higher ($\approx$ 87 %) than that of the all-aluminium mirrors ($\approx$ 84 %). As far as the glass mirror's

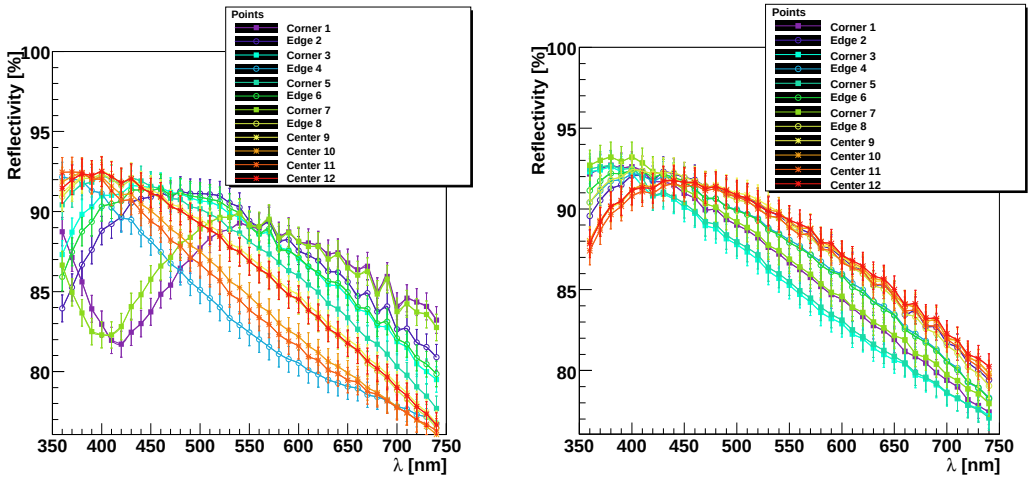

(a) Specular reflectivity spectrum of an all-aluminium mirror. On average it is about 84 %

(b) Specular reflectivity spectrum of a glass mirror. On average it is about 87 %

Fig. F.2: Comparison of the spectral specular reflectivity of an all-aluminium and a glass mirror: The coating of the glass mirror is much more homogeneous.

focused reflectivity is concerned, no measurements have been done yet. But, with regards to the other two important optical parameters of the glass mirrors it can be concluded that this second type of mirror panels fulfils the requirements for being used in the MAGIC telescope project.

List of Figures

List of Tables

List of Acronyms and Abbreviations

AGN	Active galactic nucleus
AMC	Active mirror control
CCD	Charged coupled device
CORSIKA	COsmic Ray SImulations for KAscade
CT	Cherenkov telescope
CV	Continuous Wave
EGRET	Energetic gamma-ray experiment telescope
FOV	Field of view
G-APD	Geiger avalanche photodiode
GRB	Gamma-ray burst
H.E.S.S.	High energy stereoscopic system
HEGRA	High energy gamma-ray astronomy
HLL	Halbleiter Labor [Max-Planck-Institut]
IACT	Imaging atmospheric Cherenkov telescope
IC	Inverse Compton
KASCADE	Karlsruhe shower core and array detector
LED	Light emitting diode
LONS	Light of the night sky
MAGIC	Major atmospheric gamma-ray imaging Cherenkov
MC	Monte Carlo [simulations]
MPP	Multi Pixel Photon Counter
PECVD	Plasma enhanced chemical vapour deposition

PIN	Positive intrinsic negative [diode]
PMT	Photomultiplier tube
PSF	Point spread function
QE	Quantum efficiency
RGB	Red Green Blue
RMS	Root mean square
ROOT	An object–oriented data analysis framework
QW	Quantum well
SCE	Specular component excluded
SCE	Specular component included
SiPM	Silicon Photomultiplyer
SNR	Supernova remnant
SSC	Synchrotron-self Compton
UHE	Ultra high energy
UV	Ultraviolet
VCSEL	Vertical cavity surface emitting laser
VHE	Very high energy

Bibliography

[1] M. Gaug. *Calibration of the MAGIC Telescope and Observation of Gama Ray Bursts*. PhD thesis, Universitat Autonòma de Barcelona, 2006.

[2] H. Bartko. *Observation of Galactic Sources of Very-High-Energy Gamma-rays with the MAGIC Telescope*. PhD thesis, Ludwig-Maximilians-Universität München, 2006.

[3] R. C. Hartman, D. L. Bertsch, S. D. Bloom, A. W. Chen, P. Deines-Jones, J. A. Esposito, C. E. Fichtel, D. P. Friedlander, S. D. Hunter, L. M. McDonald, P. Sreekumar, D. J. Thompson, B. B. Jones, Y. C. Lin, P. F. Michelson, P. L. Nolan, W. F. Tompkins, G. Kanbach, H. A. Mayer-Hasselwander, A. Mücke, M. Pohl, O. Reimer, D. A. Kniffen, E. J. Schneid, C. von Montigny, R. Mukherjee, and B. L. Dingus. The Third EGRET Catalog of High-Energy Gamma-Ray Sources. , 123:79–202, jul 1999.

[4] N. Tonello. *Observation of VHE γ-Rays from the Vincinity of magnetized Neutrin Stars and Development of new Photon-Detectors for Future Ground based γ-Ray Detectors*. PhD thesis, Technical University Munich, 2007.

[5] R. Wagner. *Measurements of VHE $\gamma - ray$ emission from four blazars using the MAGIC telescope and a comperative blazar study*. PhD thesis, Technical University Munich, 2006.

[6] D. Paneque. *The Magic Telescope: development of new technologies and first observations*. PhD thesis, Technical University Munich, 2004.

[7] F. Schmidt. Corsika shower images, 2005.

[8] C. Masterson. Observation of Galactic TeV Gamma Ray Sources with H.E.S.S. In *The 28th International Cosmic Ray Conference*. Universal Academy Press Inc., 2003.

[9] D. Britzger F. Goebel. The MAGIC Telescope Gamma Ray Detection with Cherenkov Telescopes, 2008.

[10] J. Knapp and D. Heck. Extensive air shower simulations with the CORSIKA code. *Nachr. Forschungszent. Karlsr., Vol. 30, No. 1, p. 27 - 37*, 30:27–37, 1998.

[11] J.A. Barrio et al. The MAGIC telescope design study. Technical report, Max Planck Institue for Physics, 1998.

[12] A. Biland, M. Garczarczyk, H. Anderhub, V. Danielyan, D. Hakobyan, E. Lorenz, R. Mirzoyan, and for the MAGIC Collaboration. The Active Mirror Control of the MAGIC Telescope. *ArXiv e-prints*, sep 2007.

[13] E. Carmona, P. Majumdar, A. Moralejo, V. Vitale, D. Sobczynska, M. Haffke, C. Bigongiari, N. Otte, G. Cabras, M. De Maria, F. De Sabata, and for the MAGIC Collaboration. Monte Carlo Simulation for the MAGIC-II System. *ArXiv e-prints*, sep 2007.

[14] M. Doro. The Reflective Surface of the MAGIC Telescope, 2007.

[15] J. A. Barrio et al. Development of all-aluminum mirrors for imaging Cherenkov telescopes. In *Towards a major atmospheric Cherenkov detector V*, page 374, 1997.

[16] M. Doro et al. The reflector of the Imaging Atmospheric Cherenkov Telescope MAGIC.

[17] D. Bastieri, J. Arnold, C. Baixeras, O. Citterio, F. Dazzi, B. De Lotto, M. Doro, M. Ghigo, E. Giro, F. Goebel, R. Kosyra, E. Lorenz, M. Mariotti, R. Mirzoyan, R. Paoletti, G. Pareschi, D. Pascoli, A. Pepato, L. Peruzzo, A. Saggion, P. Sartori, and A. Sillanpää. The reflecting surface of the MAGIC-II Telescope. *ArXiv e-prints*, sep 2007.

[18] R. Susa. *MMC900*. LT ULTRA Precision Technology GmbH.

[19] Klaus-D. Vissing. *Aufskalierung plasmapolymerer Beschichtungsverfahren*. Cuvillier Verlag, Göttingen, 2008.

[20] SBIG Astronomical Instruments. *Model ST-402ME ST-1603ME and ST-3200ME CCD Imaging Cameras* .

[21] B. J. Pichler, E. Lorenz, R. Mirzoyan, L. Weiss, and S. I. Ziegler. Production of a diffuse very high reflectivity material for light collection in nuclear detectors. *NIM*, 442:333–336, mar 2000.

[22] D. Kühlke. *Optik: Grundlagen und Anwendungen.* Harri Deutsch Verlag, 2 edition, 2004.

[23] J. W. Goodman. *Introduction to Fourier Optics.* Roberts & Co Publishers, 2004.

[24] L. Papula. *Mathematik für Ingenieure und Naturwissenschaftler. Ein Lehr- und Arbeitsbuch für das Grundstudium.* Vieweg, 4 edition, 2001.

[25] KONICA MINOLTA SENSING INC. *Spectrophotometer CM-2500d*, 2001.

[26] Lot-Oriel Group Europe. *50 - 150 W Bogen-Lichtlampe.*

[27] Andor Technology. *SR-303i*, 2008.

[28] D. Renker. Silicon Photomultipliers, 2005.

[29] N. Otte. *Study of the VHE gamma-ray emission from Active Galactiv Nucleus 1ES1959+650.* PhD thesis, Technical University Munich, 2006.

[30] Hamamatsu Photonics K. K. *MPPC Multi pixel photon counter*, January 2008.

[31] S. M. Sze. *Physics of semiconductor devices.* Physical Sciences Data, 1981.

[32] I. Rech, A. Ingargiola, R. Spinelli, I. Labanca, S. Marangoni, M. Ghioni, and S. Cova. Optical crosstalk in single photon avalanche diode arrays: a new complete model. *Optics Express*, 16:8381–+, may 2008.

[33] K. Prothmann. Comparative Measurements of Silicon Photomultipliers for the Readout of Highly Granular Hadronic Calorimeter. Master's thesis, Ludwig-Maximilian-University, 2008.

[34] C. Arbeiter. *Inverse Comptonstreuung und die Hochenergie-Emission relativistischer Stoßwellen.* PhD thesis, Ruhr-Universität Bochum, 2005.

[35] C. M. Urry and P. Padovani. Unified Schemes for Radio-Loud Active Galactic Nuclei. , 107:803–+, September 1995.

[36] T. Schweizer et al. Observation of Pulsed gamma-Rays Above 25 GeV From the Crab Pulsar with MAGIC . *Sciences Express*, oct 2008.

[37] G. Pareschie et al. Glass panels by cold slumping to cover 100 m^2 of the MAGIC II Cherenkov telescope reflecting surface. In *SPIE Astronomical Instrumentation*, 2008.

Acknowledgements

First of all, I would like to thank Dr. Florian Goebel for his support, scientific advice and encouragement during my entire thesis. I am very grateful for having made his acquaintance, as well as having had the opportunity to work with him both in Munich and in La Palma. I deeply mourne the tragic passing of Florian. During my thesis I very much appreciated the efforts of Prof. Dr. Sotier being my supervisor tutor on behalf of the university. I would like to express my special gratitude to Razmik Mirzoyan for having helped me a lot by revising my thesis and always giving me good advice, as well as to Prof. Dr. Masahiro Teshima who gave me the opportunity of working for MAGIC.

I am very much obliged to Hanna Kellermann for her continuous help and sympathy.

I also would like to thank the entire MAGIC group for the discussions concerning experimental work and their general contribution. Especially, I thank Ralf Kosyra, Jürgen Hose.

Many of my measurements wouldn't have been possible without the unhesitating provision of the many mechanics and electricans of the MPI. Finally, I would like to thank my parents and my boyfriend Michael Thomas for sharing life with me, for giving me invaluable support and beliving in me.